AC LOSS IN SUPERCONDUCTING COMPOSITES: CONTINUOUS AND DISCRETE MODELS FOR ROUND AND RECTANGULAR CROSS SECTIONS, AND COMPARISONS TO EXPERIMENTS

DISSERTATION

Presented in Partial Fulfillment of the Requirements for

the Degree Doctor of Philosophy in the Graduate

School of The Ohio State University

By

EUNGUK LEE, M.S

*****

The Ohio State University
2004

Dissertation Committee:

Professor S.A. Dregia, Advisor

Professor M.D. Sumption Co-advisor

Professor S.A. Akbar

Professor E.R. Kreidler

Approved by

Advisor

Co-advisor
Department of Materials Science & Eng.

ABSTRACT

In this work, AC loss in superconducting composites was described using both an anisotropic continuum model and a discrete model. The efforts were concentrated in three main areas. First, the eddy current coupling loss of composites with rectangular cross section was calculated using an anisotropic continuum description based on a block model with different effective resistivities in each block. In this case, a numerical approach was used. This treatment, like the more typical lumped component network model, was able to describe many factors influencing the eddy current loss in the rectangular composites, such as twist pitch, aspect ratio, and core resistivity. However, the influence of core thickness and the presence of an outer sheath were also described with this model. Certain simplifying assumptions were used here to minimize computation time, while allowing the essential information to be extracted.

In the second area, the eddy current loss of round composites were calculated from a discrete (network) point of view, and analytic expressions were developed which allow comparison to analytic expressions which were derived from effective medium theory. We need to measure only the contact resistance between the strands. The eddy current coupling loss of seven-strand MgB_2 cables were then calculated by this model. With this model, it was possible to use a measured contact resistance between the strands to both predict the loss and compare to effective medium based resistivities. The results from the block model and from the analytical model give results in reasonable agreement.

In the third part of the work, we attempt to compare the developed expressions to experiment. In some cases, data extant in the literature were used; in other cases, direct measurements were performed. For the rectangular geometry composites, existing data were sufficient. In the case of round composites, direct experiments were performed. The specific working medium chosen was round, seven-strand MgB_2 cables.

In comparing measurements to theory, it was necessary to add the hysteretic component of loss. In this case, it was also necessary to include the effect of magnetic shielding. It was shown that there are two kinds of hysteretic losses in these ferromagnetic/SC composites; the real loss and the apparent loss. Reduction of the real loss is always smaller than reduction of the apparent loss due to the shielding effect of sample signal with respect to the pick-up coil of VSM (Vibrating Sample Magnetometer).

In turn, the eddy current component for round composites was controlled by the contact resistance. The contact resistance was in some cases about two orders higher than the control samples when certain insulating surface treatments were performed on the surface of the individual strands of the cable. Loss predictions form contact resistant measurements were very low. However, actual loss measurements gave losses even lower, due to a low strand permeability.

DEDICATION

To my parents

ACKNOWLEDGMENTS

Five and half years is too long for this thesis, but it is too short for me to understand partly about the AC loss phenomena in superconducting composites. I always thank to my advisors, Dr. E.W. Collings and Dr. M.D. Sumption for teaching me patiently throughout my study in Ohio State University. Besides things directly related to my topic, I learned a lot from them about how to carry out a research.

I also thank to my colleagues, Dr. F. Buta, X. Peng and other members in LASM for their help to my study.

I want to share this joy with friends in my department especially ChongHoon and other Korean friends, who were together with me in Columbus where I spent my youth. Also, I want to thank to my wife Sunyoung, who came to this country leaving everything behind home.

VITA

June 26, 1968. . . . . Seoul, Korea

1991 . . . . B.S.
Yonsei University.

1995 . . . . M.S.
Yonsei University.

1998 – 2001. . . . . .M.S.
The Ohio State University.

1998 – 2004. . . . . .Research Asst.
The Ohio State University.

PUBLICATIONS

Research Publications

1. M. D. Sumption, E. Lee, and E. W. Collings, "Influence of Filamentary and Strand Aspect Ratios on AC loss in Short, Untwisted Samples of HTSC and LTSC Superconducting Multifilamentary Composites," *Physica C*, vol. 337, pp. 187-194, 2000.

2 M. D. Sumption, E. Lee, S. X. Dou, and E. W. Collings, "Extraction of Matrix Resistivity from Short Samples of Superconducting Multifilamentary Composite Tapes: Influence of Strand Twist and Internal Structure," *Physica C*, vol. 335, pp. 164-169, 2000.

3. M. D. Sumption, E. Lee, and E. W. Collings, "Analysis of Eddy Current AC loss for Untwisted, Multifilamentary Superconducting Composite with Various Aspect Ratios," *IEEE transactions on Applied Superconductivity*, vol. 11, pp. 2963-2966, 2001

4. M. D. Sumption, E. Lee, E. W. Collings, X. L. Wang, and S. X. Dou, "Suppression of AC(Hysteretic) Loss by Magnetic Shielding of MgB_2/Fe Superconductors: The Pseudo-Meissner Effect," *Advances in Cryogenic Engineering*, vol. 48, pp. 824, 2001.

5. E. W. Collings, E. Lee, and M. D. Sumption, "Transverse Resistivities in Untwisted HTSC Tapes at 4.2, 30, and 60K," *Physica C*, vol. 357-360, pp. 1153-1159, 2001.

6. M. D. Sumption, E. W. Collings, E. Lee, X. L. Wang, S. Soltanian, and S. X. Dou, "Reduction and Elimination of External-field AC loss in MgB_2/Fe Wire by in situ Magnetic Shielding," *Physica C*, vol. 378-381, pp. 894-898, 2002.

7. M. D. Sumption, E. W. Collings, E. Lee, X. L. Wang, S. Soltanian, S. X. Dou, and M. Tomsic, "Real and Apparent Loss Suppression in MgB_2 Superconducting Composites," *Physica C*, vol. 382, pp. 98-103, 2002.

8 E. Lee, M. D. Sumption, and E. W. Collings, "Temperature and Field Dependence of the Effective Matrix Resistivity of Bi:2223/Ag Composites," *IEEE Transactions on Applied Superconductivity*, vol. 13, pp. 3614, 2003.

9. E. Lee, M. D. Sumption, and E. W. Collings, "FEM Modeling of AC loss in Rutherford Cables with and without Resistive Cores," presented at CEC/ICMC, Anchorage, Alaska, 2003.

FIELDS OF STUDY

Major Field: Materials Science & Engineering

TABLE OF CONTENTS

Page

Abstract. ii

Dedication. iv

Acknowledgments v

Vita vi

List of Tables. xi

List of Figures xii

Chapters:

1. Introduction.. 1

1.1 Contents of this study. 1

1.2 AC loss of superconducting composites. 4

1.2.1 Hysteresis loss. 4

1.2.2 Eddy current coupling loss. 6

1.3 Factors affecting AC loss. 9

1.3.1 Magnetic field. 9

1.3.2 Frequency. 10

1.3.3 Temperature. 11

1.3.4 Filament diameter. 12

1.3.5 Twist pitch. 12

1.3.6 Matrix resistivity. 13

References for Chapter 1. 22

2. Numerical Methods. 26

2.1 Conductivity ratio limit. 26

2.2 Geometry and mesh size. 28

2.3 Boundary setup. 28

2.4 Solver type. 29

2.5 Loss calculation method. 29

References for Chapter 2 34

3. Experimental Methods. 35

3.1 Sample specification. 35

3.1.1 Hysteresis losses in samples with magnetic shielding effects 35

3.1.2 Samples for contact resistance measurements and AC loss measurement . . .36

3.2 VSM (Vibrating Sample Magnetometer). 37

3.2.1 1.7 T VSM. 37

3.2.2 9 T VSM. 38

3.2.3 Pick-up coil method. 40

References for Chapter 3. 54

4. Results and Discussion. 55

4.1 Numerical results. 55

4.1.1 Rectangular geometry conductor without core 56

4.1.2 Rectangular geometry conductor with core 57

4.1.3 Cylindrical geometry conductor. 60

4.1.4 Seven-strand model. 61

4.2 Experimental results. 62

4.2.1 Magnetic shielding in MgB_2 strand 62

4.2.2 AC loss measurement by pick-up coil method 65

4.2.3 AC loss from measuring contact resistance of MgB_2 seven strand cable. . . . 67

4.2.4 Microscopic analysis of contact region. 69

4.2.5 Comparison of AC loss calculation and AC loss measurement. 72

References for Chapter 4. 104

5. Conclusions 107

Appendix A Comparisons of discrete and continuous analytic models for rectangular geometry composites. 112

Appendix B. Eddy current coupling loss in seven- strand cables 115

Appendix C. Effective resistivity of a superconducting composite 118

Appendix D Contact resistance of a seven-strand cable. 121

Reference for Appendix 123

Bibliography. 124

LIST OF TABLES

Tables Page

2.1 Definitions of axes and the conductivity tensor for the four-block model 32

2.2 Number of tetrahedrons in each block region. 32

3.1 Sample specifications for the 9 T VSM 43

3.2 MgB_2 cable specifications for contact resistance measurements. 44

3.3 Specification of various coils in the pick-up coil system. 53

D.1 Possible current paths for R_1, R_2, R_3 and R_4. 122

LIST OF FIGURES

Figures Page

1.1 Schematic diagram of the mixed state of type II superconductors and a “fluxon” 16

1.2 Critical fields in superconductors. 16

1.3 *M-H* loops of irreversible and reversible type II superconductors 17

1.4 Current distribution in a cylindrical superconductor. 18

1.5 Current distribution in a cylindrical superconductor with a field dependent J_c. . .19

1.6 Filament coupling in superconducting composites 20

1.7 Critical temperature, field, and current density of superconductors 21

1.8 *E-J* characteristics in the presence of flux creep 21

2.1 The relationship between the base coordinate system and the sample geometry-based coordinate system 31

2.2 Example of sample geometry and mesh 33

3.1 Seven strand MgB_2 cables with a 6+1 geometry 44

3.2 Schematic of the 1.7 T VSM 45

3.3 1.7 T VSM 46

3.4 9 T VSM, head, mounting, and dewar. 46

3.5 Pick-up coil for the 9 T VSM. 47

3.6 Location of the maximum sensing point of the sample coil 48

3.7 Length dependence of the magnetic moment of the sample coil 48

3.8 Schematic of the sample coil 49

3.9 Impedance at different frequencies using several values of capacitance 49

3.10 Magnetic field distribution inside the external magnet. 50

3.11 Schematic for the pick-up coil method 51

3.12 Calibration of the pick-up coil method. 52

4.1 Twist pitch dependence of the eddy current coupling loss in the four-block model. 75

4.2 Four-block models with various aspect ratios. 76

4.3 Aspect ratio dependence of the eddy current coupling loss in the four-block model 77

4.4 Current distribution in the four-block model with a resistive core. 78

4.5 Geometry of the block model with different core thickness 79

4.6 Normalized loss vs. L_p. 80

4.7 Geometry of various core width-block models 81

4.8 Resistive core width dependence of Q_e 82

4.9 Effective resistivity derived using an analytic, anisotropic-continuum-based expression 82

4.10 Q_e vs t_c keeping $\rho_c t_c = 10^{-7}\ \Omega\text{m}^2$. 83

4.11 Q_e vs core conductivity for the four-block and core-models 83

4.12 Effect of an outer sheath on Q_e. 84

4.13 Conductivity tensor definition for a cylindrical four-block model. 85

4.14 Current distribution for the cylindrical four-block model 86

4.15 Q_e vs. L_p for the cylindrical four-block model. 87

4.16 Q_e vs. core radius and a comparison to the analytic model. 87

4.17 Schematic for a simple model of a seven-strand cable 88

4.18 Current distribution in a seven strand cable. 88

4.19 Current distribution for the seven strand cable model 89

4.20 Eddy current coupling loss of a seven-strand model with respect to twist pitch .90

4.21 *M-H* loops of an MgB_2 strand with an Fe matrix. 91

4.22 *M-H* loops of a bulk MgB_2 superconductor with no Fe matrix at various temperatures.. 92

4.23 Magnetic shielding effect at various temperatures. 92

4.24 *M-H* loop of an MgB_2/Fe wire measured at 4.2 K in a 9 T VSM 93

4.25 *M-H* loops generated by numerical calculation. 93

4.26 AC loss (Hysteresis loss) derived from *M-H* loops 94

4.27 *M-H* loops of SAE30 oil coated sample at 4.2 K by pick-up coil method 95

4.28. *M-H* loops of paint coated sample at 4.2 K by pick-up coil method. 95

4.29 *M-H* loops of an uncoated sample with no Fe layer at 4.2 K by the pick-up coil method. 96

4.30 Contact resistance in MgB_2 cables at 4.2 K with various insulating layers 97

4.31. Influence of twist pitch on the contact resistance of MgB_2 cables at 4.2 K 97

4.32 Optical microscopy on MgB_2 cables insulated using SAE30 oil 98

4.33 SEM images of the interface between stands of an MgB_2 cables 99

4.34 EDS analysis of oxygen in an MgB_2 cable. 100

4.35 BSE image and EDS analysis of sample without Fe layer. 101

4.36 EDS analysis of Fe in an MgB_2 cables. 102

4.37 Eddy current coupling loss of MOT01 at 4.2 K. 103

4.38 Eddy current coupling loss of PAT4 at 4.2 K. 103

A.1 Crossover area in a Rutherford cable 114

B.1 Eddy current path in a seven-strand MgB_2 cable 117

C.1 Unit cell of the filament with radius r_f, conductivity σ_f, and matrix with radius r_m, and conductivity σ_m. 118

D.1 Contacts between individual strands in an MgB_2 cable 121

CHAPTER 1

INTRODUCTION

1.1 Contents of this study

A number of applications have been or are being pursed for superconducting materials, such as power transfer lines, power transformers, superconducting magnets for MRI (Magnetic Resonance Imaging), and for particle accelerators. However, because the available temperature range limited by their critical temperatures, cooling is needed for the application of these materials. In addition, any AC loss coming from the superconductors represents additional heat loads to the system, and must be analyzed and minimized.

Superconducting materials are typically used in a form of composite, and a such are combined with low resistivity metals such as Cu and its alloys for LTSC (Low temperature superconducting composites) and Ag and its alloys for HTSC (High temperature superconducting composites). These metals employed both as matrix and sheath, surround the superconducting filaments, providing mechanical, electrical, and thermal protection of the composites. AC loss of these superconducting composites comes from both the superconducting filaments and the matrix materials.

AC losses of superconducting composites can be classified either by external source for the loss (magnetic field loss and transfer current loss) or by nature of the loss (hysteretic loss and eddy current coupling loss). This work focuses on the magnetic field loss which occurs when time-varying magnetic field applies to superconducting composites. Transfer current loss, also called self-field loss, occurs when AC current flows through superconducting composites. In practical application, the AC loss is summation of these losses.

When time-varying magnetic field applies to a superconductor, hyeteresis loss occurs. To reduce this loss the superconductor is divided to many fine filaments. Then, the matrix of normal metal is used to protect these fine filaments. And, eddy current coupling loss occurs within these superconduting filaments and normal matrix composites. Since there are so many filaments (or strands in case of cables), it was impossible to apply Maxwell equations to each individual component with proper boundary conditions. To solve this problem and obtain the eddy current coupling loss of superconducting composites, there were two basic models. One of them is a discrete model which describe the loss by lumped components, i.e. interstrand contact resistance[1], the other is a continuum model which describe the loss by effective conductivity of the composite and consider the composite as a homogeneous material[2].

Analytic expressions can be obtained from these two models and well apply to strands in case of the continuum model and to cables in case of the discrete model. However, when the geometry of the composites becomes complicate and important to reduce the eddy current loss, a numerical method is needed[3, 4]. For example, the effects of filaments array structure have been studied using FEM. In this work, the effects of core and outer sheath geometry will be described by block model based on continuum approach. This block model also can be applied to the loss of Rutherford cable which has been described by discrete model. Since the continuum approach was well applied to the case of cables, it is possible to compare the contact resistance from the discrete model and the effective resistivity from the continuum model. By doing this, it is possible to compare directly the eddy current loss of various composites (strands and cables) in terms of one parameter.

In Chapter 1, the basic features of superconducting composites relevant to their AC loss are described. Two models for eddy current coupling loss of superconducting composites, the anisotropic continuum model and the discrete model (lumped model, or network model), are introduced and compared to each other. In Chapter 2, the numerical methods used in these calculations will be described. In Chapter 3, the experimental methods for direct measurement of the AC loss will be described in detail. Chapter 4 has two sections, the first part is the results from the anisotropic continuum description, in terms of a numerical model. It is shown that such a numerical anisotropic continuum model is particularly useful in explaining certain aspect of the eddy current coupling loss in rectangular composites. The second part of Chapter 4 details the results from direct experiments. Both eddy currents and hysteretic losses are measured for MgB_2 composites. For completeness, the magnetic shielding effects reducing the hysteresis loss of individual MgB_2 strand are described. Next, contact resistance measurements and the microscopic analysis of superconducting samples are presented. Finally, the eddy current coupling loss values derived from numerical calculations, are compared to those from an analytical model. Chapter 5 summarizes the results of this study, and points to areas of needed future work.

1.2 AC loss of superconducting composites

Superconductors have *zero DC resistance*, but *do not* have *zero "AC resistance"*. When AC current is induced by time varying magnetic fields or applied by a direct AC current source, there is always AC loss in the superconductor. Even in a type I superconductor there is AC loss at high frequency (10 GHz)[2, 5]. There are three types of AC loss; hysteresis loss, eddy current coupling loss, and normal eddy current loss.

1.2.1 Hysteresis loss

When a magnetic field larger than H_{c1} is applied to a type II superconductor, some magnetic flux can penetrate inside, as shown in Fig. 1.1 and Fig. 1.2. Within the penetrated regions the field is present in the form of fluxons. The regions within the fluxons have normal resistivity. These fluxons may either be "free" in a perfectly homogenous sample or "pinned" by their interactions with defects. Flux motion is induced by the Lorentz force, $F = J \times B$. In the former case, there is a viscous nature to flux motion under AC fields. In latter case, the Lorentz force works against the pinning force, leading again to loss, related to the flux motion. Such flux motion always occurs in pinned Type II superconductors, because locally the Lorentz force overwhelms the pinning force (specific pinning force × density of pins), and this leads to irreversible behavior, i.e, loss. *M-H* loops of reversible and irreversible type II superconductor are shown in Fig. 1.3. After the applied magnetic field is cycled and goes to zero, there is a remaining magnetic flux, (i.e., fluxons) in case of an irreversible type II superconductor. The area of the *M-H* loop is the dissipated energy per one cycle, the hysteresis loss.

We can calculate the hysteresis of a superconductor by a basic power relation even if we do not know the exact mechanism.

$$P = \int_{Vs} J \cdot E \ dV \qquad (1\text{-}1)$$

where J is the current density, E is the electric field, V_s is the sample volume, and P is the loss per second. In (1-1), we note that the integrated volume is the filamentary volume of the superconducting composite. When we calculate the eddy current coupling loss, the integrated volume will be the filamentary region volume, which is defined as the superconducting filaments as well as the matrix between them.

To calculate this hysteresis loss analytically, we must know the current distribution inside the superconductor, J. We need a constitutive law (e.g., ohm's law). Such a constitutive model for superconductors is available; it is Bean's critical state model. In this model, we do not need to know "the resistivity" of superconductor, since it assumes a constant critical J (J_c) of superconductor. In this model, there are only two cases; J is zero or the critical current of superconductor, J_c.

$$J = J_C \frac{E}{|E|} = \frac{\partial B_Z}{\partial x} = \text{ constant , if } E \text{ is non zero.} \quad \text{or} \quad J = 0 \text{ , if } E = 0 \qquad (1\text{-}2)$$

The magnetic field and current distribution dictated by (1-2) are shown in Fig.1.4. and Fig.1.5. for a cylindrical sample[6]. The term $E/|E|$ determines the direction of current. The critical current density, J_c, and the associated flux gradients, are due to (and proportional to) flux "pinning" on defects. These may take various forms, including grain boundaries, point defects, dislocations, and twin boundaries. Increased flux pinning leads to a higher J_c and thus a larger area for the M-H loops. (1-1) has been calculated for a number of simple sample shapes and in case of cylindrical geometry, when field is applied to perpendicular to axis (e.g., wire), the hysteresis loss per cycle per unit volume is[2]

$$\oint \frac{P_h}{V_s} dt = \frac{128\mu_0 H_0^3}{9\pi J_c r_0} \quad (\mathrm{J/m^3}) \quad \text{if} \quad H_0 << H_p \qquad (1\text{-}1\text{-a})$$

$$= \frac{16}{3\pi} \mu_0 J_c r_0 H_0 \quad (\mathrm{J/m^3}) \quad \text{if} \quad H_0 >> H_p \qquad (1\text{-}1\text{-b})$$

Here, H_p is the penetration field, $H_p = (2/\pi)\, r_0\, J_c$, and r_0 is radius of superconducting wire, H_0 is the applied magnetic field. If r_0 is the radius of superconducting filament in a composite, the superconducting volume fraction, λ, should be included in (1-1-a) and (1-1-b).

1.2.2 Eddy current coupling loss

If an electromagnetic field changes with respect to time, eddy currents are induced within materials which are normal conductors. This leads to energy loss. However, in the case of superconducting composites, there are superconducting filaments embedded within the normal metal matrix. This filamentarization is needed to reduce hysteresis loss which is proportional to diameter of a superconducting filament. At quasi-static frequencies, the loss is hysteretic only in nature. When the frequency of the applied field increases, the filaments of superconducting composite begin to “couple”. Here, the term “couple” is used to describe currents which have paths which are partially within the superconducting filaments and partially in the matrix as shown in Fig. 1.6. When filaments are completely coupled, they behave as if the composite was a monofilament with a diameter equal to that of the filamentary region. These currents, which are essentially-normal metal, shielding-eddy currents, exacerbated by the presence of high conductivity paths, have losses associated with them. In fact, even though the losses originate exclusively with the normal conducting regions of the path, the losses from the "coupling currents" are far greater than normal eddy currents. If there are no superconducting filaments and only a normal conducting matrix exists, then only *normal* eddy current loss exists. However, if there are superconducting filaments in the current path of the eddy current, the resistance of current path is greatly reduced, therefore the circulating eddy currents increase and AC loss also increases. This enhanced eddy current loss, as noted above, is called coupling current loss. It must be noted that coupling current loss is also sometimes called simply "eddy current loss", when the *normal* eddy current loss inside the metal matrix can be ignored.

There are two basic models used to describe eddy current coupling loss in superconducting composites. One is the anisotropic continuum model (effective medium theory) from Carr[2] and another is the discrete model (network model, lumped model) from Morgan[1]. In the anisotropic continuum model, the superconducting composite is treated as a homogeneous material which is anisotropic. It can be treated as "homogeneous continuum" because the number of filaments is very large, and therefore, the filaments and the matrix can be treated as an "effectively averaged" material. The same power loss equation as (1-1) can be used, but the integrated volume is the filamentary region volume[7]. Based on (1-1), the coupling loss of round twisted composite in the low frequency range is[2]

$$\frac{P_e}{V_s} = (\mu_0 \dot{H}_0)^2 \sigma_\perp \left(\frac{L_p}{2\pi}\right)^2 = (2\pi f)^2 \frac{(\mu_0 H_0)^2}{2} \sigma_\perp \left(\frac{L_p}{2\pi}\right)^2 \qquad \text{(Watts/m}^3\text{).} \qquad (1\text{-}3)$$

Here, P_e is the eddy current coupling loss, V_s is the volume, L_p is the twist pitch, f is the frequency, μ_0 is the permeability of vacuum, H_0 is the applied magnetic field, and $\sigma_\perp$ is the effective transverse conductivity. For the eddy current coupling loss calculation, we use an "effective" transverse conductivity, $\sigma_\perp$. This represents a constitutive law for superconducting composites. For various sample shapes, Campbell calculated the coupling loss including a shape factor due to demagnetizing fields[8].

The eddy current coupling loss in Rutherford cables (a kind of rectangular superconducting composite) is explained within the network model of Morgan[1]. It has been much further developed by Sytnikov[9, 10] and Verweij[11]. Some comparison of the anisotropic continuum model and the network model has been made by both Carr[12] and Akhmetov[13]. An important distinction is that the network model uses interstrand contact resistance to describe eddy current coupling loss instead of an effective resistivity averaged over the whole cable. In particular, the network model is a lumped component model, where the projection of upper strands and lower strands produce the shape of network and the resistances between these strands are the determiner of the coupling current loss. In the expression by Morgan,

$$\frac{P_e}{V_s} = \frac{w}{t}\frac{{N_s}^2 L_p \dot{B}^2}{120 R_c} \qquad \text{(Watts/m}^3\text{)} \qquad (1\text{-}4)$$

or

$$\frac{Q_e}{V_s} = \frac{2}{3}\left(\frac{w}{t}\right)\left(\frac{{N_s}^2}{20 R_c}\right) L_p B_m \left(\frac{dB}{dt}\right) \qquad \text{(J/m}^3\text{)}$$

where N_s is the number of strands in the cable, w is the width of cable, t is the thickness of cable, L_p is twist pitch, $\dot{B}(=\mu_0 \dot{H})$ is the magnetic field rate of change, B_m is the magnetic field amplitude, and R_c is the interstrand contact resistance between the upper layer and bottom layer, per unit cell (in an area roughly the strand diameter squared). A comparison of expressions from the annisotropic continuum model and those from the network model is presented in Appendix A, where a relationship between the R_c parameter of the network model and the σ parameter of the anisotropic continuum model is derived.

1.3 Factors affecting AC loss

1.3.1 Magnetic field

In (1-2), we described a “single-valued” J_c (Bean’s critical state model). However, we can let J_c depend on applied field. According to Kim’s formulation of the critical state model this is expressed as (1-5) [6]

$$J_c = \frac{\alpha(T)}{c + H_0} \qquad (1\text{-}5)$$

Here, α is a constant when temperature is fixed and c is also a constant. H_0 is the applied magnetic field. (1-5) is the new constitutive law when J_c is dependent on magnetic field.

Qualitatively, we can expect from (1-1-a), a forth power dependence of hysteretic AC loss on applied field H_0 below the penetration field H_p. We must pay attention to the intensity of applied field when we analyze data with (1-1-a, b). If $H_0 < H_p$, hysteresis loss decreases with increasing critical current, J_c. If $H_0 > H_p$, hysteresis loss increases with increasing J_c.

The effect of magnetic field on the coupling current loss is more direct according to (1-3). The dependence on the square of the magnetic field originates from fact that the electric field within the superconducting composites depends on the magnetic field change via Maxwell's equation and the loss is the product of $J_{\perp}$ and $E = J_{\perp}/\sigma_{\perp}$. Here $\perp$ means "effective transverse" for any quantity, i.e., $J_{\perp}$ is the effective transverse current density.

1.3.2 Frequency

The hysteresis loss per cycle is typically considered to be independent of the frequency. However, the eddy current coupling loss per cycle is linearly dependent on the frequency in the low frequency range before all the filaments couple and "saturation" occurs.

In the low frequency range, the total AC loss *per cycle* is the sum of the hysteresis loss (1-1) and the eddy current coupling loss (1-3).

$$Q = Q_h + Q_e \cdot f \qquad (\mathrm{J/m^3}) \tag{1-6}$$

If we draw a line describing the measured AC loss with respect to frequency, the intercept is the hysteresis loss, and if we deduct this hysteresis loss from the total loss, we can obtain the eddy current coupling loss per cycle. Thus, from the frequency dependence of AC loss we can differentiate the hysteretic loss from the eddy current coupling loss[14, 15]. Except in the very low frequency range in which flux creep occurs, the independence of loss per cycle on frequency is used for verifying hysteresis loss in AC loss measurements even in HTSC[15-19]. But it is reported that in HTSC hysteresis loss can also depend on frequency to some extent [20-24]. Dependence of such creep related effects on frequency are affected by many factors such as magnetic field, temperature, and so on.

1.3.3. Temperature

When temperature rises, J_c decreases as shown in Fig. 1.7. From (1-1) it is expected that the hysteresis loss will be reduced when $H_0 > H_p$. When temperature rises, the magnetization of the superconducting composite decreases, therefore, the area of the associated *M-H* loops decrease and the AC loss per cycle also decreases.

However, when the temperature is high enough and the frequency is low enough, we can see that **flux creep** occurs. Flux creep is a phenomenon where the pinned fluxon inside superconductor becomes thermally activated at elevated temperatures. The hopping rate of a pinned fluxon from site-to-site follows an Arrhenius type equation (1-7)

$$\vec{r} = \vec{r}_0 \exp(-(U_0 - U_T)/k_B T) \qquad (1\text{-}7)$$

U_0 is activation energy for hopping, U_T is the amount of the reduction of activation energy by thermal agitation. A characteristic ***E-J*** curve is shown in Fig. 1.8. If there is flux creep, the ***E-J*** curve of the superconductor becomes nonlinear, and J_c is no longer a step function. There is always an additional energy dissipation due to the finite resistivity stemming from flux creep, even at a current smaller than J_c[25].

The effect of flux creep on the coupling current loss appears as an increased effective resistivity. When flux creep occurs, there are additional resistive current paths along the filaments[26].

1.3.4 Filament diameter

From (1-1-a, b), the hysteresis loss per unit volume is proportional to the filament diameter when the applied field is greater than the penetration field of the superconducting composite. Usually, superconducting composites are used above the penetration field (e.g., magnet applications). Therefore, it is desirable to make the filaments as fine as possible, but this is difficult in case of HTSC. Since a matrix is needed to support the filaments, coupling current loss occurs within each strand.

On the other hand, a thick monofilament can be favorable to reduce AC loss when DC transport current flows in the superconducting composite under a transversely applied AC magnetic applied field [27-31]. Under a transverse AC applied magnetic field, DC transport current causes additional AC loss due to “dynamic resistance”. If the applied field is kept below the penetration field (by increasing the filament diameter, e.g.), there is fluxon-free region in the center of superconductor and the DC transport current flows through this region without interacting with the flux.

1.3.5 Twist pitch

From (1-3), we know that eddy current coupling loss is proportional to the square of twist pitch L_p. L_p is similar to the sample length, L_s in case of an untwisted sample ($L_p \approx 2L_s$). To reduce eddy current coupling loss, it is necessary to reduce the sample length, or reduce the twist pitch of sample. According to Wilson [32], there is a critical sample length below which filament coupling does not occur. For the model system of a normal metal sandwiched within two superconducting slabs,

$$L_c = 4\left(\frac{\rho_m J_c d_s}{\partial B / \partial t}\right)^{\frac{1}{2}} \tag{1-8}$$

In (1-8), d_s is the thickness of superconducting slab, and ρ_m is resistivity of normal metal. This is too simple model to be quantitative for real strand, but such a ‘decoupling twist pitch’ does exist in twisted multifilamentary superconducting composites[33-37]. From (1-8), we know that twist pitch should be less than L_c for reducing eddy current coupling loss. However, the minimum twist pitch is often restricted by fabrication process limits (e.g., filament breakage and bridging, especially in HTSC).

The twist pitch of a superconducting composite should be as short as possible to reduce eddy current coupling loss in transverse fields. However in the presence of longitudinal field there is optimum twist pitch for minimum coupling loss[38, 39].

1.3.6 Matrix resistivity

Since there is a limit to reducing the twist pitch of a superconducting composite, we must increase the effective transverse resistivity if we wish to further reduce the eddy current coupling loss. Matrix resistivity does not affect the hysteresis loss of superconductor composite. If we increase the effective transverse resistivity, $\rho_\perp$, we know from (1-8) we can also increase the critical twist pitch (in superconducting composites, $\rho_\perp$ is equivalent to ρ_m).

There are two methods to increase $\rho_\perp$. One is alloying the matrix, the other is inserting a resistive barrier inside the matrix. In LTSC, Ni or Mn is added as an alloying element. Mn is an effective element for Cu matrix [40, 41]. It increases electrical resistivity but does not reduce thermal conductivity significantly, which is important to cryostability. In HTSC, the matrix is Ag, which has a high conductivity. Adding Au to the Ag matrix is an effective, but expensive, method for loss reduction.

Another way to increase the effective resistivity is by inserting a resistive barrier. The barrier material should not react with the ceramic superconducting filaments in HTSC and should be easily co-deformable with Ag in a rolling process. In some studies, $BaZrO_3$ or $SrZrO_3$ has been used as a resistive barrier material[42-47]. Using the barrier material to increase the effective resistivity is in theory better than an matrix alloying method, since the longitudinal resistivity along the composite axis which is important for the cryostability of system remains low, while only the transverse effective resistivity is increased.

We note that $\sigma_\perp$ is not the matrix conductivity itself. It is the "effective" transverse conductivity of the whole composite and is given as[2]

$$\sigma_\perp = \sigma_m \frac{(1+\lambda)}{(1-\lambda)} \qquad \text{if the interface resistivity is low} \qquad (1\text{-}9\text{-}a)$$

and

$$\sigma_\perp = \sigma_m \frac{(1-\lambda)}{(1+\lambda)} \qquad \text{if the interface resistivity is high} \qquad (1\text{-}9\text{-}b)$$

Here σ_m is the matrix conductivity and λ is the volume ratio of the superconducting filaments to the whole composite volume. The derivation of (1-9) is given in Appendix C (see also [48]). If there is a resistive barrier (1-9) has different form, namely[49]

$$\sigma_{\perp} = \sigma_{m} \frac{(1+\lambda) + X(1-\lambda)}{(1-\lambda) + X(1+\lambda)} \tag{1-10}$$

where $X = \sigma_m r_f / \sigma_b d_b$, r_f is the radius of the filament, σ_b is the conductivity of barrier, and d_b is the thickness of the barrier. From (1-10) we can recover (1-9). If there is no barrier, $X \to 0$ and (1-10) becomes (1-9-a). If there is perfect barrier, $X \to \infty$ and (1-10) becomes (1-9-b).

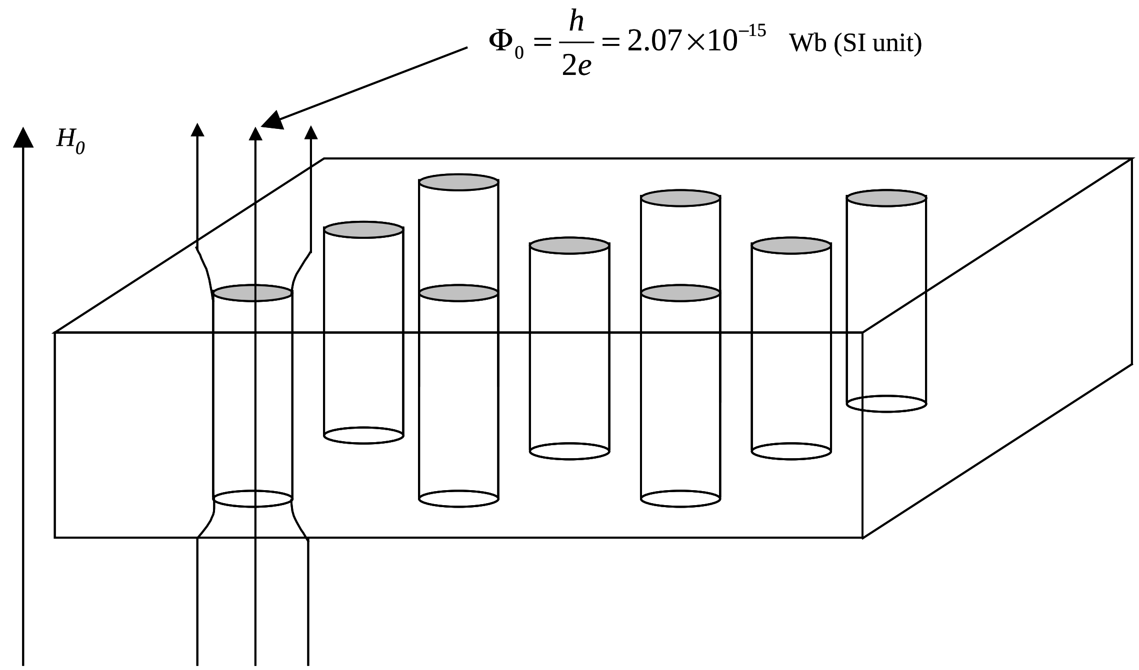

Fig. 1.1. Schematic diagram of the mixed state of type II superconductors and a “fluxon”.

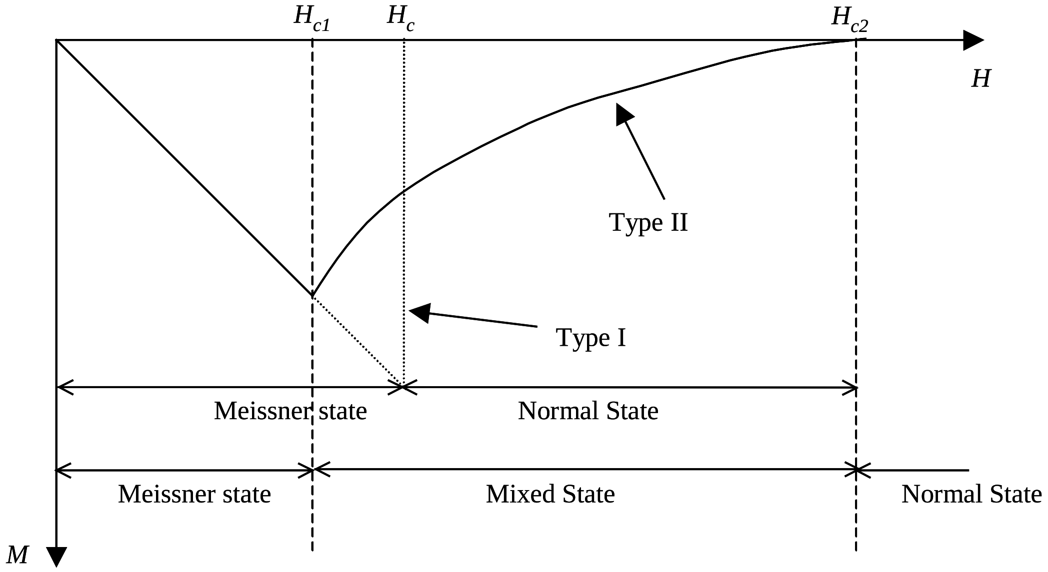

Fig. 1.2. Critical fields in superconductors. Below H_{c1} a type II superconductor is in the Meissner state. At H_{c1} Flux begins to penetrate until H_{c2} is reached. Above H_{c2} it becomes a normal conductor. A type I superconductor is in itsMeissner state below H_c

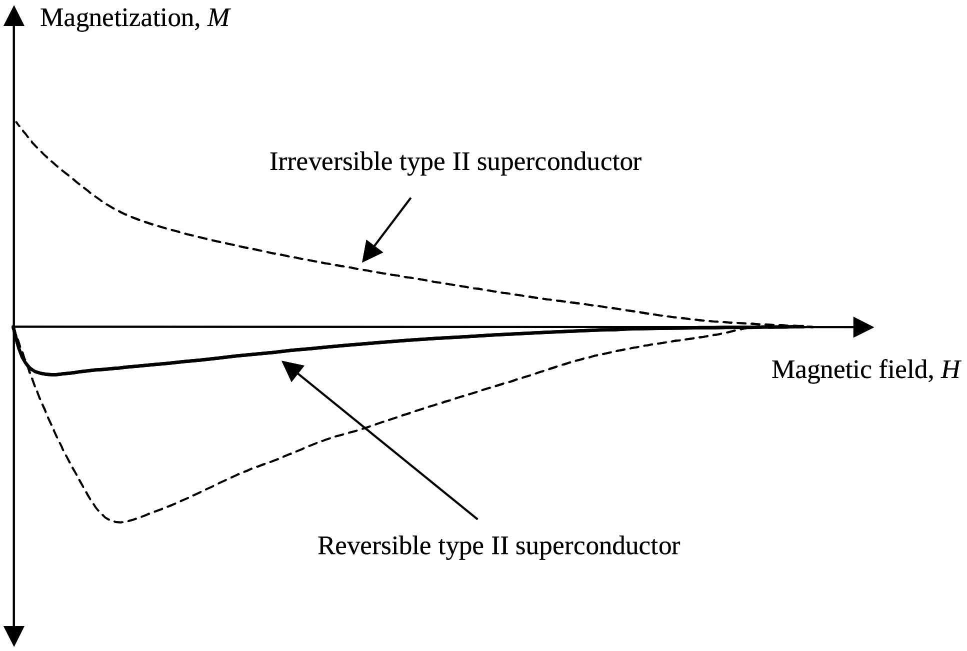

Fig. 1.3. *M*-*H* loops of irreversible and reversible type II superconductors. The area of the *M*-*H* loop (dashed one) is the hysteresis loss of an irreversible type II superconductor which has flux pinning.

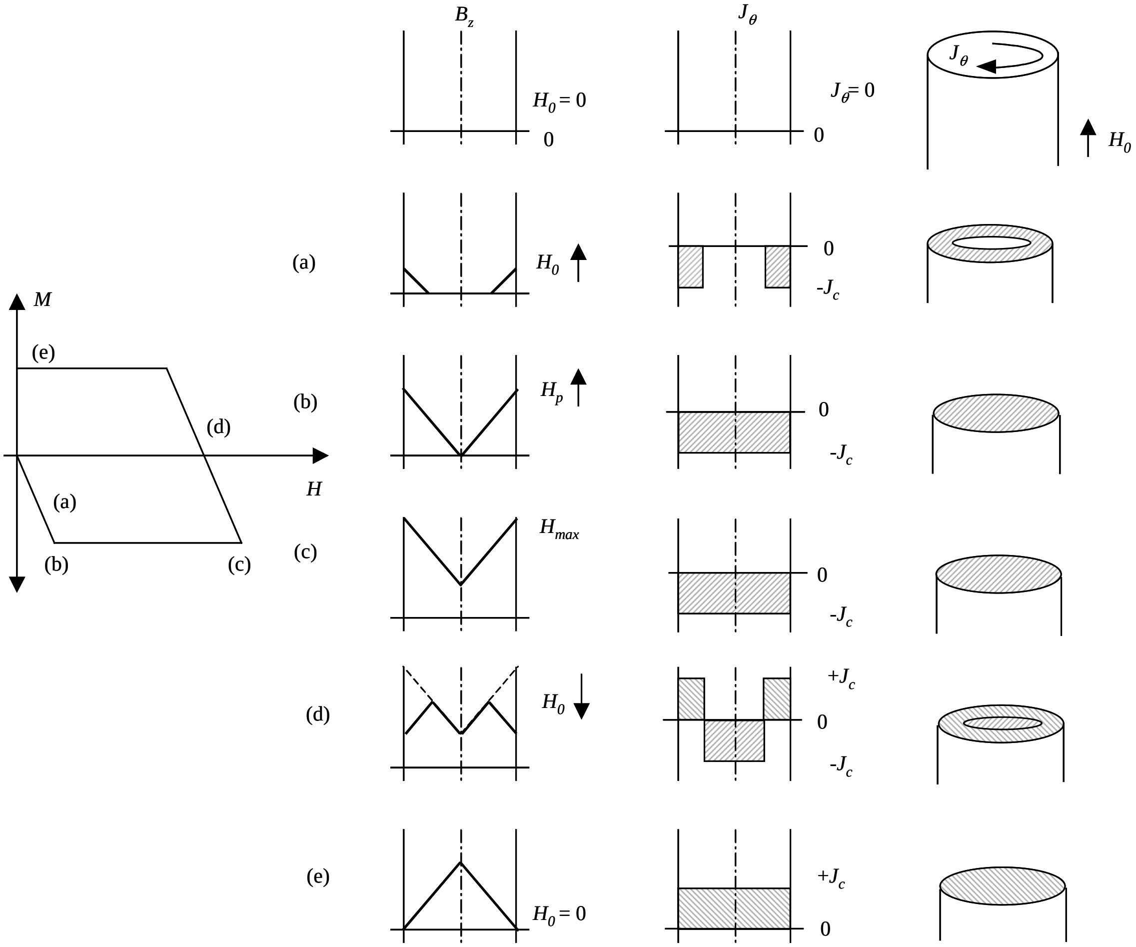

Fig. 1.4. Current distribution in a cylindrical superconductor with an infinite length when the applied field is parallel to the axis using Bean's critical state model. Here, H_p is the penetration field.

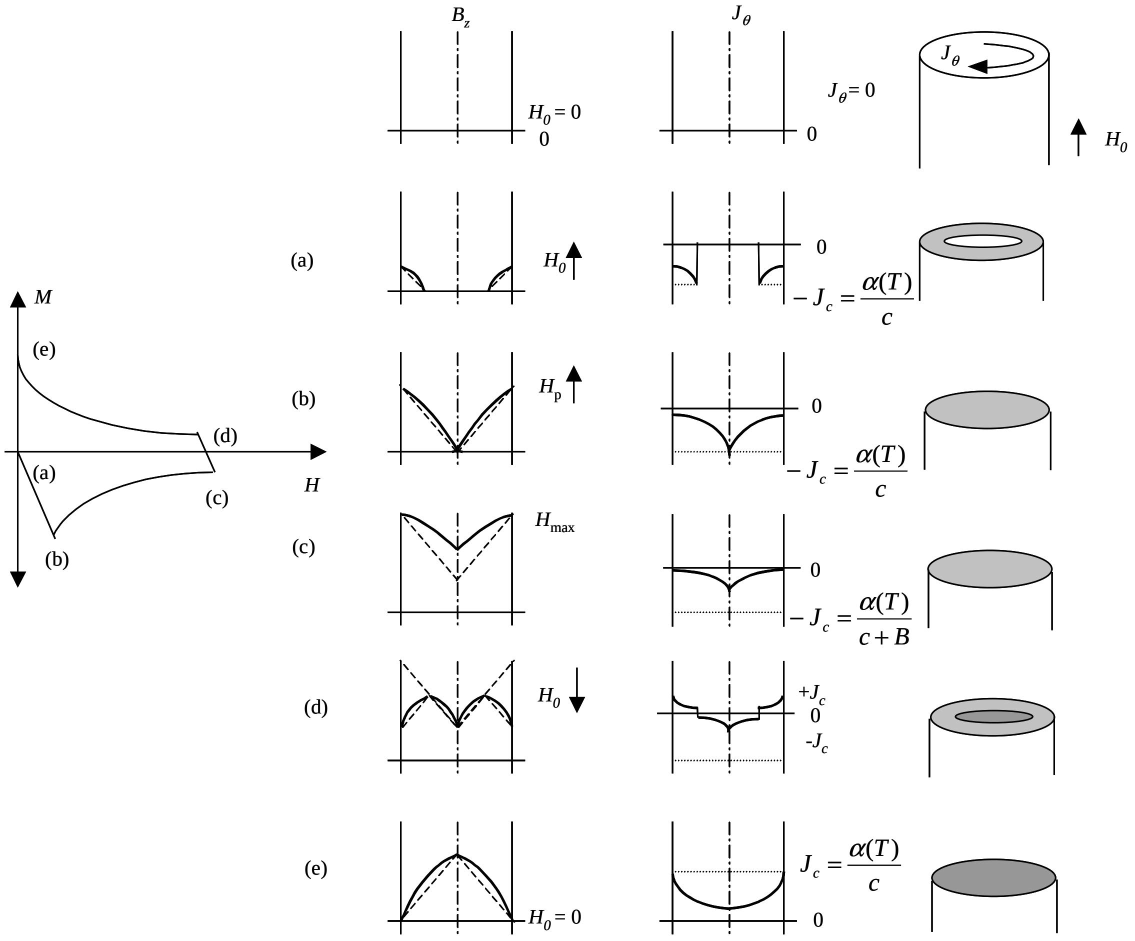

Fig. 1.5. Current distribution in a cylindrical superconductor with infinite length when the applied field is parallel to the axis using field dependent J_c (Kim’s model).

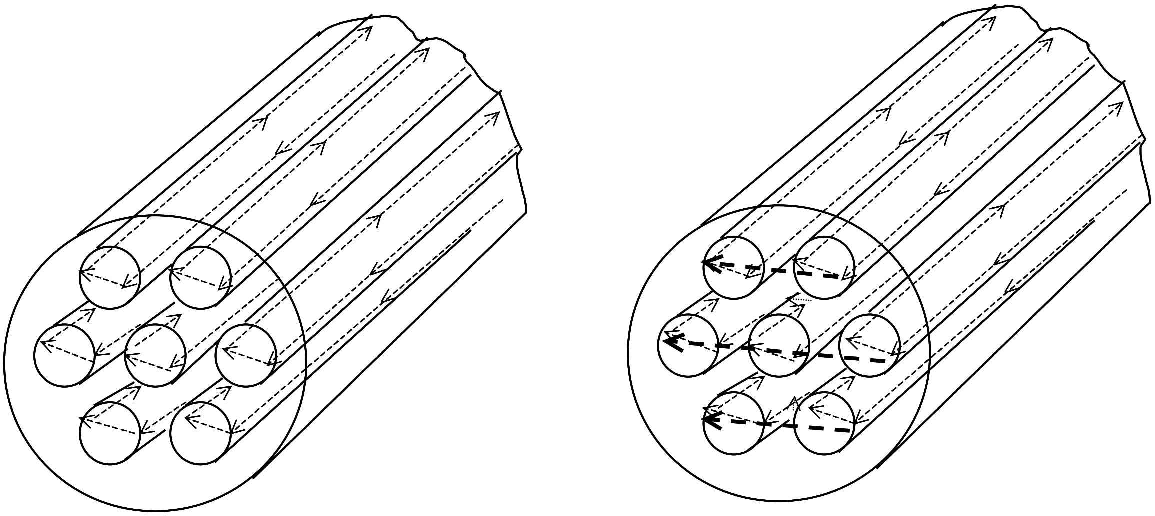

(a) (b)

Fig. 1.6. Filament coupling in superconducting composites. (a) No coupling. Super electrons flow only inside superconducting filaments. Normal eddy currents are not shown here. (b) Coupling electrons begin to flow in matrix and superconducting filaments.

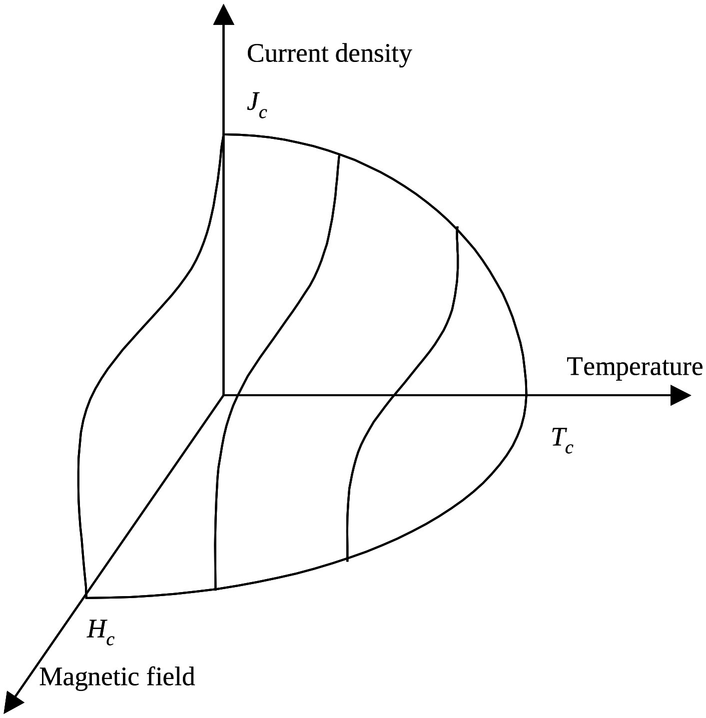

Fig. 1.7. Critical temperature, field, and current density of superconductors. Within this surface, the material is in the superconducting state.

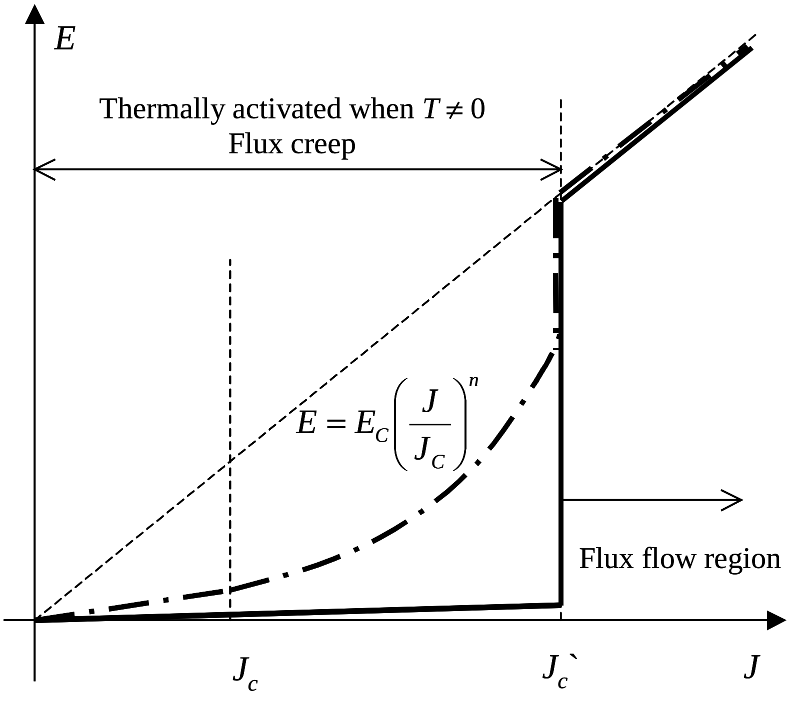

Fig. 1.8. *E-J* characteristics in the presence of flux creep. The solid line is for a low temperature superconductor while the dashed one is for a high temperature superconductor.

REFERENCES FOR CHAPTER 1

[1] G. H. Morgan, "Eddy currents in flat metal-filled superconducting braids," *Journal of Applied Physics*, vol. 44, pp. 3319-3322, 1973.

[2] W. J. Carr, *AC loss and macroscopic theory of superconductors*, 2 ed. New York: Tayor and Francis, 2001.

[3] N. Amemiya, K. Miyamoto, S. Murasawa, H. Mukai, and K. Ohmatsu, "Finite element analysis of AC loss in non-twisted Bi2223 tape carrying AC transport current and /or exposed to DC or AC external magentic field," *Physica C*, vol. 310, pp. 30-35, 1998.

[4] S. Farinon, P. Fabbricatore, F. Gomory, and E. Seiler, "Shieding and Losses in Multifilamentary Tapes Exposed to Perpendicular AC Magnetic Fields," presented at ASC 2000, Virginia Beach, VA, 2000.

[5] V. Kovachev, *Energy Dissipation in Superconducting Materials*, 1 ed. New York: Oxford University Press, 1991.

[6] E. W. Collings, *Applied superconductivity, metallurgy, and physics of titanium alloys*, vol. 1. New York: Plenum Press, 1986.

[7] K. H. Muller, "AC loss in Y-123/hastelloy superconducting tapes," presented at EUCAS'97, 1997.

[8] A. M. Campbell, "A general treatment of AC losses in multifilamentary superconductors," *Cryogenics*, pp. 3-16, 1982.

[9] V. E. Sytnikov, G. G. Svalov, S. G. Akopov, and I. B. Peshkov, "Coupling losses in superconducting transposed conductors located in changing magnetic fields," *Cryogenics*, vol. 29, pp. 926-930, 1989.

[10] V. E. Sytnikov and I. B. Peshkov, "Coupling losses for superconducting cables in pulsed fields," *Advances in cryogenic engineering*, vol. 40, pp. 537-542, 1994.

[11] A. P. Verweij, "Electrodynamics of superconducting cables in accelerator magnets,". Enschede: Twente University, 1995.

[12] W. J. Carr and V. Kovachev, "Interstrand eddy current losses in rutherford cable," *Cryogenics*, vol. 35, pp. 529-534, 1995.

[13] A. A. Akhmetov, "Compatibility of two basic models describing the AC loss and eddy currents in flat superconducting cables," *Cryogenics*, vol. 40, pp. 445-457, 2000.

[14] T. Fukunaga and A. Oota, "Hysteresis and eddy-current losses of Ag sheathed (Bi, Pb)$_2$ Sr$_2$Ca$_2$Cu$_3$O$_x$ rod-form wires under AC transport currents," *Physica C*, vol. 251, pp. 325-329, 1995.

[15] K. Kwasnitza and S. Clerc, "AC Losses of Superconducting High-T_c Multifilament Bi-2223/Ag Sheated Tapes in Perpendicular Magnetic Fields," *Physica C*, vol. 233, pp. 423-435, 1994.

[16] K. Funaki, K. Kajikawa, H. Shiraishi, M. Iwakuma, S. Miyake, T. Kumano, and T. Hasegawa, "A simple electromagnetic method of cyclic loss measurement for superconducting wires in a combined alternating transverse magnetic field and transport current," *Physica C*, vol. 310, pp. 132-136, 1998.

[17] K. Funaki, "Basic approach to AC losses in HTS wires exposed to various types of eletromagnetic configuration," *Physica C*, vol. 335, pp. 124-128, 2000.

[18] M. Ciszek, S. P. Ashworth, and B. A. Glowacki, "Transport AC losses in multifilamentary Ag/Bi-2223 tapes in low external DC magnetic fields," *Physica C*, vol. 272, pp. 319-325, 1996.

[19] M. Ciszek, A. M. Campbell, S. P. Ashworth, and B. A. Glowacki, "Energy dissipation in high temperature ceramic superconductors," *Applied Superconductivity*, vol. 3, pp. 509-520, 1995.

[20] V. Sokolovsky, V. Meerovich, S. Goren, and G. Jung, "Analytical approach to AC loss calculation in high T_c superconductors," *Physica C*, vol. 306, 1998.

[21] K. Yamafuji, T. Wakuda, and T. Kiss, "Generalized critical state model in high-T_c superconductors," *Cryogenics*, vol. 37, pp. 421-430, 1997.

[22] T. Wakuda, T. Nakano, M. Iwakuma, K. Funaki, M. Takeo, K. Yamafuji, Y. Yamada, and S. Yasuhara, "*E-J* chracteristics and AC losses in a superconducting Bi(2223) hollow cylinder," *Cryogenics*, vol. 37, pp. 381-388, 1997.

[23] C. H. Cheng, Y. Zhao, and H. Zhang, "Thermal diffusion and AC loss in high T_c superconductors," *Physica C*, vol. 337, pp. 239-244, 2000.

[24] M. Iwakuma, Y. Tajika, K. Kajikawa, K. Funaki, T. Matsushita, E. S. Otabe, N. Ayai, K. Hayashi, and K. Sato, "Twist effect on hysteresis loss in Bi2223 multifialmentary wires exposed to an AC magnetic field," *Physica C*, vol. 310, pp. 154-158, 1998.

[25] T. P. Sheahen, *Introduction to high temperature superconductivity*, 1 ed. New York: Plenum Press, 1994.

[26] E. Lee, M. D. Sumption, and E. W. Collings, "Temperature and field dependence of the effective matrix resistivity of Bi:2223/Ag composites," *IEEE transactions on applied superconductivity*, vol. 13, pp. 3614, 2003.

[27] K. Kanbara, "Hysteresis loss of a round superconductor carrying a d.c transport current in an alternating transverse field," *Cryogenics*, vol. 27, pp. 621-630, 1987.

[28] E. W. Collings, K. R. Marken, M. D. Sumption, J. R. Clem, S. A. Boggs, and M. V. Parish, "AC loss and dynamic resistance of a high T_c strand carrying a direct current in a tranverse AC magnetic field," presented at CEC/ICMC, Huntsville, AL, 1991.

[29] S. A. Boggs, E. W. Collings, and M. V. Parish, "AC losses in HTSC conductor elements," *IEEE transactions on applied superconductivity*.

[30] M. Oomen, J. Rieger, M. Leghissa, B. Fischer, and T. Arndt, "Decease of magnetic AC loss in twisted-filament Bi-2223 tapes," *Physica C*, vol. 310, pp. 137-141, 1998.

[31] M. Oomen, J. Rieger, M. Leghissa, B. T. Haken, and H. H. J. ten Kate, "Dynamic resistance in a slab-like superconductor with $J_c(B)$ dependence," *Supercond. Sci. Technol.*, vol. 12, pp. 382-387, 1999.

[32] M. N. Wilson, *Superconducting magnets*, 1 ed. New york: Oxford University Press, 1983.

[33] Y. Yang, T. Hughes, C. Beduz, and F. Darmann, "Experimental study on AC losses in Ag sheathed PbBi2223 tapes with twist filaments," *Physica C*, vol. 310, pp. 147-153, 1998.

[34] E. Martinez, Y. Yang, C. Beduz, and Y. B. Huang, "Experimetal study of loss mechanisms of AgAu/PbBi-2223 tapes with twisted filaments under perpendicular AC magnetic fields at power frequencies," *Physica C*, vol. 331, pp. 216-226, 2000.

[35] T. Hughes, F. Darmann, J. Horvat, and S. X. Dou, "Reduction of the AC losses in Ag sheathed PbBi2223 tapes with twisted filaments," *Physica C*, vol. 325, pp. 77-82, 1999.

[36] H. Eckelmann, M. Quilitz, C. Schmidt, W. Goldacker, M. Oomen, and M. Leghissa, "AC losses in multifilamentary low AC loss Bi(2223) tapes with novel interfilamentary resistive carbonate barriers," presented at Applied Superconductivity Conference, Palm Springs, CA, 1998.

[37] F. Darmann, R. Zhao, G. McCaughey, M. Apperley, and T. P. Beals, "AC losses of filamentary HTS twisted filaments round wires and flat tapes,",, 1998.

[38] S. Fukui, O. Tsukamoto, and K. Negishi, "AC loss of low temperature superconducting AC wire caused by longitudinal and azimuthal AC magnetic field components," *Physica C*, vol. 310, pp. 142-146, 1998.

[39] N. Banno and N. Amemiya, "Numerical analysis of AC loss in high T_c twisted tape carrying AC transport current in external AC magnetic field - effect of twisting on loss reduction," presented at Applied superconductivity Conference, Palm Desert, CA, 1998.

[40] E. W. Collings, "Stabilizer design considerations in fine-filament Cu/Nbti composites," *Advances in Cryogenic Engineering Materials*, vol. 34, pp. 867-878, 1988.

[41] M. D. Sumption and E. W. Collings, "Transverse resistivities of Cu-matrix and Cu-Mn matrix multifilamentary strands as fuctions of magnetic field and temperature," presented at CEC-ICMC93, Albuquerque, NM, 1993.

[42] M. Dhalle, A. Polcari, F. Marti, G. Witz, Y. B. Huang, R. Flukiger, S. Clerc, and K. Kwasnitza, "Reduced filament coupling in Bi(2223)/$BaZrO_3$/Ag composite tapes," *Physica C*, vol. 310, pp. 127-131, 1998.

[43] H. Eckelmann, J. Krelaus, R. Nast, and W. Goldacker, "AC losses of multifilamentary Bi(2223) tapes in external perpendicular magnetic fields with different internal resistive barrier structure betwwen the filaments," presented at EUCAS'99, Sitges, Spain, 1999.

[44] J. Krelaus, R. Nast, H. Eckelmann, and W. Goldacker, "Novel, internally stranded "Ring Bundled Barrier" Bi-2223 tapes for low AC loss applications," presented at EUCAS'99, Sitges, Spain, 1999.

[45] K. Kwasnitza, S. Clerc, R. Flukiger, and Y. B. Huang, "Reduction of alternating magnetic field losses in high T_c multifilament Bi(2223)/Ag tapes by high resistive barriers," *Cryogenics*, vol. 39, pp. 829-841, 1999.

[46] V. Lennikov, H. Caudevilla, L. A. Angurel, G. F. de la Fuente, and R. Navarro, "Development of Ag sheathed Bi-2223 Multifilamentary tapes with MgO Coated Filaments,",, 1998.

[47] P. X. Zhang, R. Inada, T. Uno, Y. Takatori, A. Oota, H. Fujimoto, P. Ji, Z. Z. Duan, C. S. Li, H. L. Zheng, and L. Zhou, "Fabrication and transport AC losses of (Bi,Pb) 2223 multifilamentary tapes with resistive barriers," presented at Applied Superconductivity Conference, Virginia Beach, VA, 2000.

[48] W. J. Carr, *AC loss and macroscopic theory of superconductor*, 1st ed. New York: Gordon and Breach, 1983.

[49] B. Seeber, *Handbook of applied superconductivity*, vol. 1: IOP Publishing, 1998.

CHAPTER 2

NUMERICAL METHODS

The calculation of the electromagnetic fields within finite size, three-dimensional objects cannot be performed easily by analytic methods under fully general conditions particularly for the case of materials with anisotropic properties which have principle anisotropy axes non-aligned with the sample dimensions. In this study, some of the models developed are tested using numerical methods, in particular FEM (Finite-Elements-Method) commercial software (Maxwell 3D). The details and basic principles of FEM for electromagnetic fields can be found in other references[1, 2], below a general description of the use of commercial software packages is presented.

2.1 Conductivity ratio limit

For proper simulations, the conductivity along the filamentary or strand direction within the composite should be as large as possible. However, due to the computational capacity of presently available hardware and software, the conductivity value in the superconducting direction was chosen to be 10^{12} S/m. More important than this is that difference in conductivity between the superconducting direction and the normal conducting direction should be as large as possible. Optimally, this difference is 10^6 – 10^8 S/m[3, 4]. Therefore, 10^6 S/m was chosen for the normal conducting direction. The conductivity of the vacuum surrounding the sample is fixed at zero. The maximum allowable conductivity difference between the highest and lowest conductivity regions defined within the available software and hardware turned out to be 10^{12} S/m.

If an anisotropy of conductivity tensor within normal metal region becomes larger, that is a conductivity of filamentary direction becomes much larger than a conductivity of transverse direction, then, the loss in this region approaches the loss value of the superconducting composite with superconducting filaments and normal metal matrix[5]. This indicates that a conductivity difference of 10^6 S/m between the superconducting filament direction and the transverse direction is sufficient to obtain sound numerical results for superconducting composites. The relationship between the base coordinate system and the sample geometry-based coordinate system is shown in Figure 2.1, and the definition of conductivity tensor in each region is given in Table 2.1. Definitions for both the four-block model and the core model are shown.

Nevertheless, if the conductivity difference is too large, numerical instability will occur[4, 6]. To preclude this, numerical instability was tested for by two criteria in this study. First, the results were checked for discontinuities, a clear sign of numerical instability. Secondly, the invariance of the result with increasing mesh refinement was required.

2.2 Geometry and mesh size

The eddy current loss in a Rutherford cable shows a saturation behavior with respect to L_s/L_p when sample length is larger than five times the twist pitch[7]. Here, L_s is sample length and L_p is twist pitch. Thus, we set $L_s/L_p > 5.7$.

The size of the surrounding vacuum box must be large enough to keep the demagnetizing field surrounding the sample from interfering with the boundary conditions. If the surrounding sample box is too small, the correct solution will not be obtained. But, as the region grows, we need a finer mesh requiring greater computing capability. When the sample is a long rectangular shape with a size of 300 x 15 x 4 mm, the size of the surrounding vacuum box is 500 x 300 x 300 mm. The average number of nodes for this model is shown in Table 2.2. The size of the surrounding vacuum box is 300 x 60 x 60 mm when the sample is a long cylindrical shape with dimensions of 200 mm length by 4 mm radius. The superconducting composite region has a finer mesh as compared to the surrounding vacuum region. An example of a sample geometry and its associated mesh is shown in Figure 2.2.

2.3 Boundary setup

In a quasi-static field, the magnetic vector potential, $\boldsymbol{A}$ should be properly defined at the outer boundary of the surrounding vacuum box in order to produce a uniform, time-harmonic magnetic field. In Maxwell 3D software, it was not necessary to input the specific value of $\boldsymbol{A}$, since it automatically defines that value at the outer boundaries when we specify the applied magnetic field. Since the field is time-harmonic, non-linear problems cannot be considered by the method used in the present study.

The effective permeability of the superconducting composite is assumed to be 1.0, since we are considering the case of full field penetration. Hysteretic components are not computed in the eddy current calculation, these can be added separately.

2.4 Solver type

There are two solver types in the Maxwell 3D software package, a direct solver and an iterative solver. The iterative solver, requiring less computing memory stops its iteration when the relative error (the difference between the previous solution and the current solution) is smaller than a predetermined error limit, for example, 10^{-8}. However, it frequently fails to converge for models with conductivity differences as high as 10^{12} S/m as in this study, and thus the direct solver was used.

2.5 Loss calculation method

After the current distribution was calculated from FEM, the AC loss, especially the eddy current coupling loss, could be calculated by either of two methods. First, the loss can be calculated by using

$$P = \int_V J \cdot E dV = \int\int_V J \cdot \frac{1}{\sigma} \cdot J dV \tag{2-1}$$

Since we have a finite conductivity (10^{12} S/m) in the superconducting direction, (2-1) has non-zero contribution only along the normal conducting direction, the *z* direction in the present study. This direction is perpendicular to the axis of the "length" of the superconducting composites and parallel to the applied magnetic field. To calculate average power loss, we calculate the loss at a phase angle of 90°, and then multiply it by 0.5[6].

The second method is to calculate magnetization, *M* using

$$M = \int_V r \otimes J dV = \int_V \begin{vmatrix} i & j & k \\ x & y & z \\ J_x & J_y & J_z \end{vmatrix} dV$$

$$= \int_V \left(i(J_z \cdot y - J_y \cdot z) - j(J_z \cdot x - J \cdot z) + k(J_y \cdot x - J_y \cdot y) \right) dV$$

$$= M_x \cdot i + M_y \cdot j + M_z \cdot k \qquad (2\text{-}2)$$

Since the applied magnetic field has a *z* component only, it is sufficient to calculate M_z contributions only.

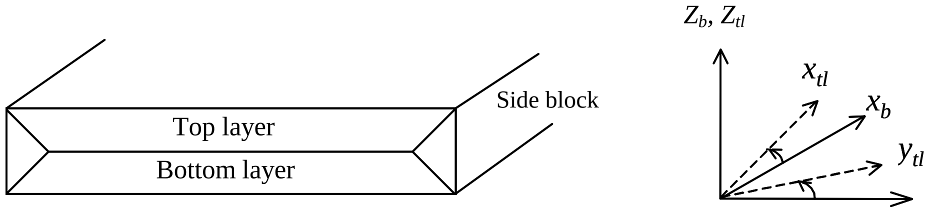

Four-block model

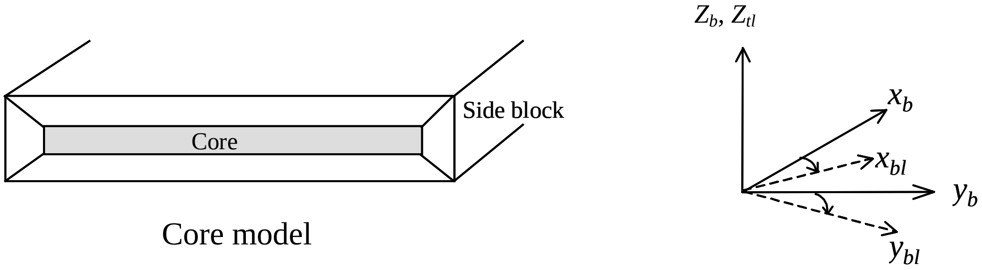

Core model

Fig. 2.1. The relationship between the base coordinate system and the sample geometry-based coordinate system. x_b,y_b, and z_b are the base coordinates and x_{tl},y_{tl}, and z_{tl} are the sample geometry-based coordinates within top layer. x_{bl},y_{bl}, and z_{bl} are the sample geometry-based coordinates within the bottom layer. Within the side blocks, both coordinate systems are identical.

Block	Four-block model	Core model
Top layer	$\sigma_{xx} = 10^{12}$ (S/m) $\sigma_{yy} = \sigma_{zz} = 10^{6}$ (S/m) x_{tl}, y_{tl}, z_{tl} are rotated around z_b such that x_{tl} now lies along the filamentary direction defined by L_p (+ rotation)	same
Bottom layer	$\sigma_{xx} = 10^{12}$ (S/m) $\sigma_{yy} = \sigma_{zz} = 10^{6}$ (S/m) x_{bl}, y_{bl}, z_{bl} are rotated around z_b such that x_{bl} now lies along the filamentary direction defined by L_p (- rotation)	same
Left and right side block	$\sigma_{xx} = 10^{6}$ (S/m) $\sigma_{yy} = \sigma_{zz} = 10^{12}$ (S/m) $x_s, y_s, z_s = x_b, y_b, z_b$	same
Core	N.A.	$x_c, y_c, z_c = x_b, y_b, z_b$ Isotropic $\sigma = 10^4$-10^6 (S/m)

Table 2.1. Definitions of axes and the conductivity tensor for the four-block model.

	Four-block model	Core model	Cylinder model	Seven-strand model
Surrounding vacuum	17000	14000	20000	3500
Top & Bottom layer	13500 x 2	9500 x2	Each 4 block has about 10000	Each 8 block has about 2500 and core region has about 10000
Left & Right block	3500 x2	3000 x2		
Core	--	10000		
Total	≈50000	≈50000	≈60000	≈35000

Table 2.2. Number of tetrahedrons in each block region.

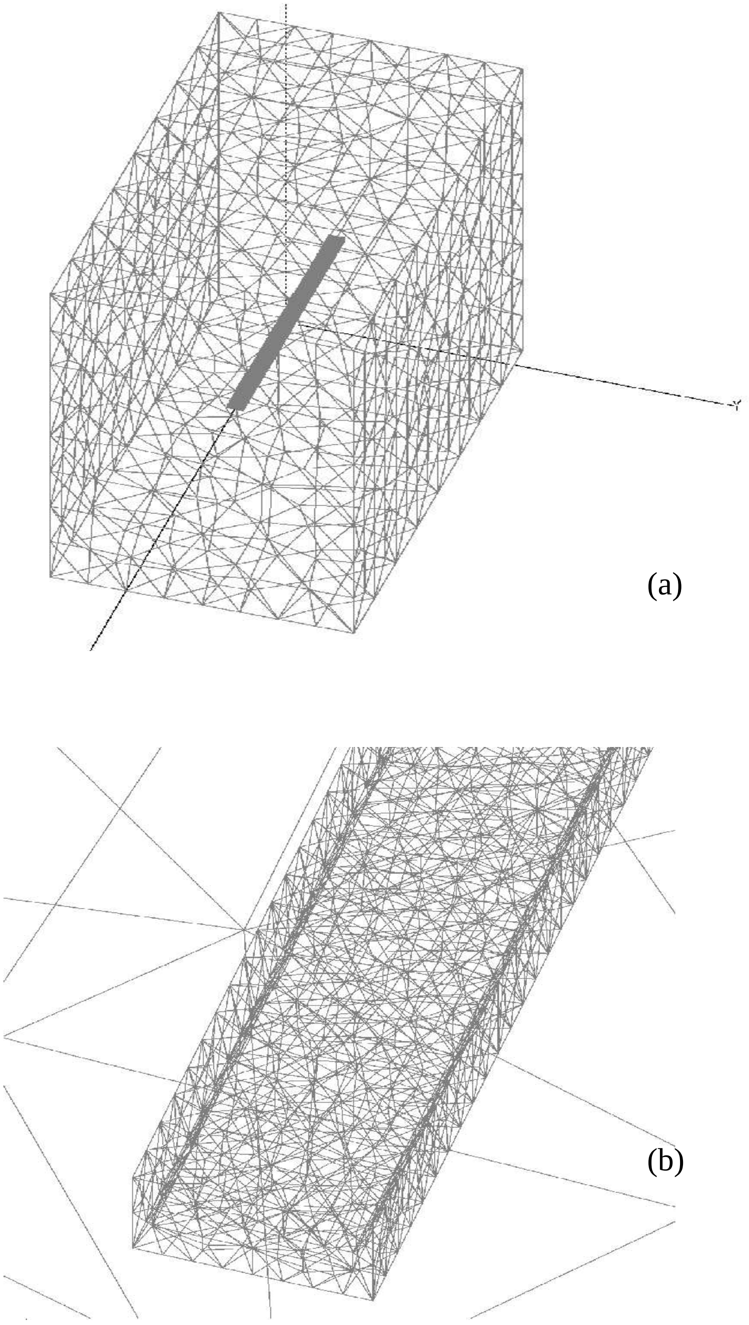

Fig. 2.2. Example of sample geometry and mesh. (a) An example of a selected sample geometry and its associated mesh in the case of four-block and core models. (b) The mesh of the sample region is finer than that of the surrounding regions.

REFERENCES FOR CHAPTER 2

[1] J. Jin, *The finite element method in electromagnetics*: John wiley & Sons, 1993.

[2] P. P. Silvester and R. L. Ferrari, *Finite elements for electrical engineers*, 3 ed: Cambridge university press, 1996.

[3] N. Amemiya, K. Miyamoto, N. Banno, and O. Tsukamoto, "Numerical analysis of AC losses in high T_c superconductors based on *E-J* characteristics represented with n-value,",, 1997.

[4] N. Amemiya, S. Murasawa, N. Banno, and K. Miyamoto, "Numerical modelings of superconducting wires for AC loss calculations," *Physica C*, vol. 310, pp. 16-29, 1998.

[5] G. B. J. Mulder and E. M. J. Niessen, "Coupling losses of multifilamentary superconductors having several concentric regions and mixed matrix,", Chicago, IL, 1992.

[6] COMSOL, *FEMLAB 2.3 Eletromagnetic module manual*: COMSOL AB, 2002.

[7] A. P. Verweij, "Electrodynamics of Superconducting Cables in Accelerator Magnets,". Enschede: Twente University, 1995.

CHAPTER 3

EXPERIMENTAL METHODS

3.1. Sample specification

3.1.1 Hysteresis losses in samples with magnetic shielding effects

Two different MgB_2 composite strand types were measured in this work. The first strand type was manufactured by the University of Wollongong using standard powder-in-tube methods. The starting tube was Fe with an outside diameter of 10 mm, a wall thickness of 1 mm, and was 10 cm long. Magnesium (99% purity) and amorphous boron (99%) with the stoichiometry of MgB_2 were mixed together and used to fill the tube. After wire drawing the strand was sintered in a tube furnace, where T ranged from 600 to 1000 °C for 1–48 h[1]. A high purity argon gas flow was maintained throughout the sintering process. For comparison a sintered MgB_2 sample with no Fe sheath was prepared with dimensions $0.35 \times 0.65 \times 0.174$ cm^3.

The second strand type was manufactured by Hyper Tech Research. These strands were made by a CTFF (Continuous Tube Forming and Filling) method. Magnesium (99% purity) and amorphous boron (99%) with the stoichiometry of MgB_2 were mixed and then slightly mechanically alloyed, after which the powder was filled into a thin Fe tube formed from a strip during filling. This rod was then inserted into a monel tube 6 mm OD and then drawn to final size.

Both types of MgB_2 strands with different heat treatments and power compositions were measured at 4.2 K using a 9 T VSM. Details of sample specifications are listed in Table 3.1.

3.1.2 Samples for contact resistance and AC loss measurements

Seven strand MgB_2 cables with a 1 + 6 geometry (one central strand surrounded by six other strands) were fabricated by Hyper Tech Research. The individual strands were made by the CTFF method. Before twisting the strands, various insulation methods such as oil dipping and high temperature painting were applied. Then, they were heat treated at 700 –750 °C for 15 to 30 minutes in flowing argon gas. Details of sample specifications are given in Table 3.2. The contact resistance between each of the strands within a given cable was measured by four point method at 4.2 K in liquid He. To insure an "averaged" measurement, the sample length was more than 11.5 cm at minimum. By the symmetry of the cable, we need to measure only four contact resistances between specific strands for a given cable, as shown in Fig. 3.1. (Between 1 and 2(R_1), 1 and 3(R_2), 1 and 4(R_3), 1 and 5(R_4)). A 0.5 A DC current was applied to the current leads and the voltage was measured. After this, the polarities of the current were reversed and the voltage was measured again. After averaging the absolute values of the voltages and dividing by 0.5 A, the contact resistance between strands was obtained.

3.2. VSM (Vibrating Sample Magnetometer)

3.2.1. 1.7 T VSM

A VSM (Vibrating Sample Magnetometer) measures the magnetic moment of a sample. A slowly ramping (nearly static) magnetic field is applied to the samples, the sample itself vibrates, and the magnetic moment of sample is detected by a pick-up coil. The voltage signal of the pick-up coil is proportional to the magnetic moment of the sample. After integration of the voltage signal coming from the pick-up coil with respect to time, the magnetization can be calculated, and an *M-H* loop is generated. This signal is calibrated against the saturation magnetization of a Ni standard. The area of the *M-H* loop is the AC loss of the sample per cycle.

In this experiment, a VSM model 4500 from EG&G was used. The schematic and the photograph of the 1.7 T VSM are shown in Fig. 3.2 and Fig. 3.3. Magnetic fields up to ±1.7 T generated by a water cooled resistive magnet were applied to the sample space. The current needed for the magnet was supplied by a “DC” bi-polar power supply. The magnetic field sweep rate could be varied from 2.4×10^{-3} to 7.0×10^{-2} T/sec, which is a much lower frequency range than that of the pick-up coil method to be described in the following section. The applied magnetic field was measured by a Hall sensor located near the sample.

The temperature of the sample can be controlled by adjusting the opening of a needle valve connecting the He-reservoir with the sample measuring space, in conjunction with a heater which can vaporize and heat the helium within the sample space. The temperature can range from 4.2 K to room temperature. A temperature sensor was attached to just above the sample in order to measure the temperature as accurately as possible. Previous measurements show this to be accurate to within a tenth of a degree. If we pump the sample space, temperatures as low as 2.2 K are possible. The orientation of sample can be changed by rotating the VSM head which vibrates the sample. Therefore, we can apply a magnetic field at an arbitrary angle to the wide surface of the sample. The maximum sample length that can be measured in 1.7 T VSM is about 1.6 cm because of the size of the pick-up coil and the size of the sample space. When we affix the sample to the sample holder for use at low temperatures, we use silicon grease and teflon tape.

3.2.2. 9 T VSM

In order to measure tapes, wires and cables, a system which would allow larger samples was needed. Most VSM systems are made to measure small samples. However, in the course of this work a VSM-type machine capable of measuring larger samples was developed. It was built using a 9 T magnet in order to have a larger available field, so it became designated the “9 T VSM”. The magnet itself is a NbTi superconducting magnet operating at 4.2 K, in a liquid He cryogenic system with a liquid nitrogen outer jacket. A maximum magnetic field sweep rate of 0.0375 T/sec is possible. Since the magnetic field sweep rate is relatively low, we cannot measure the eddy current coupling loss with the 9 T VSM. However, the hysteric components can be measured.

A schematic of the pick-up coil for 9 T VSM is shown in Fig. 3.5. 40 gauge copper wire was wound onto a G10 coil former, after which GE varnish was applied to protect the coil. GE varnish is a standard low temperature insulation, because commercial epoxy will crack at LHe temperatures. A maximum sample length of 3 cm can be measured with this pick-up coil arrangement.

Since the sample rod (6 ft.) is about 2 times longer than that of the 1.7 T VSM, locating the sample at the center of the pick-up coil as precisely as possible is essential to obtaining a sound *M-H* loop. A small sample coil was made to find this exact location along the axis *z*. A current was impressed to the sample coil, and the magnetic moment of the sample coil was measured as a function of position within the pick-up coils. By finding the maximum of the response curve generated in this way, the proper *z*-axis position of the sample was determinded. The results are displayed in Fig. 3.6. The sensitivity of pick-up coil at various points in *x-y* plane can be determined by measuring the magnetic moment of several sample coils with different lengths. The result of measurements of the length dependence of magnetic moment in *x-y* plane were displayed in Fig. 3.7. The schematic of the sample coil is shown in Fig. 3.8. The width of the sample coil and the number of turns are the same for all sample coils and only the length is changed. All sample geometries are calibrated using a Ni standard of the same shape as the sample.

Since the sample space of the 9 T VSM is much larger than that of 1.7 T VSM, frozen N_2 and O_2 can more readily formed inside the sample space, and this can interfere with the vibration of the sample. If this occurs, a sound *M-H* loop cannot be obtained. To prevent this, it is important to fill the sample space with He gas, pumping out all other gases from the sample space before opening the needle valve and evaporating the liquid He.

3.2.3. Pick-up coil method

The pick-up coil measurement system in this experiment was initially modeled after that of Kyushu University[2]. However, there were numerous modifications including some to the AC power circuit as well as the geometry of pick-up and cancel coil, and the mode of signal cancellation. In the pick-up coil method, the sample does not vibrate. However, the magnetic field experienced by the sample varies with time at a much larger rate than in the VSM. To generate a magnetic field of 0.1 T in a external magnet wound with 1510 turns, having a self inductance of 90 mH, and an area of 6.21 $\times 10^{-3}$ m^2, a current of 10.41 A is required,

$$B = \frac{L \cdot I}{N \cdot A_m} \ , \qquad I = \frac{B \cdot N \cdot A_m}{L} = \frac{0.1 \times 1510 \times \pi (4.445 \times 10^{-2})^2}{90 \times 10^{-3}} = 10.41 \text{ ampere.}$$

Here, A_m is the cross sectional area of the external magnet (primary coil). The external magnet has an inductance (L) and a resistance (R). To maximize the field, we had to add a capacitance (C), making a R-L-C circuit with minimum impedance at any given frequency. The resonant frequency of a R-L-C circuit in series is given by $\omega_0 = \frac{1}{\sqrt{L \cdot C}}$.

The needed capacitance at the given frequency is then $C = \frac{1}{L \cdot \omega^2}$. We chose several frequencies and then calculated the needed capacitance values. The total impedance of this R-L-C circuit was then given by $Z = \sqrt{R^2 + (X_L - X_C)^2} \approx \sqrt{(X_L - X_C)^2}$. Here, $X_L = \omega L = 2\pi f L$ and $X_C = 1/(\omega C) = 1/(2\pi f C)$. The impedance Z at different frequencies using several values of capacitance is displayed in Fig. 3.9. With a maximum voltage output of the AC power supply at 150 volts and the required current 10.41 ampere, an impedance below 14.4 ohm is enough to generate a magnetic field up to of 0.1 T. That the field distribution inside the external magnet should be uniform was confirmed using a numerical calculation, the results of which are shown in Fig. 3. 10.

The sample, now immersed in field, shields this field to some extent. The level of shielding determines the resulting *B*, which can be measured by a pick-up coil wrapped around the sample. The voltage signal measured by the pick-up coil contains the voltage signal generated by the external time-varying magnetic field. This signal must be cancelled using the canceling coil. The geometry and the number of turns of the pick-up coil and the cancel coil are nominally identical and they are located symmetrically within the external magnet. The schematic of the electrical circuit of this experiment is shown in Fig. 3.11. To damp the oscillations in the pick-up and cancel coils a 100 Ω resistance was connected in series to both pick-up and cancel coils. A resistance divider network connected in parallel to the pick-up coil was used to fine tune the compensation. To measure the magnetic field amplitude, an additional pick-up coil was inserted as shown in Fig. 3.11. The dimensions of all pick-up coils as well as the external magnet coil are displayed in Table 4.

The applied magnetic field and the sample magnetization are given by the integration of voltage signal from each measuring coil as follows[2, 3]

$$H(t) = c \cdot \int V_f(t)dt \ ,$$

$$M(t) = c \cdot \int V_{p-c}(t)dt$$

Here, c is a constant dependent on the number of turns of the coil and the cross sectional area of the coil. $V_f(t)$ is the voltage signal from the magnetic field measuring coil and $V_{p\text{-}c}(t)$ is the voltage signal from pick-up coil after cancellation. The data from the oscilloscope are numerically integrated using a commercial software package (Sigma plot 8.0).

After all measurements, the voltage signals for the magnetic moments are measured again without the samples under the same conditions to estimate the error in the system. This error comes from the incomplete cancellation of the voltage from the pick-up and canceling coils. Perfect cancellation is almost impossible in practice since small variations in pick-up and cancel coil symmetry will occur due to the winding process. The error signals are determined and then subtracted from each initial voltage signal from the pick-up coil and $M(t)$ is given by numerical integration of these signal after the subtraction.

The generated magnetic field amplitude can be checked from the voltage signal of the field measuring coil using $V = \frac{-Nd(B \cdot A_c)}{dt} = \frac{-N \cdot A_c dB}{dt}$. If the cosine waveform of $K\cos(\omega t)$ is assumed for the voltage signal, then $K\cos(\omega t) = \frac{-N \cdot A_c dB}{dt}$ and therefore, $B = -\frac{K}{N \cdot A_c \cdot \omega}\sin(\omega t)$. Here, N is the number of turns of the field measuring coil, A_c is the cross section area of that coil and K is a constant. For example, A_c is $\pi \times (8 \times 10^{-3})^2$, N is 721 and K is 9.6994 at 75 Hz by fitting the voltage signal data to a cosine waveform.

Then, the maximum field amplitude *B* is 0.142 T and an *rms* magnetic field of 0.1 T is generated, as expected.

Finally, the voltage signal for sample magnetization was calibrated. This can be done either by using a standard sample with a known magnetic property or using small sample coils with a known number of turns and cross sectional area. We chose pure iron (Fe) which is a soft magnetic material. Several Fe strips were measured together using the 1.7 T VSM as well as the pick-up coil method. After normalizing with respect to the weight of the Fe strips, the sample magnetization was calibrated. The result of calibration is shown in Fig. 3.12. The conversion factor was 508.83. Since the Fe strips were measured with the wide surface of the Fe strips perpendicular to the magnetic field, the *M*-*H* loops show some demagnetizing effect. But, it was assumed that deviation from complete saturation was the same for both the 1.7 T VSM measurements and the pick up coil method.

Sample Name	Heat treatment	Structure	Manufactures
DMGB1	800 °C, 30 min.	MgB_2 / Fe	U. of Wollongong
DMGB3	1000 °C, 30 min.	MgB_2 / Fe	
DMGB4	800 °C, 30 min.	(MgB_2 + C) / Fe	
DMGB6	1000 °C, 30 min.	(MgB_2 + C) / Fe	
OSU225	700 °C, 15 min.	(MgB_2 + SiC) / Fe /Monel	Hyper Tech Research
OSU226	700 °C, 15 min.	MgB_2 / Fe /Monel	

Table 3.1. Sample specifications for the 9 T VSM.

Sample Name	Powder batch	Twist pitch/length, cm	Insulation method	Heat treatment
MOT01	MgB_2, #205 (Fe/monel)	4.445/11.5	Motor oil (Mobil #1 SAE30)	750 °C 30 min.
GEO02		5.08/17.0	Gear oil (Pennzoil, SAE80W-90GLS)	
NOS03		4.445/12.5	No insulation	
PAT04		4.445/14.5	Paint (POR15)	
GEO05		4.445/13.5	Gear oil (Pennzoil, SAE80W-90GLS)	
FMO06	MgB_2, #152 (Fe/monel)	5.08/16.0	No insulation	700 °C 15 min.
FMO07		3.81/16.0		
FMO08		2.54/16.0		
NOF09	MgB_2, #270 (No Fe/monel)	5.08/16.0		
NOF10		3.81/16.0		
NOF11		2.54/16.0		
CUC12	MgB_2 + SiC (10%), #256A, (Fe/CuNi)	5.08/16.0		
CUC13		3.81/16.0		
CUC14		2.54/16.0		

Table. 3.2. MgB_2 cable specifications for contact resistance measurements.

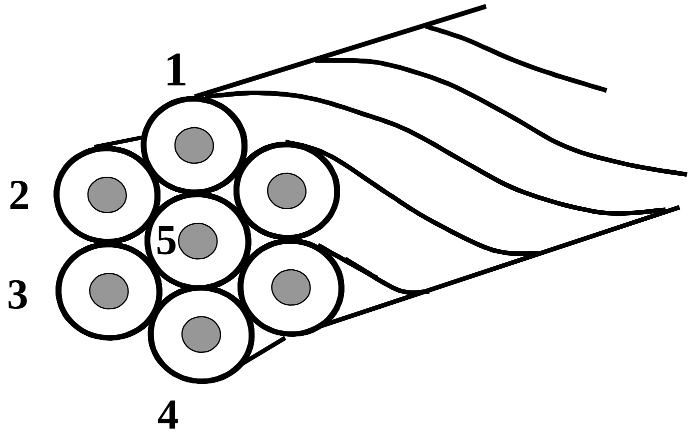

Fig. 3.1. Seven strand MgB_2 cables with a 6 + 1 geometry.

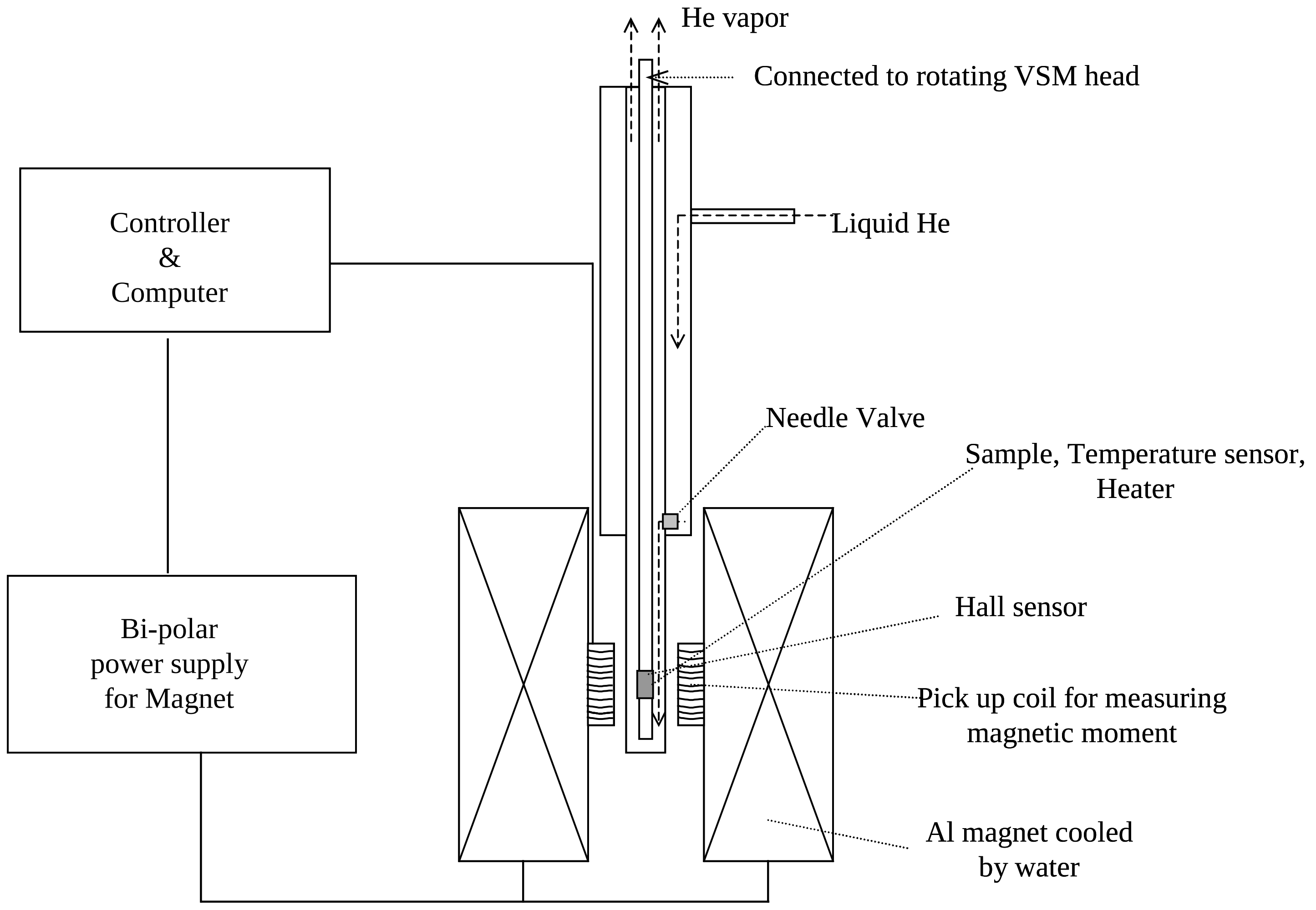

Fig. 3.2. Schematic of the 1.7 T VSM (Vibrating Sample Magnetometer).

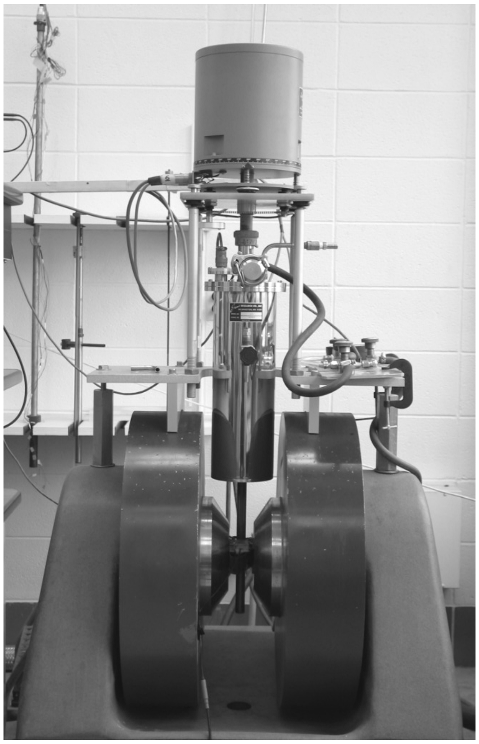

Fig. 3.3. 1.7 T VSM.

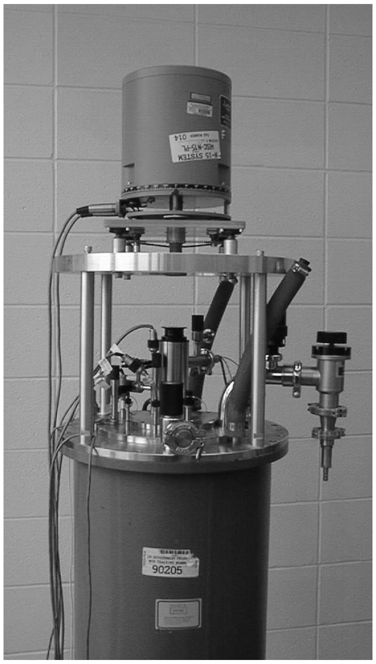

Fig. 3.4. 9 T VSM, head, mounting, and dewar.

Dimension of pick-up coil	
Number of turn for upper/bottom coil	3000
Diameter of copper wire for coils	0.08mm
Inner diameter of the coils	1.729″
Inner diameter of coil former	1.529″
Outer diameter of coil former	1.929″

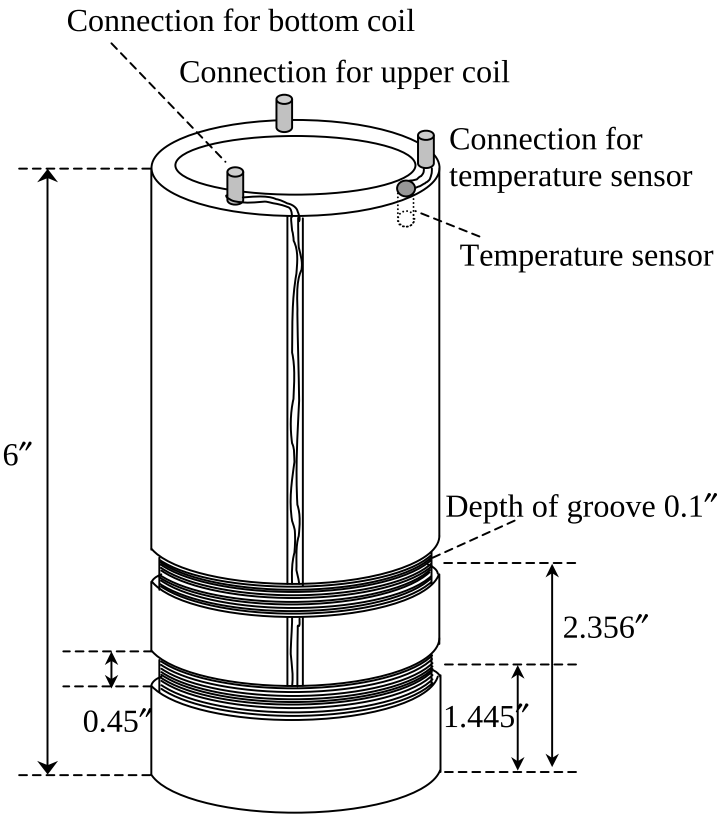

Fig. 3.5. Pick-up coil for the 9 T VSM.

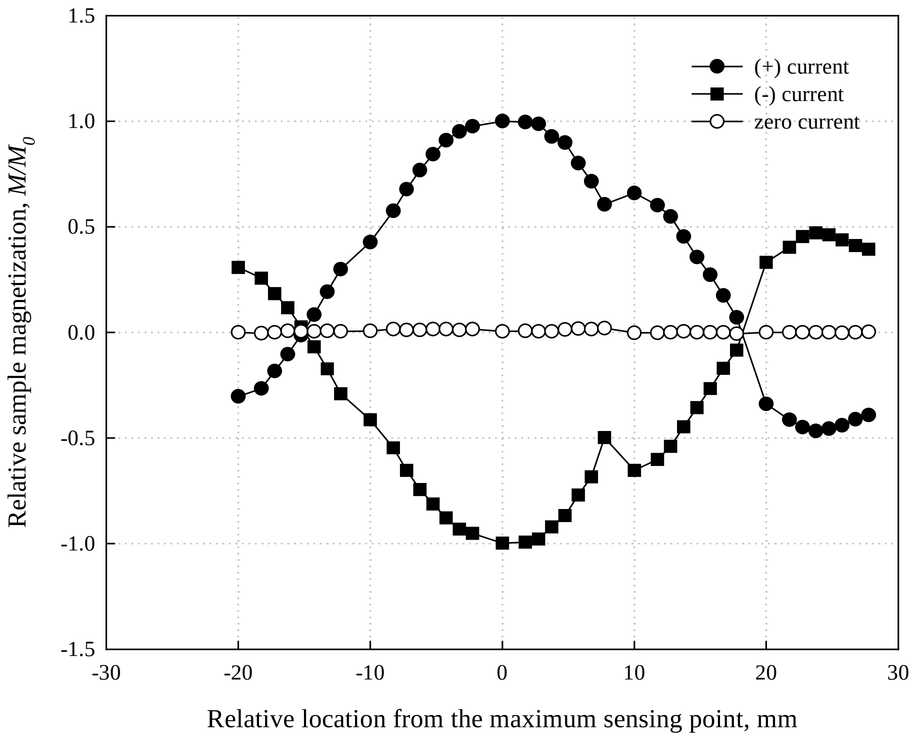

Fig. 3.6. Location of the maximum sensing point of the sample coil.

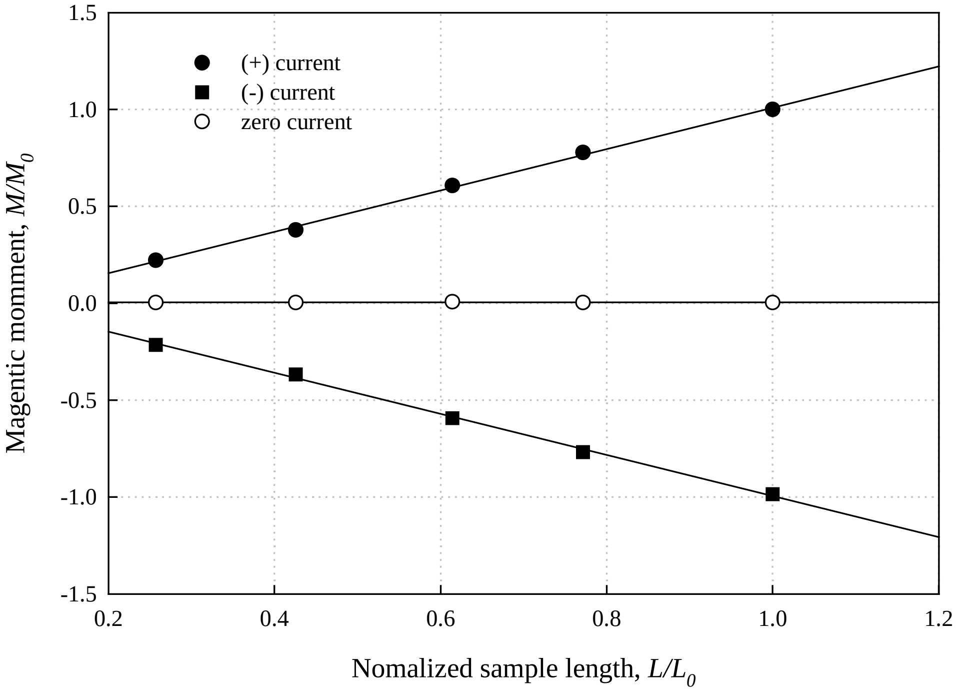

Fig. 3.7. Length dependence of magnetic moment of sample coil.

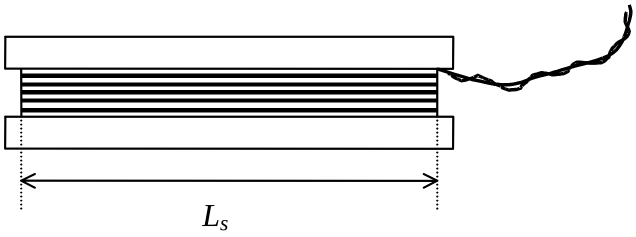

Fig. 3.8. Schematic of sample coil. Only the sample length L_s is changed. The number of turns and the width of sample coil are constant for all sample coils.

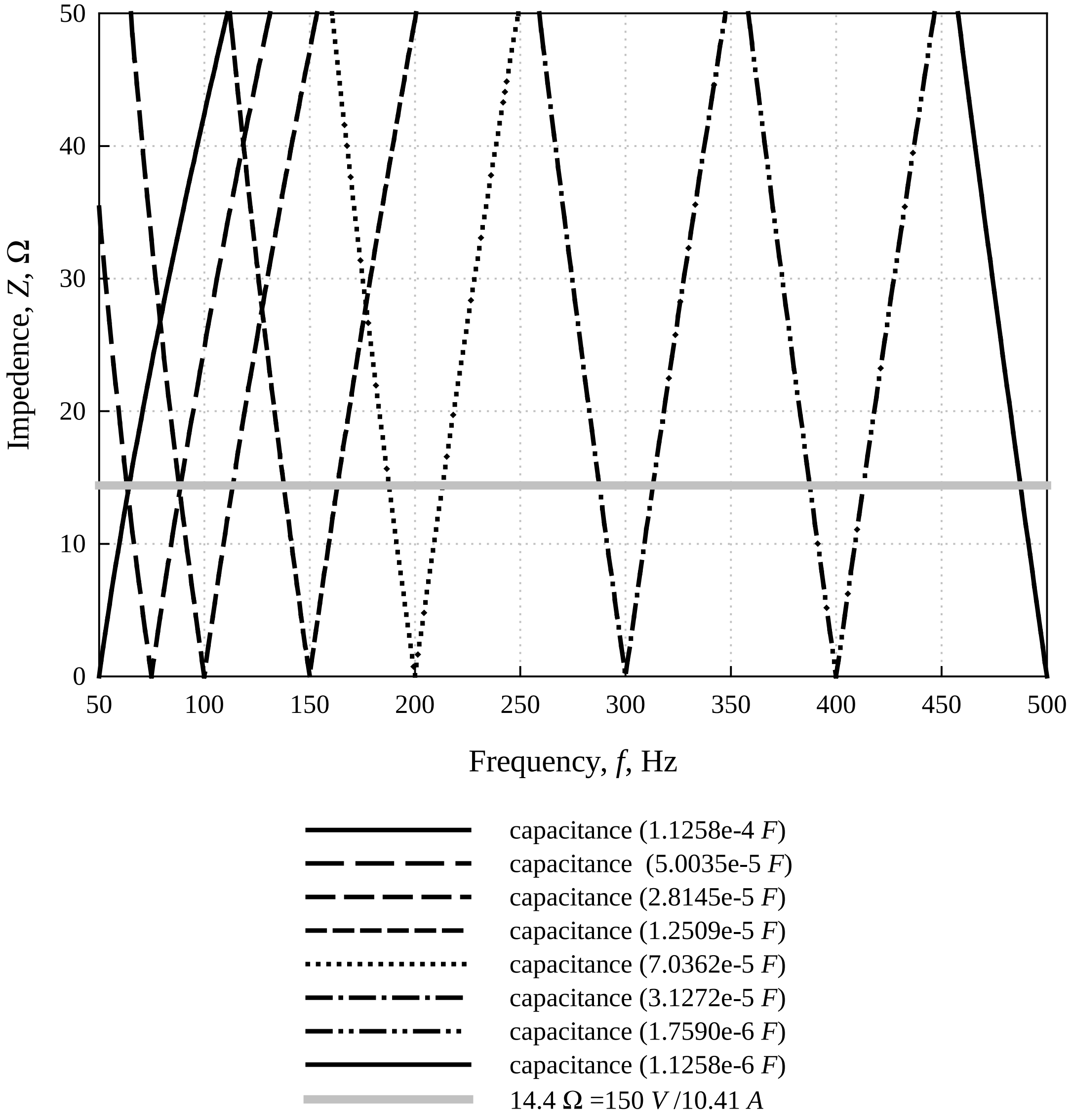

Fig. 3.9. Impedance at different frequencies using several values of capacitance.

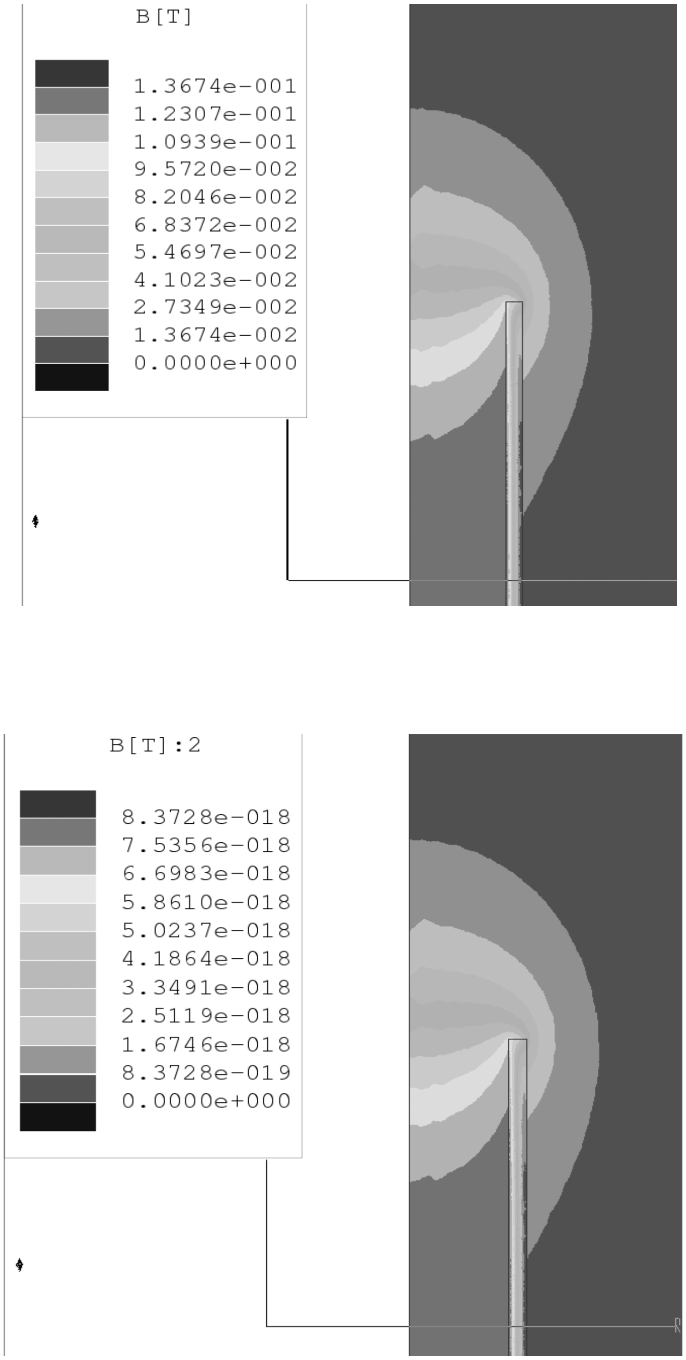

Fig. 3.10. Magnetic field distribution inside the external magnet when field is maximum and when the field is decreasing toward zero.

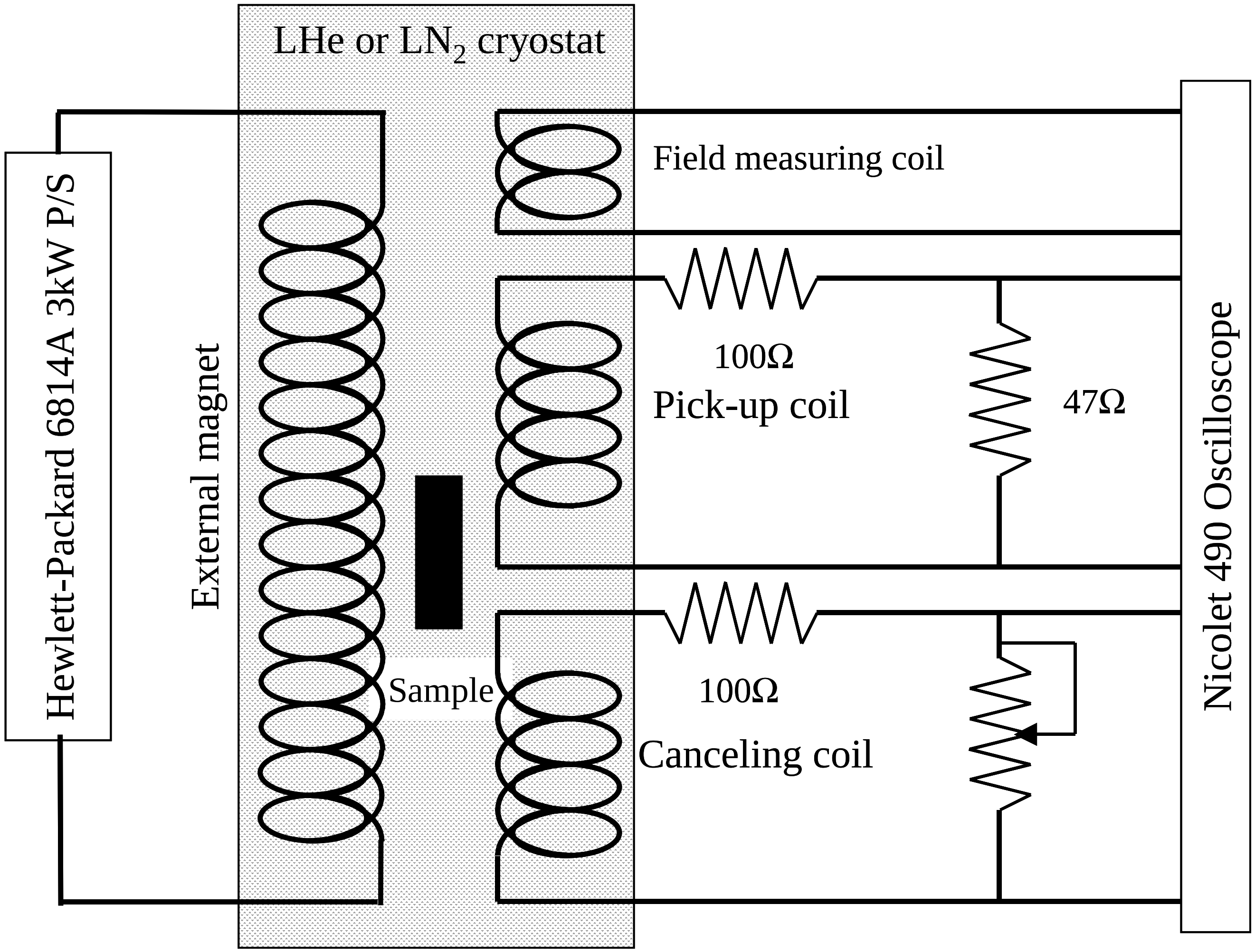

Fig. 3.11. Schematic of the pick-up coil

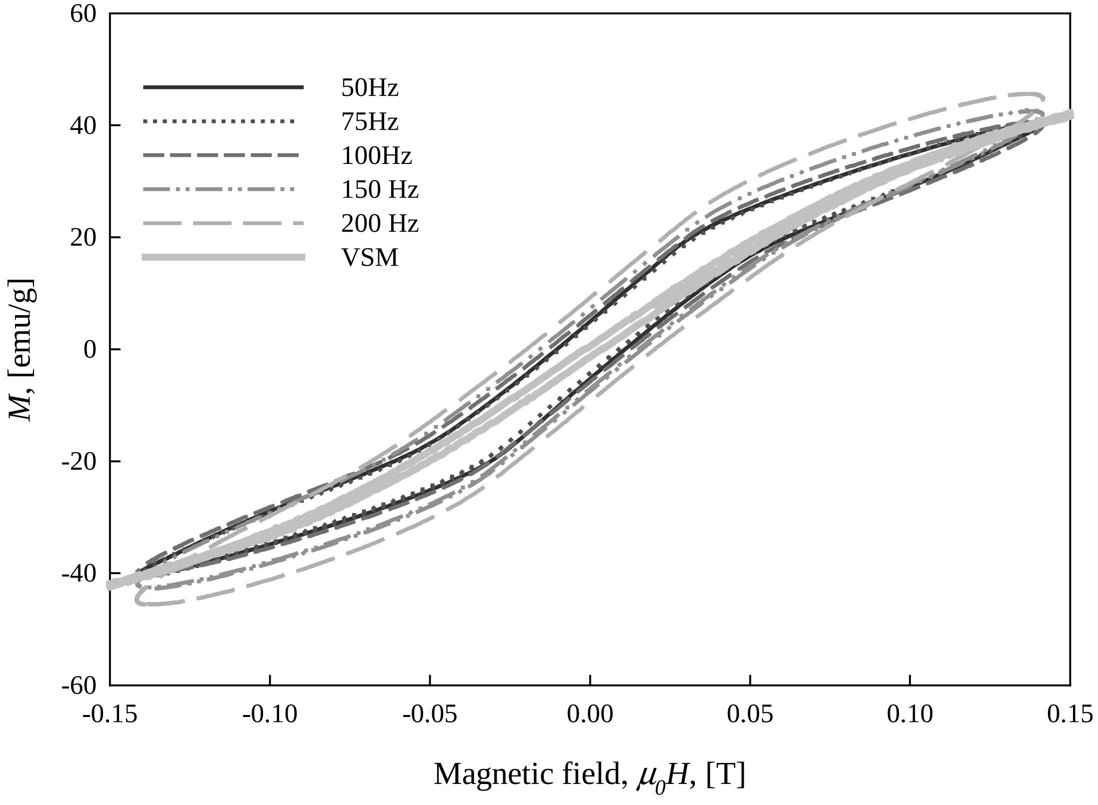

Fig. 3.12. Calibration of the pick-up coil method

Pick-up coil & cancel coil	
Shape	Square cylinder type
Dimension	$54 \times 30 \times 1.27$ mm
Number of turn	205
Number of layer	1
Wire diameter	100 μm
Inductance	≈ 0.980 mH
Magnetic field measuring coil	
Shape	Cylinder type
Diameter	16.0 mm
Height	30.0 mm
Number of turn	721
Number of layer	3
Wire diameter	100 μm
Inductance	3.660 mH
Magnet for external magnetic field	
Shape	Cylinder type
Inner diameter	88.9 mm
Outer diameter	11.07 mm
Clear bore	76.2 mm
Height	186.0 mm
Number of turn	1510
Wire diameter	1.0 mm
Inductance	90 mH
Resistance	9.9 Ω at 298 K

Table 3.3. Specification of various coils in the pick-up coil system.

REFERENCES FOR CHAPTER 3

[1] S. Soltanian, X. L. Wang, I. Kusevic, E. Babic, A. H. Li, M. J. Qin, J. Horvat, H. K. Liu, E. W. Collings, E. Lee, M. D. Sumption, and S. X. Dou, "High-transport critical current density above 30K in pure Fe-clad MgB_2 tape," *Physica C*, vol. 361, pp. 84-90, 2001.

[2] K. Kajikawa, "A new Multi-purpose Method for AC Loss measurements of superconducting wires" Thesis, Fukuoka: Kyushu University, 1998.

[3] K. Funaki, "Superconductivity, Part 8 AC loss measurements," International Electrotechnical Commission 90/FDIS, 1990.

CHCAPTER 4

RESULTS AND DISCUSSION

4.1 Numerical results

In order to describe the current distribution within superconducting composites and obtain the AC loss from it, the sample is divided into several blocks which have different conductivity tensors. Three dimensional block model is developed to describe the AC loss of various geometry conductors; specially rectangular and cylindrical shapes with and without resistive core. This model can be applied to both strands and cables. So far, an anisotropic continuum model has typically been used to describe the strands, and a discrete model has typically been used to describe the cables. However, we will compare these approaches for composites of both types.

A four-block model based on a numerical anisotropic continuum model (in this case a numerical approach) can be used to calculate the eddy current coupling loss of the composites with a complicate geometry which has not yet been solved with the usual analytic models above.

4.1.1 Rectangular geometry conductor without a core

First, the dependence of the eddy current couplings loss in a rectangular superconducting composites on the twist pitch, L_p, is presented for four-block modelwithout a core. It is proportional to the square of twist pitch, L_p, as should be expected from comparisons with analytic calculations based on continuum models [1, 2]. But, in the network model for a Rutherford cable, the dependence of eddy current coupling loss, P_e, on twist pitch, L_p initially appears to be just linear[3-5]. However, these two descriptions are really comparable. (For a further discussion of two points, see appendix A.) In the four-block model in this numerical calculation, the effective resistivity is defined in each of four blocks, as described in Table 2.2. We note that the eddy current loss is proportional to the square of the twist pitch, L_p as in Fig. 4.1. With increasing mesh, the data approach the theoretically expected line, but this asymptotic approach shows a saturation as the number of tetrahedron approaches 53,000.

Next, the aspect ratio (width/thickness) dependence of eddy current coupling loss of the composite is presented for a rectangular geometry without a core. Usually, the AC loss of HTSC (High temperature superconducting composites) has been modeled using ellipsoidal cross section geometries, and the aspect ratio of such a system is defined as (length of long axis, *a*/ length of short axis, *b*) of the ellipsoid. The eddy current coupling loss, P_e, depends on the square of the sample aspect ratio in case of twisted samples, but it shows just linear behavior in case of untwisted samples[6-9].

The geometry of various samples with different aspect ratios is shown in Fig. 4.2. The results from the four-block model (numerically calculated in this case) are shown in Fig. 4.3. We can see the square dependence of eddy current coupling loss, P_e, on the sample aspect ratio, (*a/b*). Results are normalized to the loss value of the widest width sample, w = 15 mm and the square of the twist pitch The reason for aspect ratio dependence of eddy current coupling loss, P_e, is presence of the demagnetizing field around the sample[10]. The demagnetizing field is again in this case present, due to the induced current within the sample. When induced current flows inside the sample, it induces the magnetizing field around the sample that modifies the applied magnetic field around the sample[11].

4.1.2 Rectangular geometry conductor with a core

To reduce loss, a core region between the upper layer and lower layer can be inserted as shown in Fig. 2.1. If we change the thickness and the conductivity of the core region, we can calculate the eddy current coupling loss for rectangular geometry conductors with resistive cores[12]. The current distribution in a sample without or with core is shown in Fig. 4.4. As core resistivity increases, the transverse current across the core is greatly reduced resulting in a reduction of eddy current coupling loss. We can change the core thickness as well as its resistivity. The geometry of various core models are shown in Fig. 4.5. In Fig. 4.6, the thickness of the core is varied from 0.4 mm to 1.5 mm and the conductivity is two orders of magnitude reduced as compared to the z-axis conductivity of the rest of the conductor in order to mimic the effect of a resistive core for a Rutherford cable[13, 14] or for a Bi based strand[15-18]. The values listed alongside the thicknesses are the loss values for twist pitch, L_p = 51.96 mm. As the core thickness increases and the conductivity decreases (Fig. 4.6. (b)), the eddy current coupling loss P_e decreases.

Loss calculations were made as the width of the core resistivity ($\sigma = 10^4$ S/m) was varied from zero to 12.5 mm, and the geometry of various core width models are shown in Fig. 4.7 and the results of these are displayed in Fig. 4.8. Q_e decreases as the resistive core width increases. Using the following expression from Carr[7],

$$\frac{P_e}{V_s} \approx \frac{\dot{B}^2}{120} {L_p}^2 \sigma_\perp \left(\frac{a}{b}\right)^2 \approx \frac{(2\pi f)^2 {B_0}^2}{2 \cdot 120} {L_p}^2 \sigma_\perp \left(\frac{a}{b}\right)^2 \tag{4-1}$$

and the calculated value of P_e, for f = 1 Hz, B_0 = 1.7 T, L_p = 30 mm, and $V_s = 1.8 \text{ x } 10^{-5} \text{m}^3$, we can obtain the effective transverse conductivity, $\sigma_\perp$. These results are shown in Fig. 4.9. As the thickness of the core is varied while keeping $\rho_c t_c = 10^{-7}\ \Omega\text{m}^2$ constant, the AC loss occurring in the core is as shown in Fig. 4.10, where we see the loss is lower for thicker cores (the core-only loss is of course the same by definition).

Loss calculations were then made as the conductivity of core and the conductivity in *z*-direction of four-block model was varied from 10^2 S/m to 10^6 S/m. The AC loss with respect to this conductivity variation is shown in Fig. 4.11. In the case of the four-block model, the loss is linearly dependent on the *z*-direction conductivity. But, in the case of the core model, the loss deviates from this linear behavior when the conductivity of core is less than 10^4 S/m and more than 3×10^5 S/m. At very low core conductivities, current path redistribution seems to be occurring, but since only $R_\perp$ associated losses were calculated, the reported values are underestimated of the loss for the core model in this region. On the other hand at high conductivities, the core conductivity is approaching that of the surrounding regions, a violation of the core model.

An outer sheath with thickness 1 mm and an isotropic conductivity of 10^6 S/m was added to one of the core models. The loss in the outer sheath was calculated in the *x*, *y* and *z* directions, while the loss inside the core was calculated using *z* direction current only, as before. The effect of outer sheath on loss is less than 10%. The geometry and the resulting losses are shown in Fig. 4.12.

To compare the numerical results above to those of experiments, the loss value should be multiplied by a conversion factor, *G*. Let $Q_{experiment} = G \cdot Q_e = G \cdot \frac{P_e}{f}$ where P_e in this work has been loss in W/m^3, Q_e is loss per cycle, and *G* is a conversion factor scaling the loss from values at parameter chosen for convenience in numerical calculations to those relevant to experimental situations. In particular, the conductivity of copper at 4.2 K is 6.45×10^9 S/m (based on a RRR = 100 and a copper resistivity at 273 K of 1.55×10^{-8} Ωm[19]). L_p is 115 mm, *t* is 1.9 mm and the magnetic field sweep amplitude is 0.4 T from[14]. In this calculation, transverse conductivity is 10^6 S/m, L_p is chosen as 51.96 mm, *t* is 4 mm, frequency is 1 Hz, and the magnetic field sweep amplitude is 1.7 T. The low conductivity value is chosen since the maximum available conductivity value which gives a sound current distribution is 10^{12} S/m. *Q* is calculated using

$$G \cdot \sigma L_p{}^2 (\tfrac{w}{t})^2 f B_0 = (\frac{6.45\times10^9 S/m}{10^6 S/m})(\frac{115mm}{51.96mm})^2 (\frac{1}{1.9mm/4mm})^2 (\frac{0.005Hz}{1Hz})(\frac{0.4T}{1.7T}) Q_e = 164 Q_e$$

with this conversion factor, *G*, the sinusoidal average loss value coming from calculation is 3.28×10^6 J/m^3 at 0.005 Hz. Experimentally, loss values for Cu-surface contact cables varies greatly[14]. The value of these calculation are similar to the highest loss measurements from experiments, namely, uncored LHC (Large hadron collider)-class cables cured for 2 hours at 250 °C from[20], which is 2.925×10^6 J/m^3. The difference between these values is 10.8%. This loss agreement of experiment with the highest loss experimental results makes sense because in our FEM calculation there are no thin oxide layers which would make the contact resistance high. Copper oxide layer on the strands of Rutherford cables is unstable and it dissolved completely in the above uncored LHC-class cables given aggressive heat treatments above 250 °C, 75 Mpa[21, 22].

4.1.3 Cylindrical geometry conductor

We can define a conductivity tensor in each block of a cylindrical model to simulate the eddy current coupling loss of a twisted round strand, or a twisted cable. The conductivity tensor is different point by point and is defined by two twist angles of the principle axis. One is γ for the twist angle of principle axis of σ_{zz} relative to the z-axis and the other is α for the twist angle of the principle axis of σ_{xx} relative to the x-axis. The details of the definition of the conductivity tensor are given in Fig. 4.13. The value of σ_{zz} is 10^{12} S/m and the values of σ_{xx} and σ_{yy} are 10^6 S/m. The current distribution of this model is shown in Fig. 4.14 and the results of P_e calculation are shown in Fig. 4.15. When P_e was calculated, only current components in x and y direction were considered to cause eddy current coupling loss. All data were normalized to P_e at L_p = 27.713 mm. Fig. 4.15 shows a square dependence of P_e on the twist pitch L_p, which is expected from anisotropic continuum theory. For comparison, P_e at L_p = 27.713 mm is 1283.2 Watts/m^3 and P_e from the analytical expression by Carr[1] is 1109.8 Watts/m^3 as given by,

$$\frac{P_e}{V_s} = (2\pi f)^2 \frac{\sigma_\perp (\mu_0 H_0)^2}{2} \frac{{L_p}^2}{4\pi^2} = 1109.8 \text{ Watts/m}^3$$

The difference between these values from four-block model and above expression is about 13.5%.

We can also insert a core region into this cylindrical four-block model with a core region conductivity of 10^6 S/m. We can then change the radius of core region and calculate the loss in the core region only. The results of this as well as a comparison to the cylindrical four-block model and the analytical expression of the above are shown in Fig. 4.16 for the case of L_p = 16.0 mm. The extrapolation of P_e of core model to a value at the core radius of 4 mm which is the radius of four-block model has the value of 319.66 Watts/m^3 and the P_e value from the cylindrical four-block model is 353.16 Watts/m^3 with the value from the analytical expression above is 369.92 Watts/m^3.

4.1.4 Seven-strand model

As an alternative to the cylindrical four-block model, a seven-strand model can be used to simulate the eddy current coupling loss in seven strand MgB_2 cables. We have to divide our model to represent each region with different conductivity as shown in Fig. 4.17. The superconducting core region has a conductivity of 10^{12} S/m and the matrix region has a conductivity of 10^6 S/m. In these regions, σ is isotropic. The interstrand region has a transverse conductivity 10^4 S/m and the inner strand region has a transverse conductivity 10^6 S/m. As these regions are anisotropic, we need to define the conductivity tensor as in 4.1.3 section. When the magnetic field is applied perpendicular to the sample, the current distribution should be as shown in Fig. 4.18. The eddy current coupling loss is caused by the transverse current (thick black arrow) and not by the current along the superconducting filament inside each strand (gray arrow). The analytical calculation of the interstrand eddy current coupling loss in seven strand cable is given in Appendix B.

The current distribution of a seven-strand model is shown in Fig. 4.19. In Fig. 4.19, the current inside the dotted line is the transverse current for the eddy current coupling loss and the other currents are along the superconducting filaments, generating no eddy current coupling loss. We can see the transverse current only in the interstrand region (inside dotted line), since in the numerical results, the current along the superconducting filamentary direction are also shown and projected into x-y plane. The results of interstrand eddy current coupling loss P_e, are shown in Fig. 4.20. The value of P_e for seven strand cable with the transverse conductivity of 10^4 S/m in the interstrand region is 0.95 % of loss value of the cylindrical four-block model with same radius (4mm). We can see the eddy current coupling loss is greatly reduced. However, the twist pitch dependence of P_e also follows the square of L_p. Here, the transverse current in the interstrand and matrix region are considered and the current in the inner strand region and the superconducting filament region are excluded since we are calculating the eddy current coupling loss between strands in seven strand MgB_2 cables.

4.2 Experimental results

4.2.1 Magnetic shielding in MgB_2 strands

To get a high critical current density, J_c, a sintering process is needed for MgB_2 wires. Stable metal sheaths should be used that does not react with Mg up to 900 °C. So far, the best candidate for this is Fe[23]. Since Fe is a ferromagnetic material, it will be necessary to include its losses in our calculations for twisted strands. It will turn out that under certain circumstances, the Fe can also reduce the losses.

A round strand 1.5 cm long and with a 0.77 mm radius was measured in the 1.7 T VSM. It had an Fe outer sheath. The *M-H* loops for this sample are shown in Fig. 4.21. In this figure, "No Fe sheath" means that we have subtracted the *M-H* loop measured at 40K (above the critical temperature of MgB_2). If we compare this *M-H* loop of "Fe sheath" sample to the *M-H* loop of bulk MgB_2 (Fig. 4. 22), we can see that below 0.2 T, the *M-H* loop is suppressed, such that the curve had no area. Since an *M-H* loop with smaller area is obtained, the hysteresis loss of this strand is reduced. This effect is caused by the magnetic shielding of the Fe matrix as explained by " the Pseudo Meissner Effect "[24]. This magnetic shielding effect is shown at various temperatures in Fig. 4.23. The *M-H* loop size decreases, as the temperature is increased towards T_c. Above T_c, only the signal from Fe sheath can be seen.

M-H loops of MgB_2 strands with different heat treatments and powder compositions were measured at 4.2 K using the 9 T VSM. In Fig. 4.24, we can also see the magnetic shielding effect at low applied fields. Above 6 T, the magnetic J_c are zero as can be seen from the ΔM values of the *M-H* loops. Adding carbon and SiC to MgB_2 powder increases the magnetic J_c of the composites[25-27]. The saturation magnetization of each MgB_2 strand can be seen at high magnetic fields. It comes from the Fe sheath or the Fe and monel sheath and shows that the saturation is different for each samples because the effective thickness of the ferromagnetic layer is different. Not only the saturation magnetization, but the magnetic shielding effect also depends on the thickness of Fe layer. The magnetic shielding effect is more severe for the samples from the

University of Wollongong than those from Hyper Tech Research, as shown in Fig 4.21 and Fig. 4.23. Hysteresis loss is reduced by the magnetic shielding of the Fe, but its effects on the eddy current loss still need to be investigated (but see below).

It is important to be careful when determining how much the hysteresis loss is reduced by this magnetic shielding, since there are two kinds of magnetic shielding induced by the Fe sheath. One is the magnetic shielding of the applied magnetic field to the superconducting filaments (Outside to Inside shielding), another is the magnetic shielding of the magnetic moment of superconducting filaments from the pick-up coil (Inside to Outside shielding)[28, 29]. The “apparent loss” with these two forms of magnetic shielding is always less than the “real loss” which the composite really exhibits.

Numerical calculation using FEM (Finite Element Method) was performed to differentiate these two kinds of magnetic shielding. Using FEMLAB FEM code, a two dimensional simulation was performed. To calculate a Bean-current like magnetization, we first define a positive critical current density in one half of the superconducting region and a negative critical current density in the other half of the superconducting region. The polarity of this current is reversed when shielding branch of *M-H* loop changes to a trapping branch and vice versa. The magnitude of the critical current density in this region can be assumed to follow the Kim-like model, decreasing with the magnetic field. The intrinsic magnetic permeability of the Fe matrix should be used when there is magnetic shielding and the magnetic permeability of Fe should be set to unity when there is no magnetic shielding effect.

If we apply a magnetic field, H_0, we can get the B from the numerical results in each geometry, and from $B = \mu_0(H_0 + (1-D)M)$, we can calculate the magnetization M

in each geometry. *D* is demagnetizing factor for this two dimensional geometry and can be calculated using permeability values[28, 29]. We must use only the *B* component along the applied field direction.

When we calculate the “real loss” that is the loss without the inside to outside shielding, first, the applied magnetic field, H^* of superconducting region need to be calculated for the outside to inside shielding. This can be calculated putting the intrinsic permeability of Fe into sheath region. Once the magnetic field, H^* is calculated, we change the permeability of Fe to a unity to remove the inside to outside shielding. By applying the same magnitude of the magnetic field as H^*, we can obtain *B* in the superconducting area without the inside to outside shielding. Then, we calculate *M* from *B* and H^* with demagnetizing factor. This M should be normalized to whole composite volume.

In Fig. 4.25, the *M-H* loops for the “real loss”, the “apparent loss” and the loss without any magnetic shielding are shown. If we calculate the loss values with respect to the applied magnetic field by calculating area of the *M-H* loops, the “real loss” is always greater than the “apparent loss” but is always smaller than the loss without any magnetic shielding (Fig. 4.26).

4.2.2 AC loss measurement by pick-up coil method

AC losses of seven-strand MgB_2 cables are measured at 4.2 K by the pick-up coil method as discussed in Chapter 3. The external magnet and the measuring coil system containing a sample are located inside the liquid He dewar for 4.2 K measurement. The results are displayed in Fig. 4. 27-29. There are almost no hysteresis loss and no eddy current coupling loss for these seven strand MgB_2 cables in this low magnetic field even though the applied frequency is above 50 Hz. We expected low losses, based on the values predicted by contact resistance measurements. However, this loss is even smaller than we expected.

The reason for low hysteresis loss is the magnetic shielding effect by Fe layer surrounding superconducting MgB_2 filaments. To get some hysteretic signal from superconducting filament, the applied magnetic field to MgB_2 strand should be larger than 0.2 T. But, at present, the output of AC power supply is limited to 0.14 T and even this maximum magnetic field cannot be applied and only 0.04 T is available due to the severe evaporation of liquid He.

One of the reasons for this extremely low loss besides the magnetic shielding effect and high contact resistance can be the applied magnetic field is below the penetration field of the composite. The penetration field is given by $H_p = (2/\pi)\, r_0 J_c$. If we input, r_0 = 0.2 mm J_c = 100 A /(πr_0^2), then H_p is about 0.127 T which is well above the applied magnetic field, 0.04 T in this pick-up coil method. In this situation, the permeability of the composite is not unity and the composite is still diamagnetic material. Then, according to Campbell[10], the eddy current coupling loss is greatly reduced when the superconducting filaments is in diamagnetic state.

The low eddy current loss is mainly due to the very high contact resistance between the strands. From the expression (1-3) and (4-1), the eddy current coupling loss is inversely proportional to the effective resistivity of the superconducting composite. If we convert the contact resistance to effective resistivity using the expression in Appendix

B, the effective resistivity is about 10^4 times higher compared to that of Bi2223/Ag strand in 4.2 K even in the case of no insulated MgB_2 cables.

Another possible reason for almost zero AC loss is the current re-distribution when there is high permeability material as Fe. However, how different it is from the case where there is no Fe layer and whether this will reduce the eddy current coupling loss or not, are still need to be investigated in future study.

The low AC loss in this condition is valuable for the application such as power transfer line and transformer where the magnetic field is low but the frequency is high. However, the areas of *M-H* loops are too small to calculate the loss from it and compare to the results from the seven-strand model and the analytical model in Appendix B. Those models expect some eddy current loss anyway.

4.2.3 AC loss from measuring of contact resistance of MgB_2 seven strand cable

AC loss measurement at 4.2 K by the pick-up coil method is non-trivial. The measurement of eddy current coupling loss by VSM is also difficult because of the limited frequency range (typically lower than (1/120) Hz). Therefore, we need an alternative to estimate the eddy current coupling loss of superconducting composites in a simple way.

The eddy current coupling loss in cables is dominated by the contact resistance between the strands inside the cable[13, 14]. If, for example, the contact resistance between the upper layer and the lower layer of the Rutherford cables is known, the eddy current coupling loss of the cable can be determined by the network model[5]. Similar models are available for round CIC (Cable in conduit) cases, [30-33]. However, in seven strand MgB_2 cables, the sample geometry is different from the above examples.

Below we will measure the contact resistance of some seven strand MgB_2 cables. Experimentally, measured contact resistances results from many possible connection paths between strands. For example, the contact resistance between strand 1 and strand 2 comes from the contact of strand 1 and strand 2 and other contacts between strands. (See Appendix D). The contact resistance, R_c, between any pairs of strands can be determined after measuring experimentally four contact resistances, R_1 (between strands 1 and 2), R_2 (between strands 1 and 3), R_3 (between strand 1 and 4) and R_4 (between strand 1 and 5) as follows

$$R_c = \frac{273R_1}{60} = \frac{283R_2}{60} = \frac{258R_3}{60} = \frac{234R_4}{60} \qquad (4\text{-}2).$$

With R_c, after normalizing by multiplying the number of eddy current path ($L_s/2r$), the eddy current coupling loss in seven strand MgB_2 cables can be calculated as follows

$$\frac{P_e}{V_s} = \frac{9\pi r^3 \dot{B}^2 {L_p}^2}{48\rho_\perp} \times \frac{(L_p/2r)}{\pi(3r)^2 L_p} = \frac{\dot{B}^2 {L_p}^2}{96\rho_\perp} = \frac{\dot{B}^2 {L_p}^2}{32\pi r R_c} = \frac{\dot{B}^2 L_p}{16\pi R_c} \cdot N_e \quad (4\text{-}3).$$

r is the radius of one strand, L_s is the sample length, L_p is the twist pitch, N_e is the number of eddy current paths in the volume of one twist pitch. (refer to Appendices A and B)

Four contact resistances for each MgB_2 cable were measured as explained in Chapter 3. The results are shown in Fig. 4. 30. When there is an insulation layer between strands, the contact resistance is two orders higher than the contact resistance without an insulation layer. Motor oil, gear oil, and high temperature paint coatings were used as insulation methods for these cables. We can see that the high temperature painting used in PAT04 did not provide any insulation effect. The possible reason for this was that the paint did not adhere to the individual strand during twisting and heat treatment. Since the etching procedure before applying the paint removed the natural oxide on the surface, the contact resistance is even lower than that of no insulation at all.

The effect of twist pitch on the contact resistance is shown in Fig. 4.31. There is almost no dependence of the twist pitch on the contact resistance.

4.2.4 Microscopic analysis of contact region

Optical microscopy of one of the MgB_2 cables (MOT01) is shown in Fig. 4.32. The uncontacted region as indicated in the Fig. 4.32 can cause some distribution of the contact resistance values. After 5 second etching with dilute hydrochloric acid, we can identify the Fe layer surrounding the MgB_2 superconducting filaments.

The average contact resistance between strands over the cable length, which is an important factor to the eddy current coupling loss, is a kind of summation of the local contact resistance between the strands. In section 4.2.3, the average contact resistance over the cable length not the local contact resistance at some point was measured. This local contact resistance can be affected by several factors. There can be the uncontacted regions as above, the carbonizing effect of decomposed SAE30 oil, and the existence of a native oxide layer on the metal sheath. At 750 °C, carbon can be dissolved into Ni about 0.4 At. % and 0.008 At. % into Cu[34]. There is no ternary phase diagram for Ni-Cu-C system. The oxide layer on the surface of the strands can be affected by the insulating methods and can be the natural oxide itself on the metal surface in case of the sample without any surface treatment. The sample insulated with SAE30 oil (MOT01) and the sample without any surface treatment (NOS03) was analyzed with SEM and EDS. The interface between strands of NOS03 is relatively clear compared to that of MOT01 as shown Fig. 4.33. This may be due to the decomposition of the SAE30 oil applied to the strand surface after heat treatment.

To see if there is any carbonizing effect from SAE30 oil to the strand matrix which is nickel alloy, EDS analysis was performed on the both sample. The composition of carbon is not so much different on both samples though the content of carbon in MOT01 is slightly higher than that of NOS03. But, the contamination of carbon can occur easily in standard SEM sample preparation and the carbon content is decreasing toward the interface from the superconducting filament except near the interface where the carbon content is very high for both samples. Therefore, the carbonizing effect by SAE30 oil addition is not clear by EDS analysis, though the averaged contact resistance of MOT01 is about 20 times higher than that of NOS03.

To check any oxide layer on the surface of strands, we found the clean surface without contamination of impurity such as Si, S, C from mounting epoxy and diamond paste as shown Fig. 4.34. Two points in each sample are analyzed by EDS. One is for the free surface and another is for the inside of matrix. The composition of oxygen is slightly higher in case of MOT01. But, the effect of applying SAE30 oil on the natural oxide is not so clear from this composition difference.

The primary object of the Fe layer surrounding superconducting filaments is preventing a reaction between Mg in superconducting filament and Cu in matrix materials. If there is no Fe layer, the reaction between Mg, Cu and Ni occurs, forming intermetallic compounds, such as Cu_2Mg and $CuMg_2$. Reaction between Mg and Ni also occurs, froming Mg_2Ni and $MgNi_2$[35]. BSE image and EDS analysis of NOF11 without Fe layer between filament and matrix shown in Fig. 4.35 indicate the existence these reactions and we can clearly see the reaction layer between filament and matrix. EDS analysis was performed at nine locations by point by point. Three points (# 1-3) are within an MgB_2 filamentary region, next three points belong to reaction layer, and remaining three points are within monel matrix. Secondary electrons were gathered at 20 kV during the lapsed time 40 sec at average (at least 1000 count number), until pick heights of each elements signal did not change to insure enough and same condition for each analysis.

Even the reaction between Fe and Ni seems to occur at 750 °C and the reaction layer can be seen as shown in Fig. 4.36. EDS analysis was performed by point by point as same way as NOF11 sample. #1 point is within an MgB_2 filament, #2 and #3 points are within Fe layer, # 5-7 points are within matrix. #4 point belongs to "reaction layer" in case of PAT04 sample, but there is not the reaction layer in case of CUC14 sample (no #4 point for CUC 14 sample). EDS analysis shows that Fe composition does not fall to the level same as that of matrix. The reaction layer can be seen in PAT04 with monel matrix, but it is difficult to find in CUC14 with Cu-Ni alloy with high Cu composition about 85 At. % Cu. This is expected from binary phase diagram of Ni-Fe and Cu-Fe[35]. The solubility of Cu in Fe, vice versa, is about 1 At. % at 750 °C, but in case of Ni-Fe system, the solubility of Ni to Fe is about 4 At. % and $FeNi_3$ intermetallic compound and (γFe, Ni) alloy can be formed in wide composition range.

The reaction between elements from filaments and elements from matrix does not change the contact resistance between strands directly. But, it changes the overall transverse effective resistivity of superconducting composites, that is $R_{c\ effective} \approx R_{c\ strand} + R_{c\ reaction\ layer}$. This increased effective resistance eventually reduces the eddy current coupling loss. However, the superconducting properties of filaments such as T_c and J_c must be considered more fundamentally than the reduction of eddy current coupling loss of the composites.

4.2.5 Comparison of AC loss calculation and AC loss measurement

From the measured contact resistance values, we can get the value of R_c from expression (4-2). Using this R_c value and expression (4-3), we also can get the AC loss (eddy current coupling loss) of seven strand MgB_2 cables. For example, the measured contact resistance R_c of an MgB_2 cable(MOT01) insulated with SAE30 oil is 0.439 Ω. The R_c of eddy current path then, is $0.439 \times (L_s/2r) = 45.88$ Ω. Here, L_s is sample length, and r is radius of a strand. Using (4-3), the eddy current coupling loss at a frequency of 1 Hz and a magnetic field of 1.7 T is 4.44×10^{-2} Watts/m^3. The calculated AC loss value from numerical simulation is 5.42 Watts/ m^3. This loss value is calculated inside the interstrand region only using the current along the x-direction that is the transverse direction in the seven strand cable geometry. We also considered the current along the z-direction only the transverse direction in the in four-block model and core model for the Rutherford cables.

To compare these loss values, we have to use a conversion factor G. Here, the frequency and the magnetic field are assumed the same as 1 Hz and 1.7 T for both cases and G is defined as follows.

$$P_{e\ from\ Rc} = G \cdot P_{e\ from\ Numerical} = ((\frac{L_{p\,Rc}}{L_{p\,Num}})^2 / (\frac{\rho_{\ Rc}}{\rho_{\ Num}})) \cdot P_{e\ from\ Numerical} = 9.35 \times 10^{-3} \cdot P_{e\ from\ Numerical}$$

$L_{p\ Rc}$ is 0.044 m, $L_{p\ Num}$ is 0.028 m $\rho_{\ Rc}$ is 2.642×10^{-2} Ω m and $\rho_{\ Num}$ is 1.0×10^{-4} Ω m. ρ_{Rc} is from R_c value using $\rho_\perp = \frac{\pi r}{3} R_c$. (Refer to Appendix A). Then, using this *G*, the AC loss from numerical calculation is converted to $5.42 \times 9.35 \times 10^{-3} = 5.07 \times 10^{-2}$ Watts/m^3. The difference between AC loss using measured R_c values and expression (4-3) and the AC loss from numerical calculation is about 12.5 %. This difference is due to the loss calculation using all the current inside the interstrand region including the current along the strands that has no resistive component in real application. In Fig. 4.17 and Fig. 4.19, we have to use the only the transverse current causing the eddy current loss not the current along superconducting filaments. In numerical calculation, by definition of anisotropic conductivity, the current that flows along the strands **inside the interstrand** region has resistive component resulting eddy current coupling loss.

The second example is for the MgB_2 cable with high temperature painting (PAT04). This cable has two orders lower value of measured R_c, which is 2.903×10^{-3} Ω, since there is no insulation layer. R_c of the eddy current path is 0.4592 Ω. Then, the AC loss using (4-3) is 4.44 Watts/m^3. This time *G* is 1.12 and the AC loss from numerical calculation is converted to $5.42 \times 1.12 = 6.07$ Watts/m^3. The difference between AC loss using measured R_c values and expression (4-3) and the AC loss from numerical calculation is about 27 %.

The eddy current coupling loss predicted by numerical calculation can be compared to the loss from expression (4-3) using the value of R_c in more wide range of frequencies. The applied magnetic field is assumed 0.14 T, and in each frequency, the conversion factor *G* was calculated. After multiplying this *G* to the numerical result, the comparison for the sample insulated with SAE30 oil (sample #1) is given in Fig. 4.38, and that of the sample painted with high temperature paint (sample #3) is given in Fig. 4.39. According to the anisotropic continuum theory [1], there is a frequency above which saturation occurs and the whole filamentary array is coupled together. To get a general frequency dependence of eddy current loss, the factor of $1\big/(1+(f\ /\ f_1)^2)$ should be multiplied to the loss in linear dependence region. Here, f_1 is the critical frequency the saturation occurs and $f_1 = \dfrac{4\pi}{\mu_0 \sigma_\perp {L_p}^2}$. Since the effective resistivities of both sample is high not to allow the saturation occur below 200 Hz, the general frequency dependence of eddy current loss is identical to the linear frequency dependence as in Fig. 4.37 and Fig. 4.38.

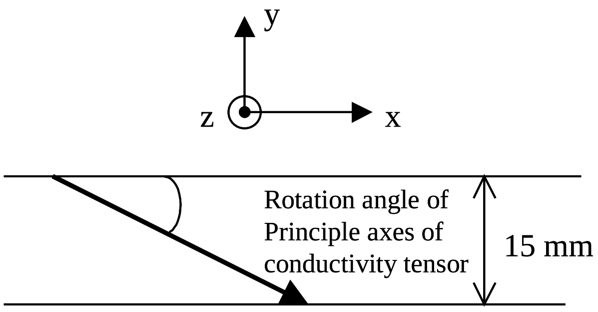

Top view of four block model

L_p, mm	Rotation angle, °
51.96	30
42.84	35
30.00	45
25.17	50
17.32	60

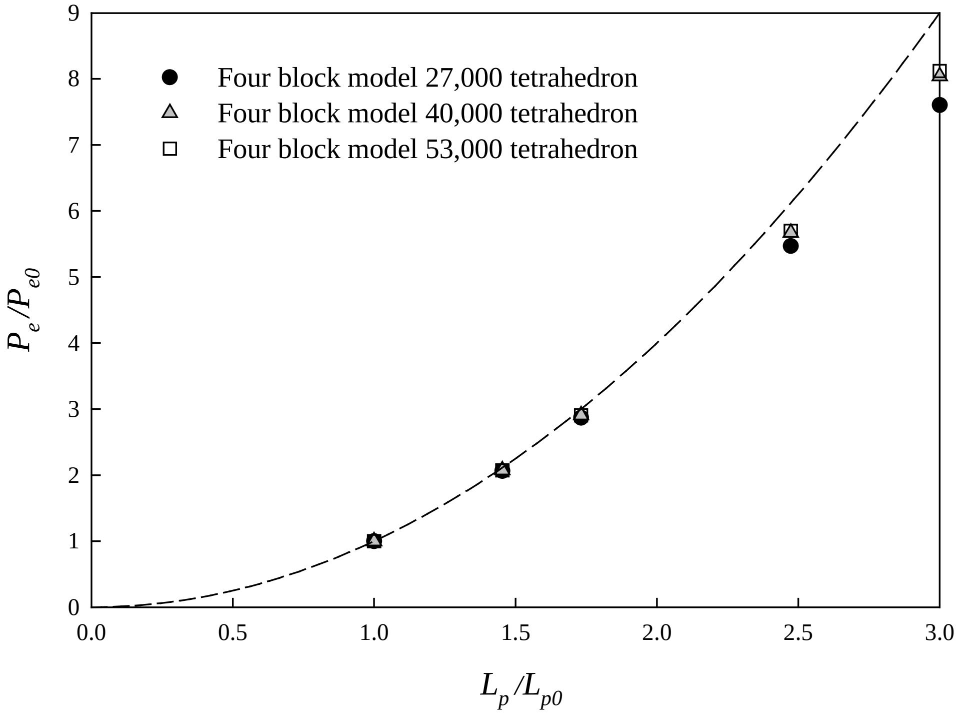

Fig. 4.1. Twist pitch dependence of the eddy current coupling loss in the four-block model.

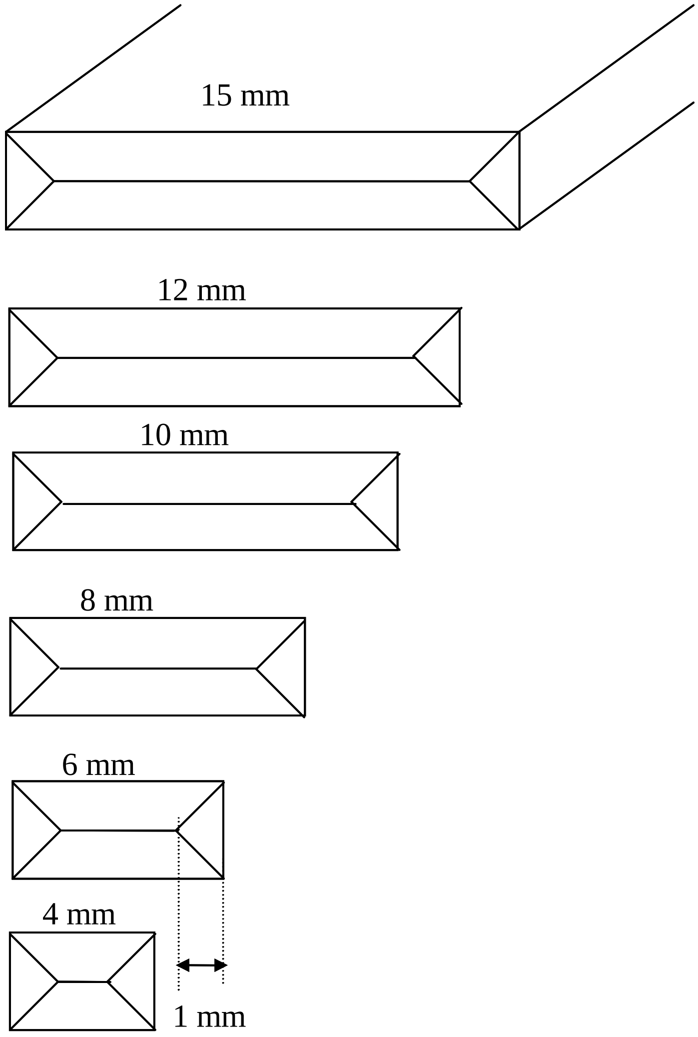

Aspect ratio	$(a/b)^2$
15/4 = 3.75	14.06
12/4 = 3.0	9.0
10/4 = 2.5	6.25
8/4 =2.0	4.0
6/4 = 1.5	2.25
4/4 =1.0	1.0

Fig. 4.2. Four-block models with various aspect ratios.

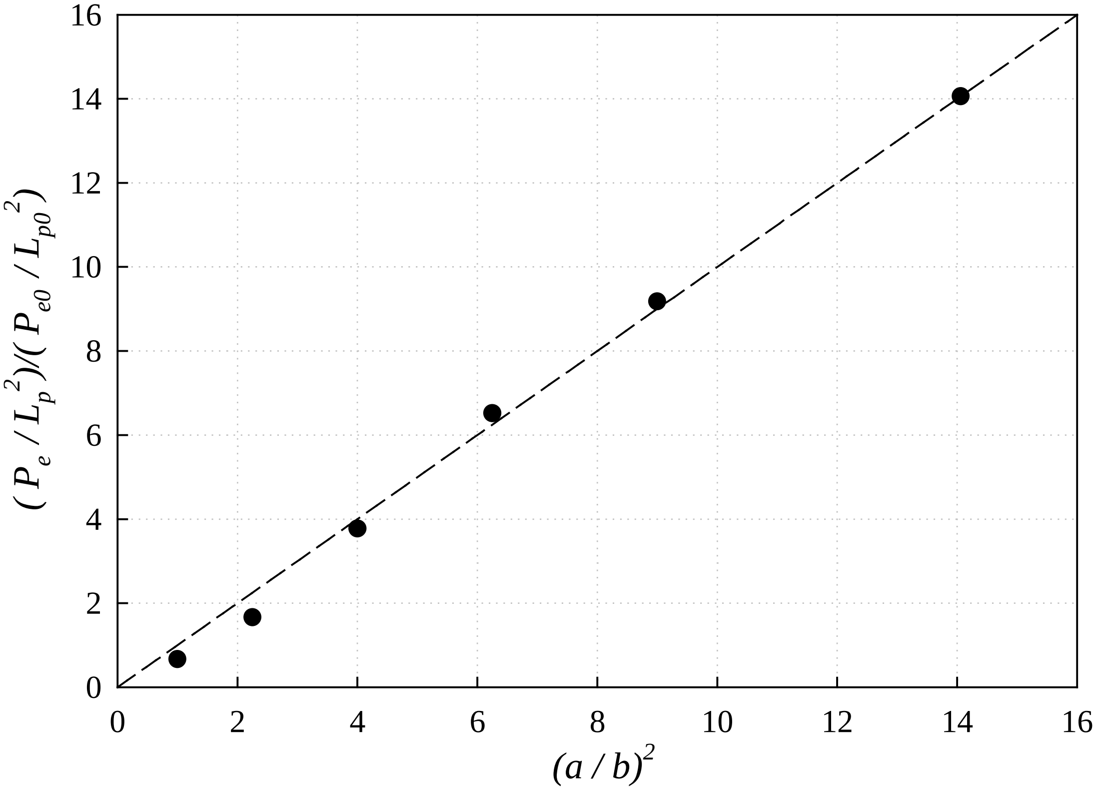

Fig. 4.3. Aspect ratio dependence of the eddy current coupling loss in four-block model. The loss is normalized to $(a/b)^2 = 14$.

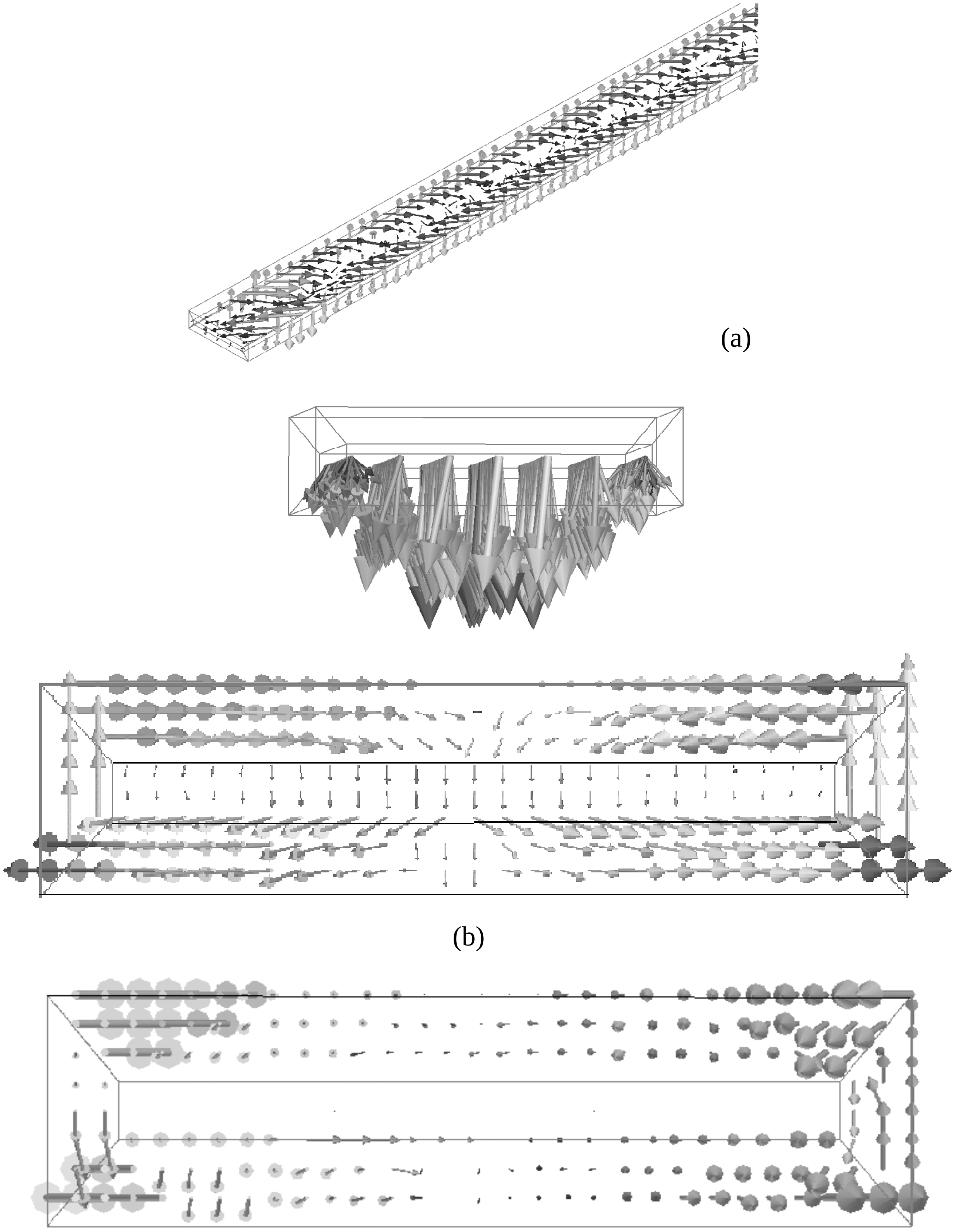
(a)

(b)

(c)

Fig. 4.4. Current distribution in block model with a resistive core. (a) shows three dimensional views of currents. Second view of (a) shows just a transverse current across the core. (b) core with conductivity 10^6 S/m (c) core with conductivity 10^4 S/m.

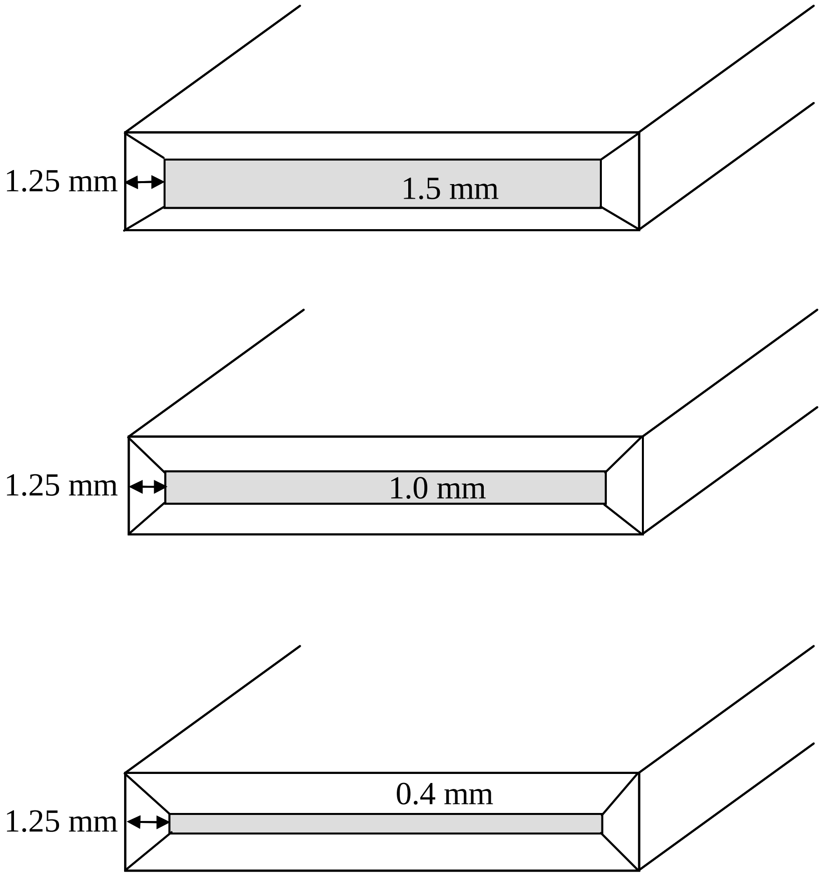

Fig. 4.5. Geometry of the block model with different core thickness.

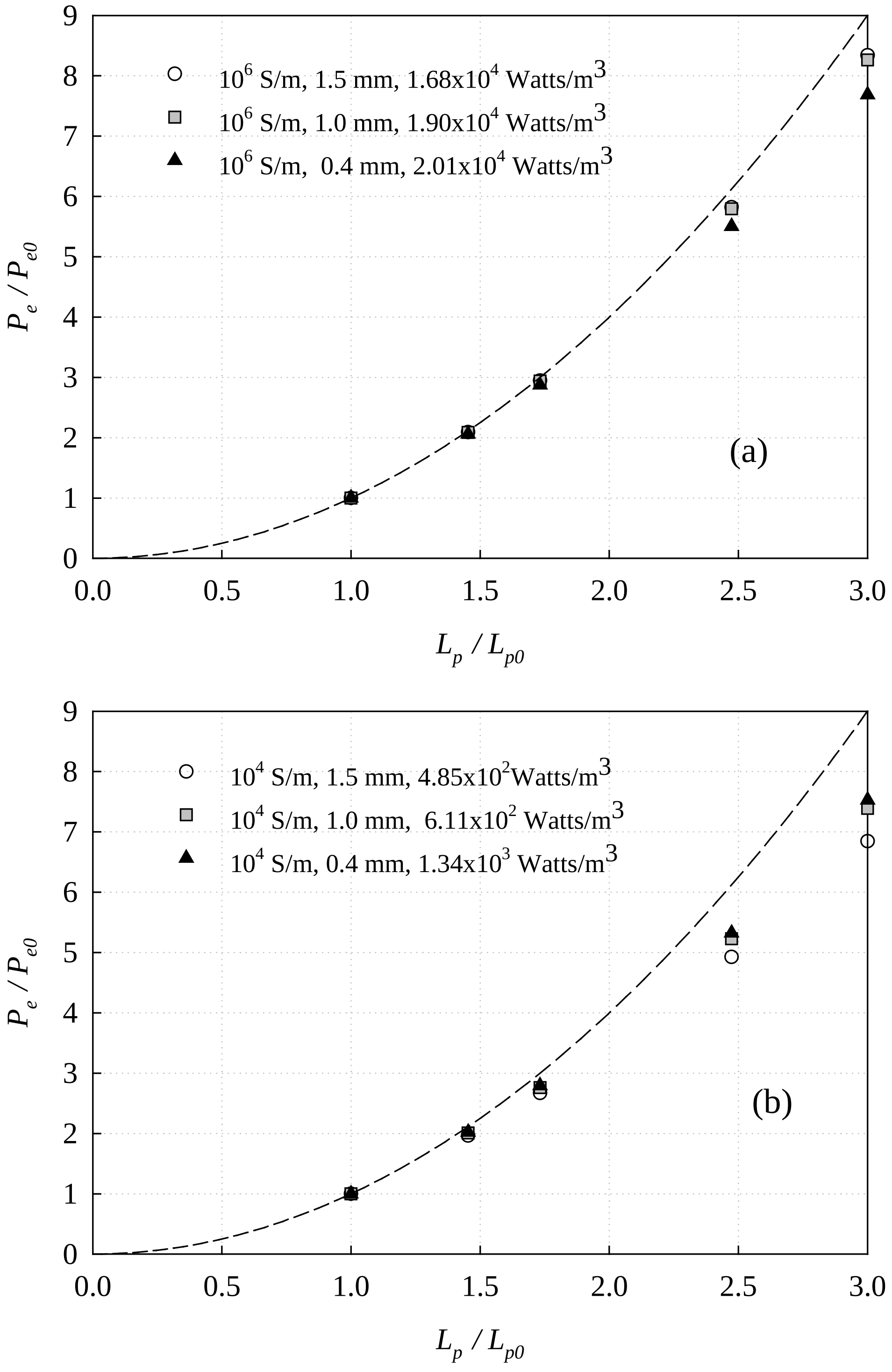

Fig. 4.6. Normalized loss vs L_p for (a) various core thickness, and (b) various core conductivities.

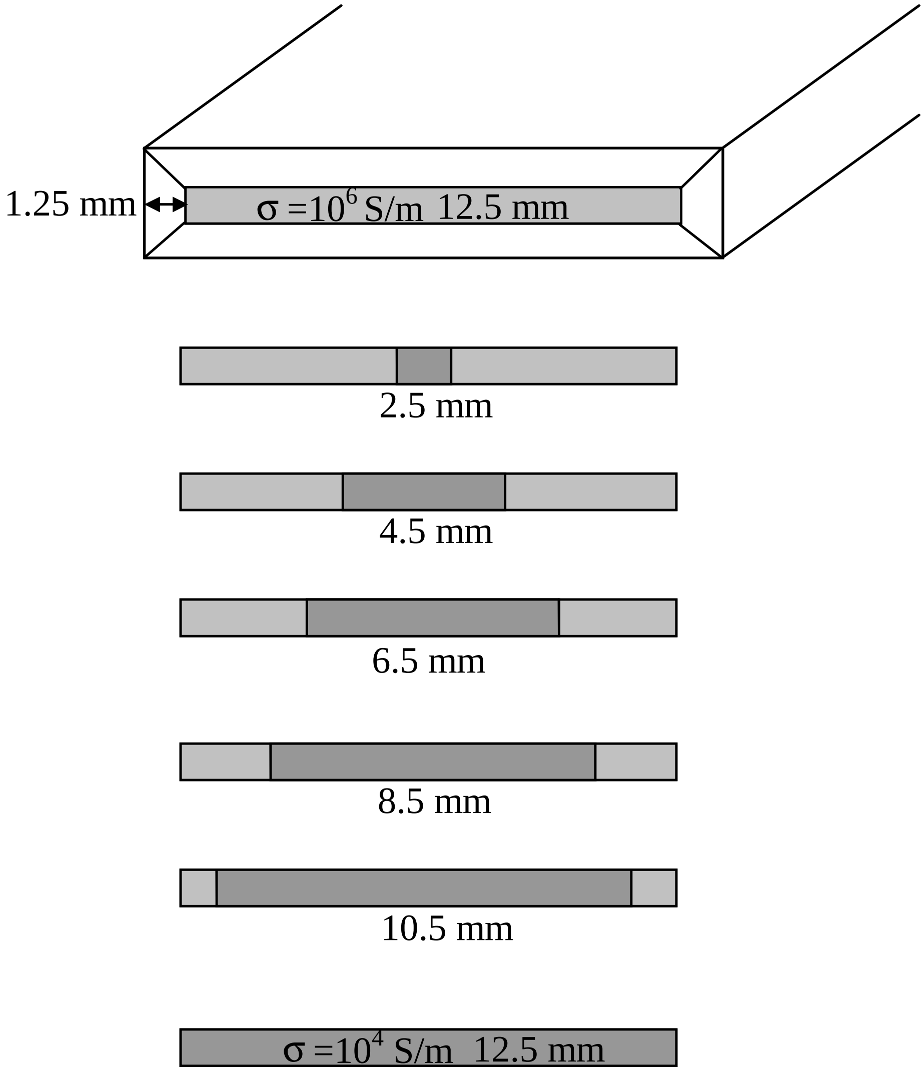

Fig. 4.7. Geometry of various core width-block models.

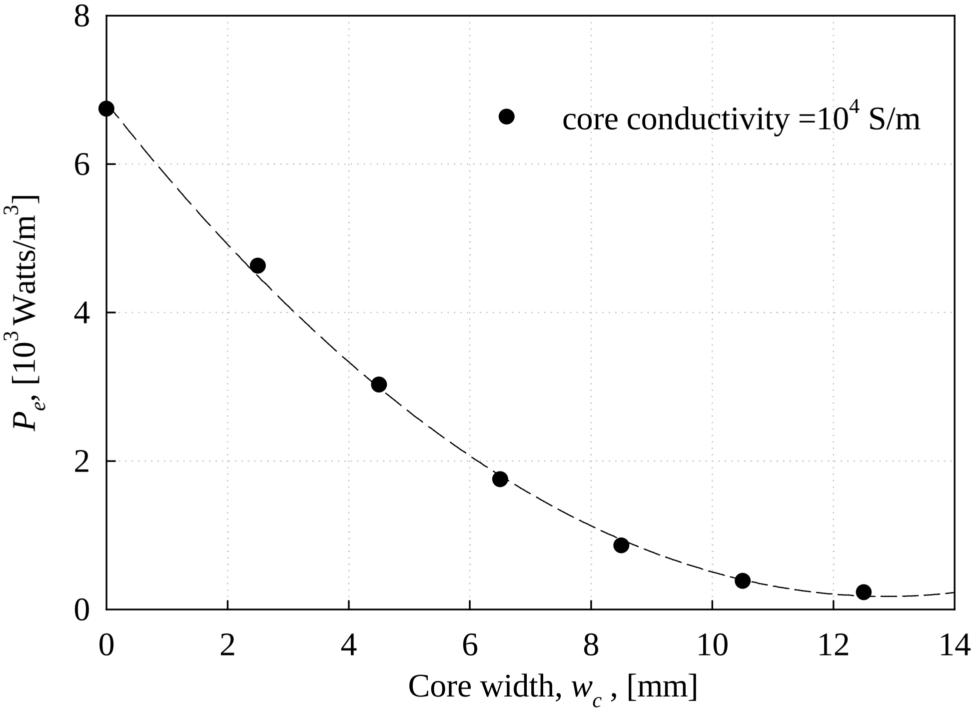

Fig. 4.8. Resistive core width dependence of P_e.

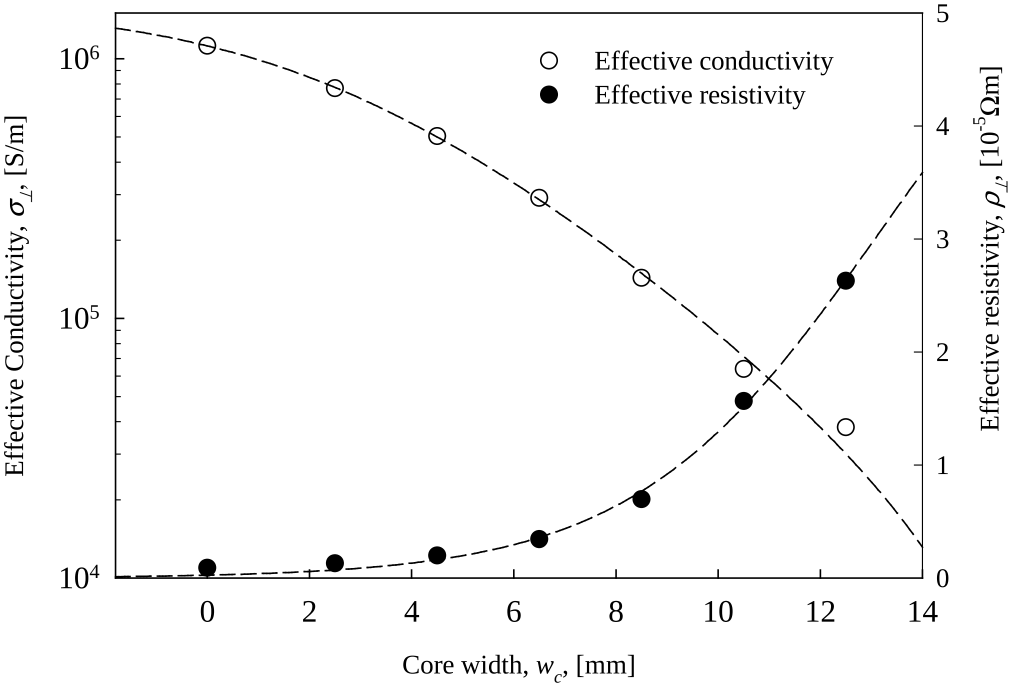

Fig. 4.9. Effective resistivity derived using analytic anisotropic continuum-based expression (4-1).

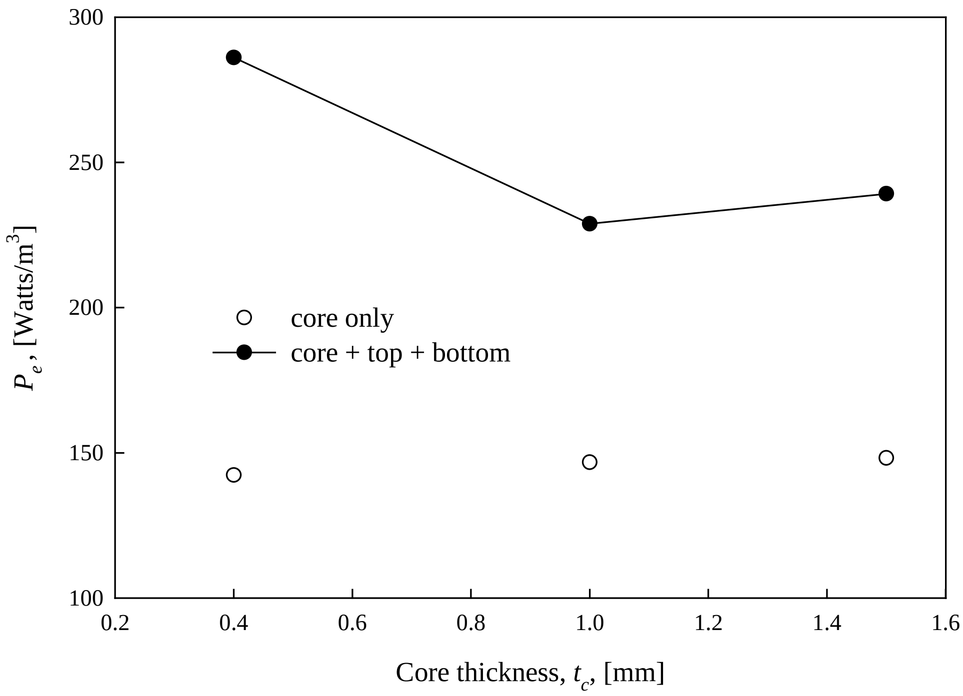

Fig. 4.10. P_e vs t_c keeping $\rho_c t_c = 10^{-7}\ \Omega\text{m}^2$.

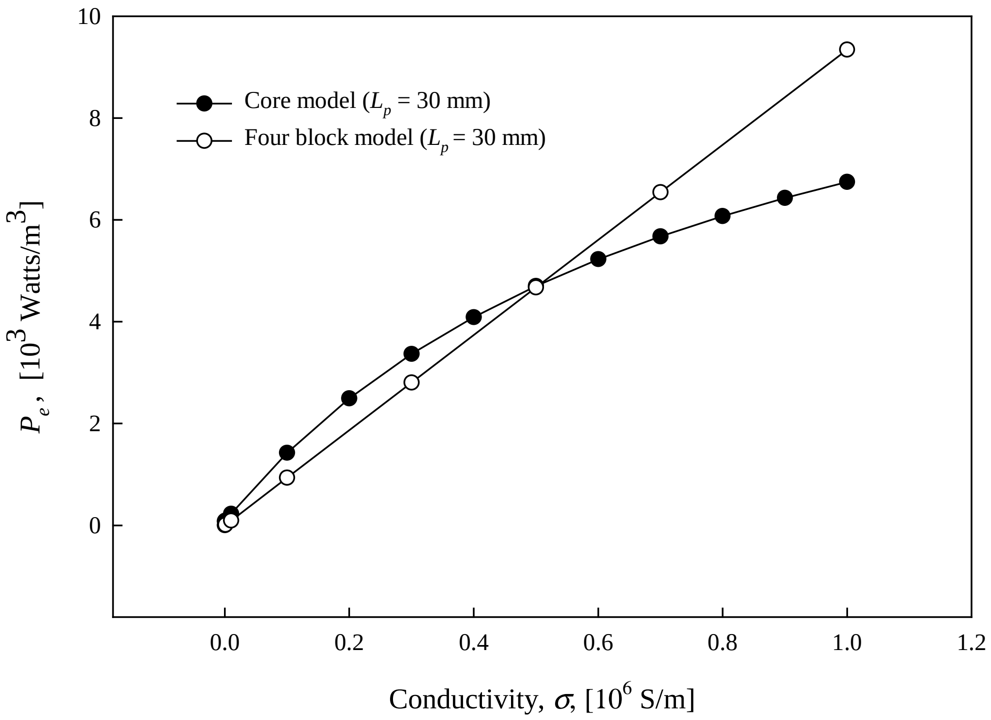

Fig. 4.11. P_e vs core conductivity for the four-block model and block model with resistive core.

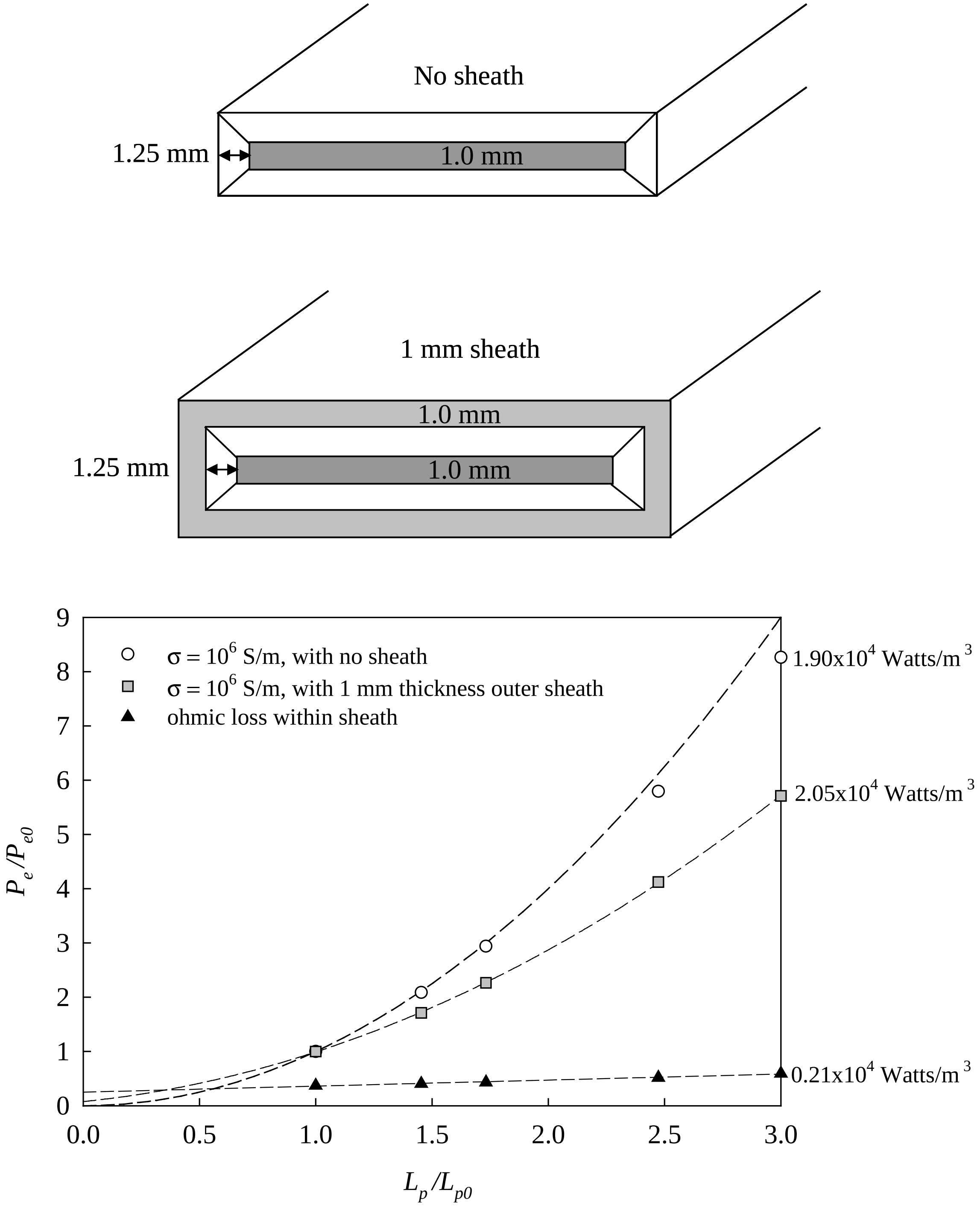

Fig. 4.12. Effect of an outer sheath on P_e.

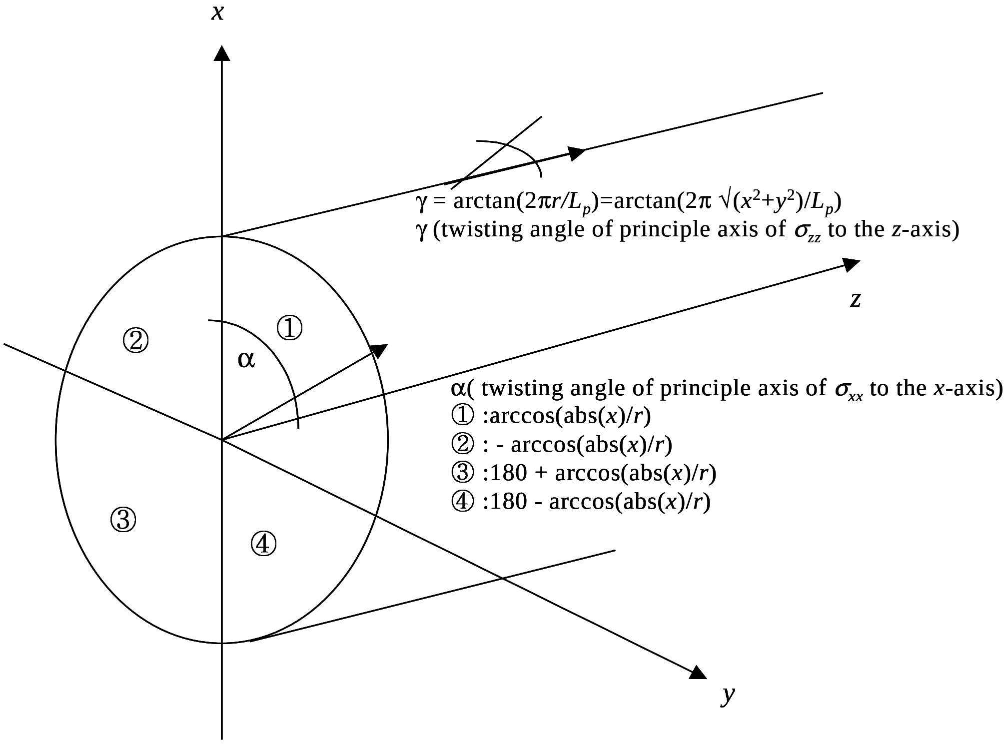

Fig. 4.13. Conductivity tensor definition for a cylindrical four-block model.

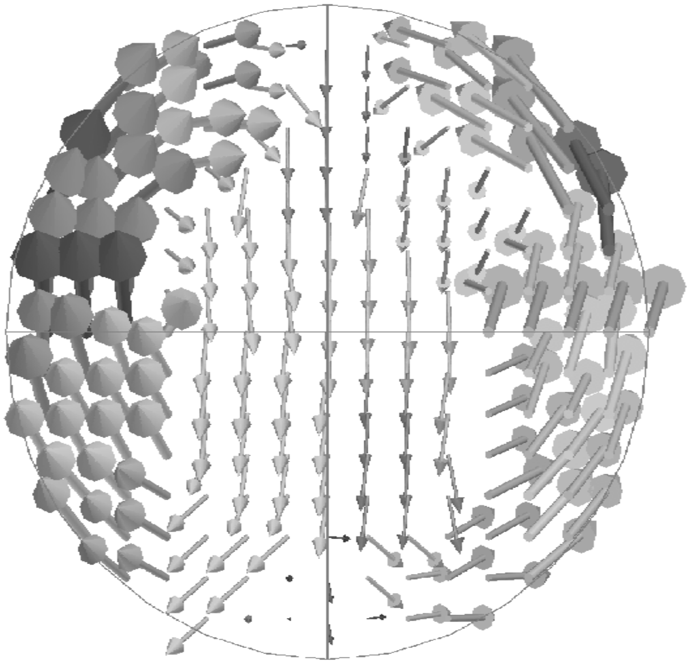

Fig. 4.14. Current distribution for the cylindrical four-block model. Projection to the cross section of the sample.

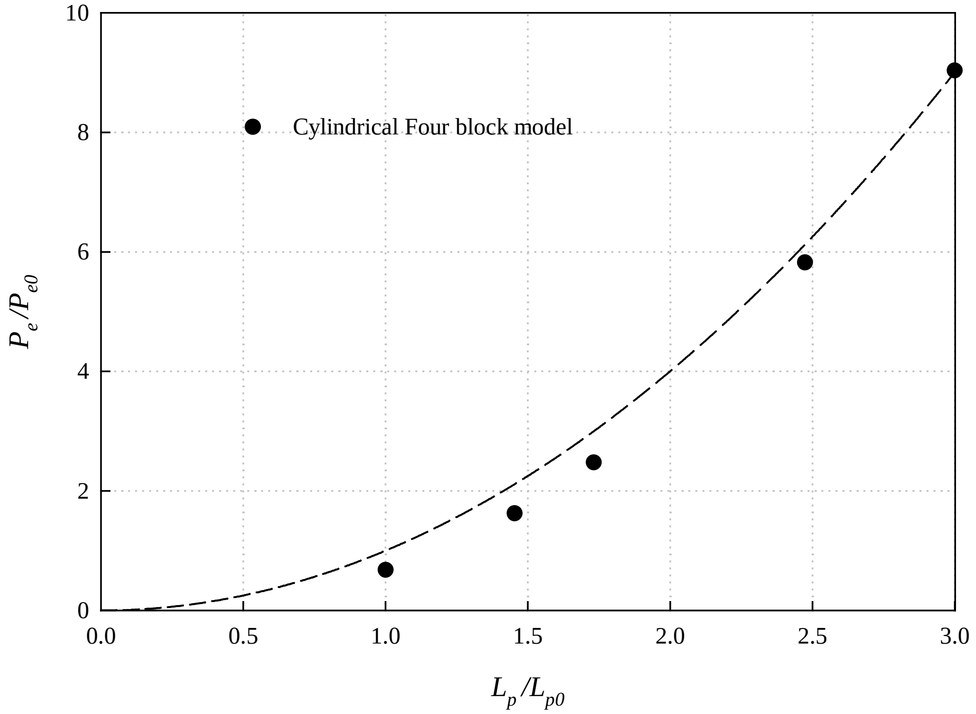

Fig. 4.15. P_e vs. L_p for the cylindrical four-block model.

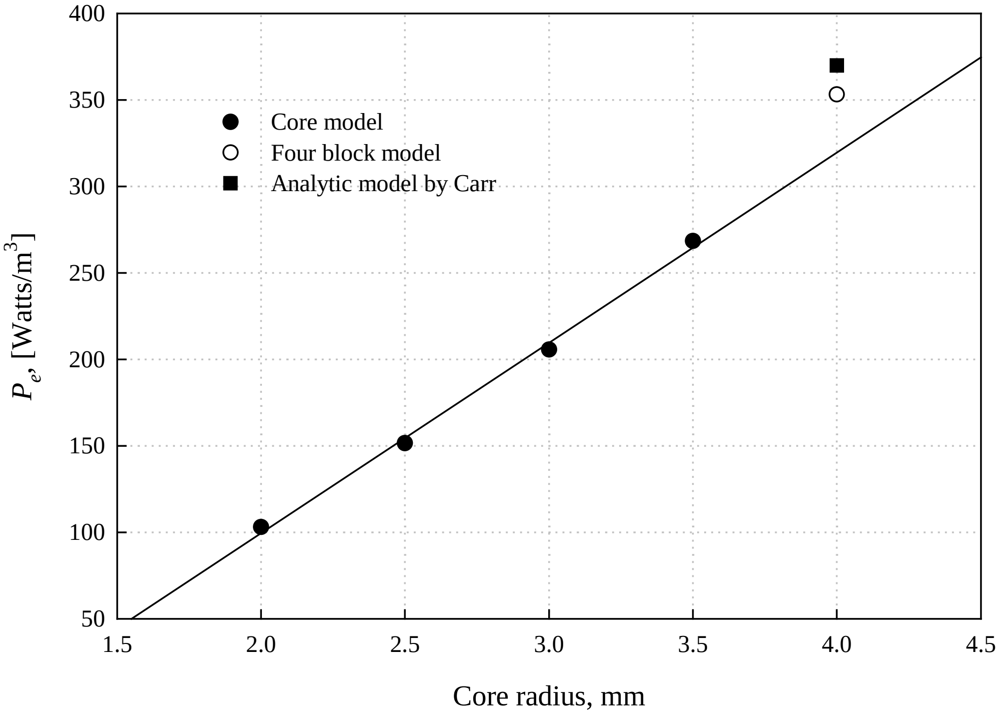

Fig. 4.16. P_e vs. core radius and a comparison to the analytic model.

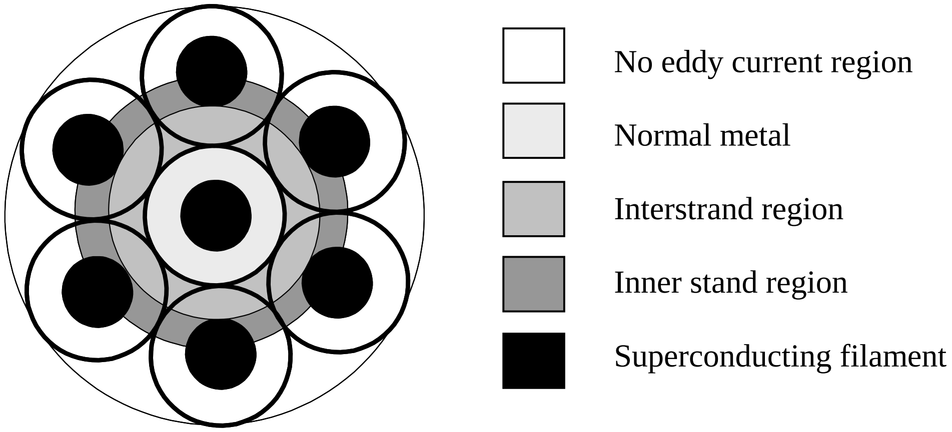

Fig. 4.17. Schematic for a simple model of a seven-strand cable. White region (No eddy current region) is excluded from the numerical simulation. Normal metal and the superconducting filament regions are isotropic. The remaining interstrand region and inner strand region are further divided into four blocks to simulate the twisting effect.

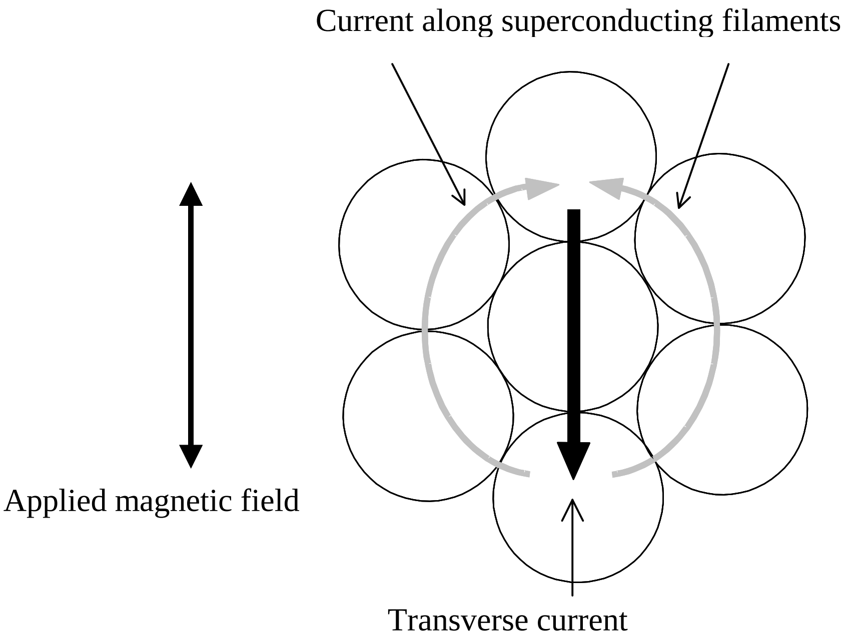

Fig. 4.18 Current distribution in a seven-strand cable.

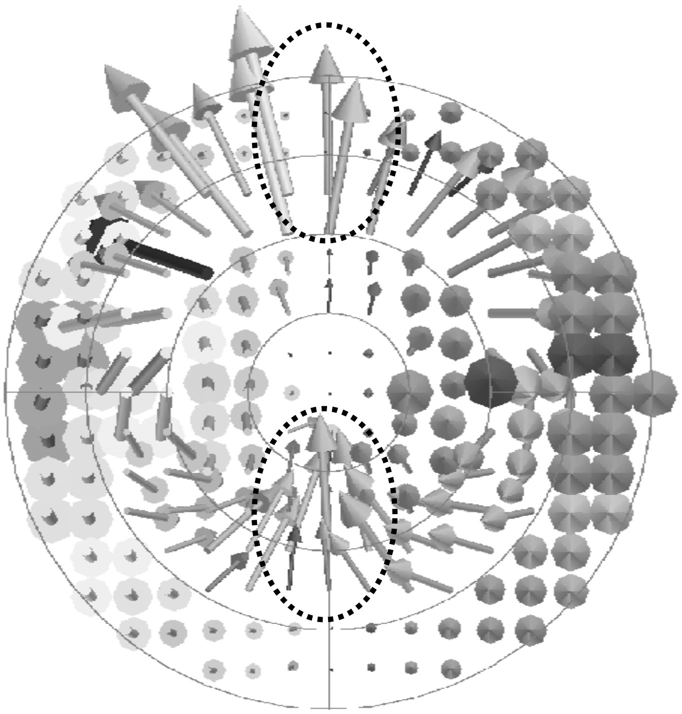

Fig. 4.19. Current distribution for the seven-strand cable model. Projection to the cross section of the sample. The current inside the dotted line is the transverse current for eddy current coupling loss, other currents are along the superconducting filament.

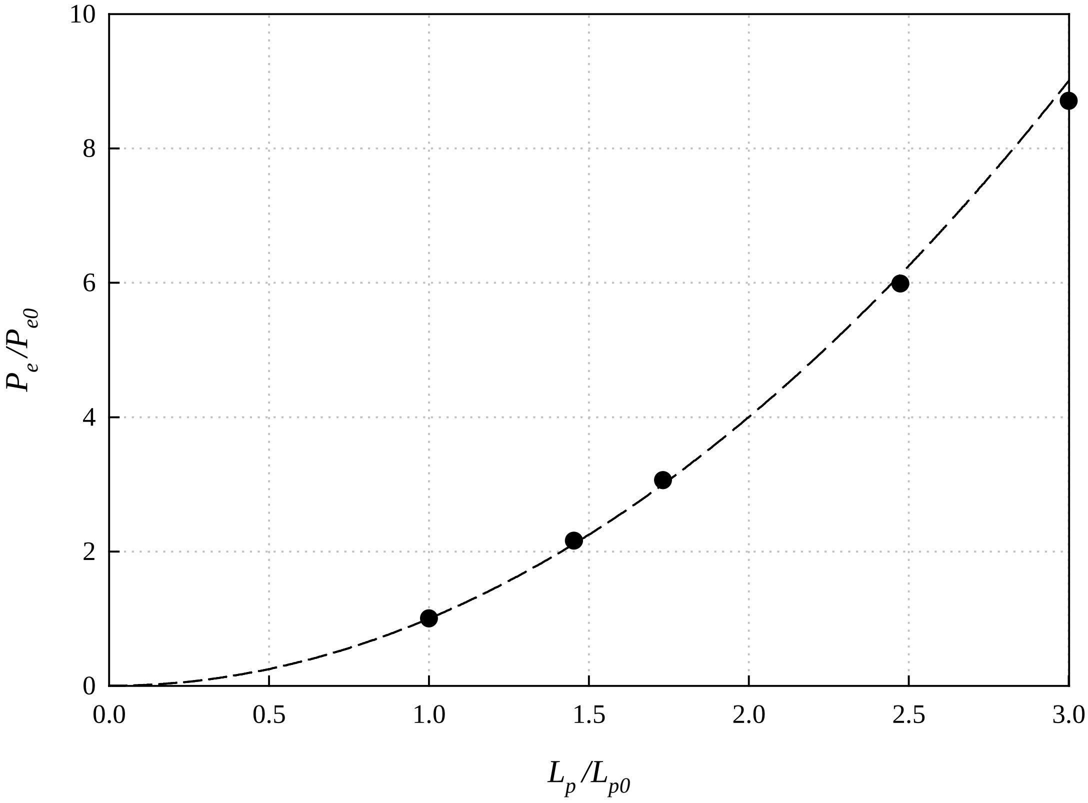

Fig. 4.20. Eddy current coupling loss of a seven-strand model with respect to twist pitch. Only the transverse current in interstrand and matrix region are considered.

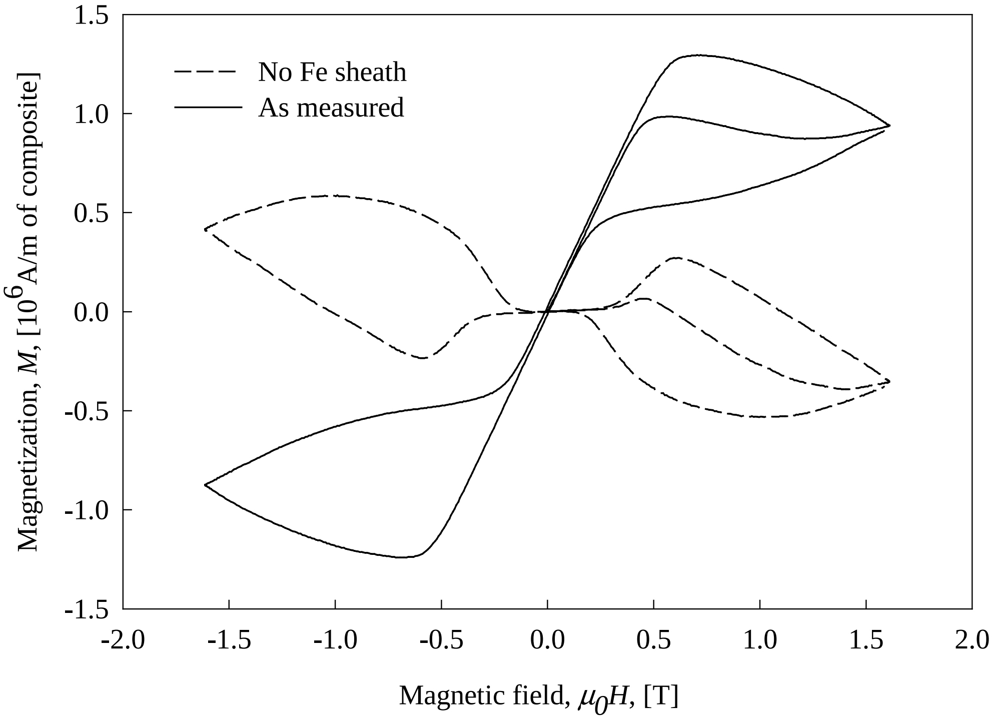

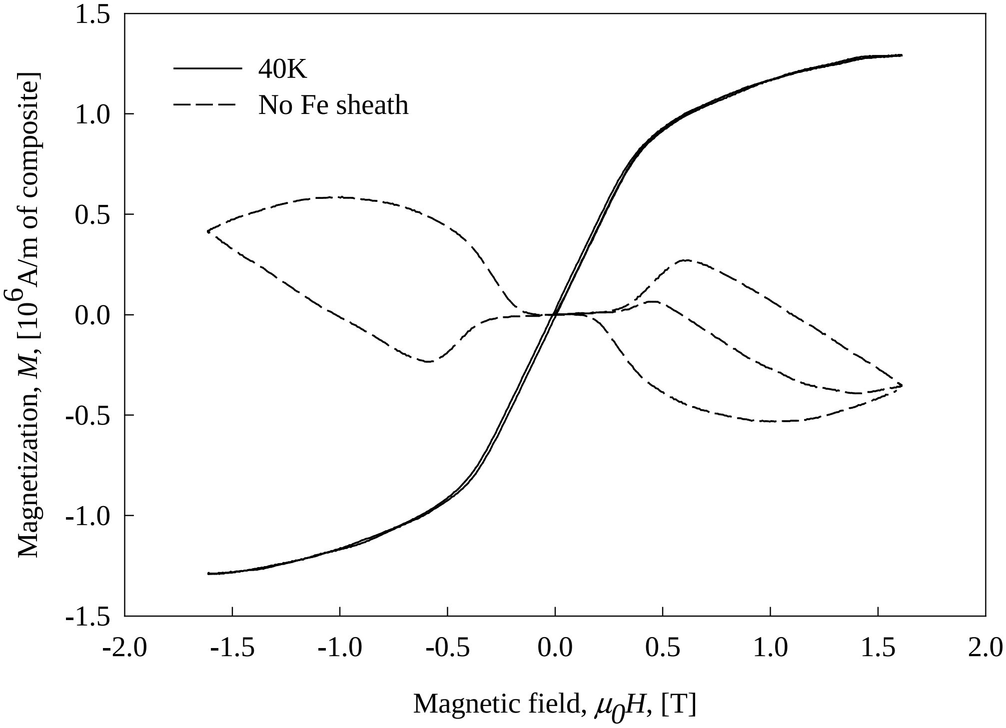

Fig. 4.21. *M-H* loops of an MgB_2 strand with an Fe matrix. No Fe sheath *M-H* loop is obtained by subtracting 40 K signal from the as measured signal.

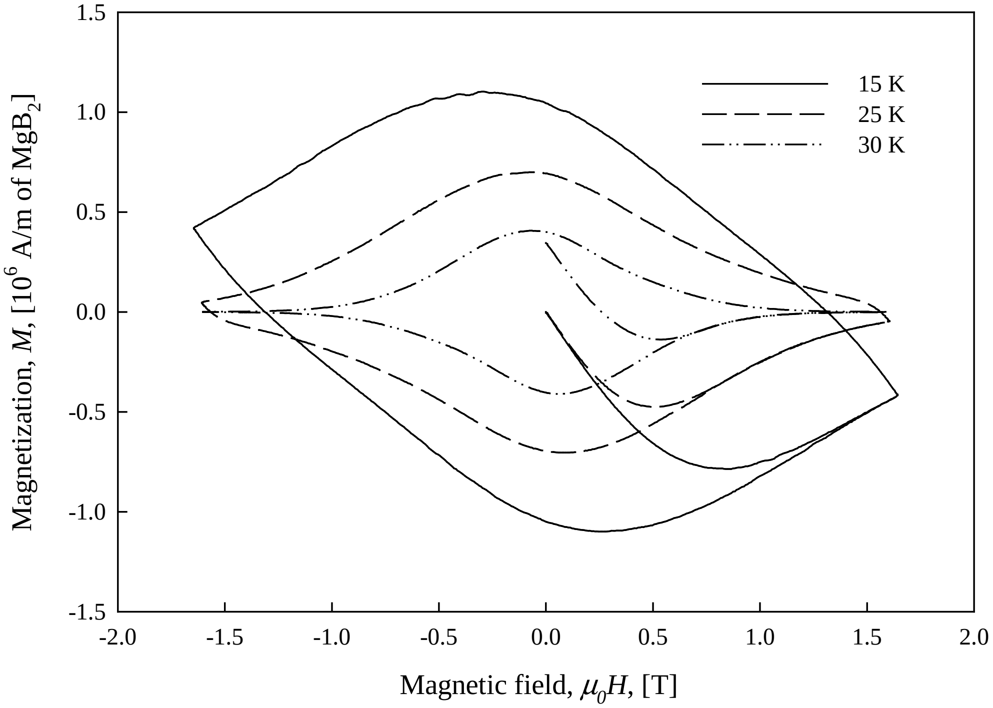

Fig. 4.22. *M-H* loops of a bulk MgB_2 superconductor with no Fe matrix at various temperatures.

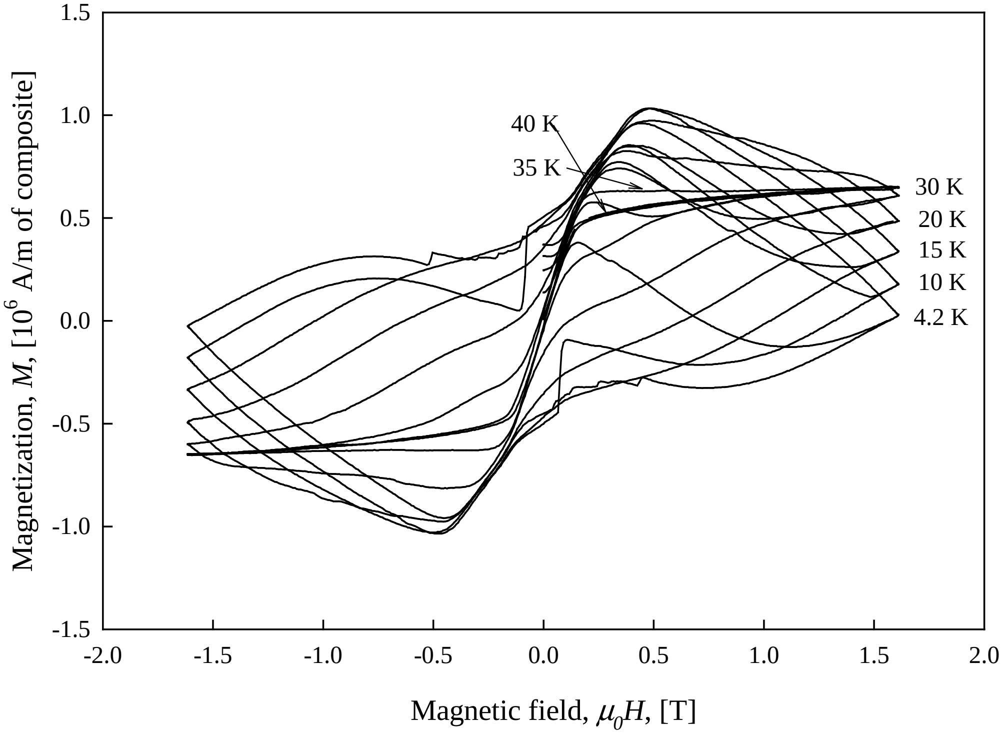

Fig. 4.23. Magnetic shielding effect at various temperatures.

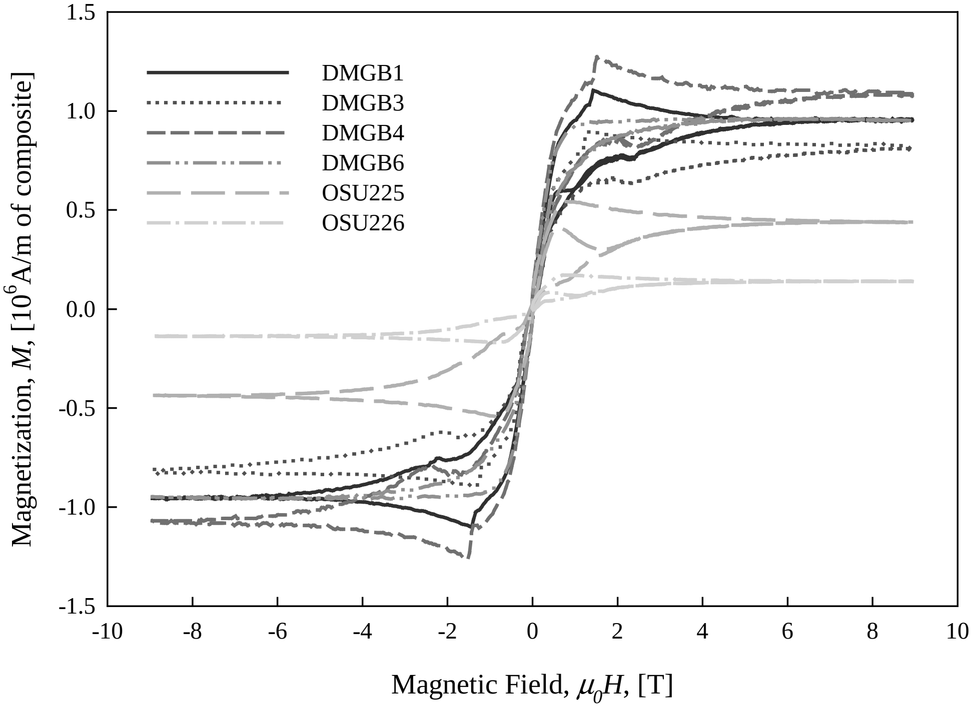

Fig. 4.24. *M-H* loops of MgB_2/Fe strands measured at 4.2 K in 9 T VSM.

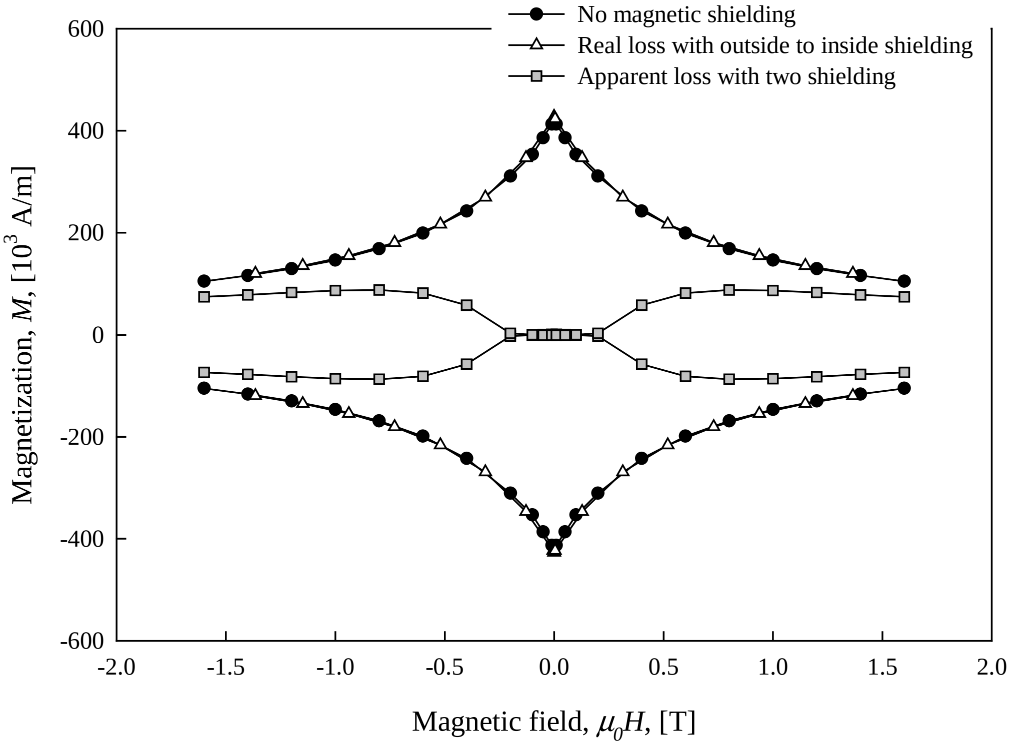

Fig. 4.25. *M-H* loops generated by numerical calculation.

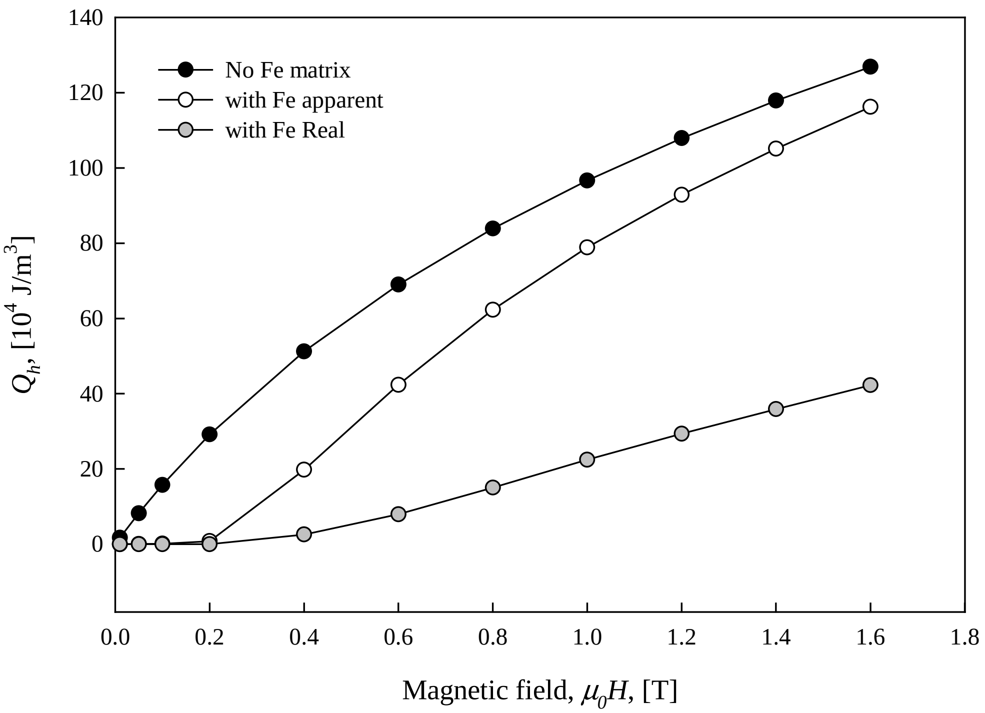

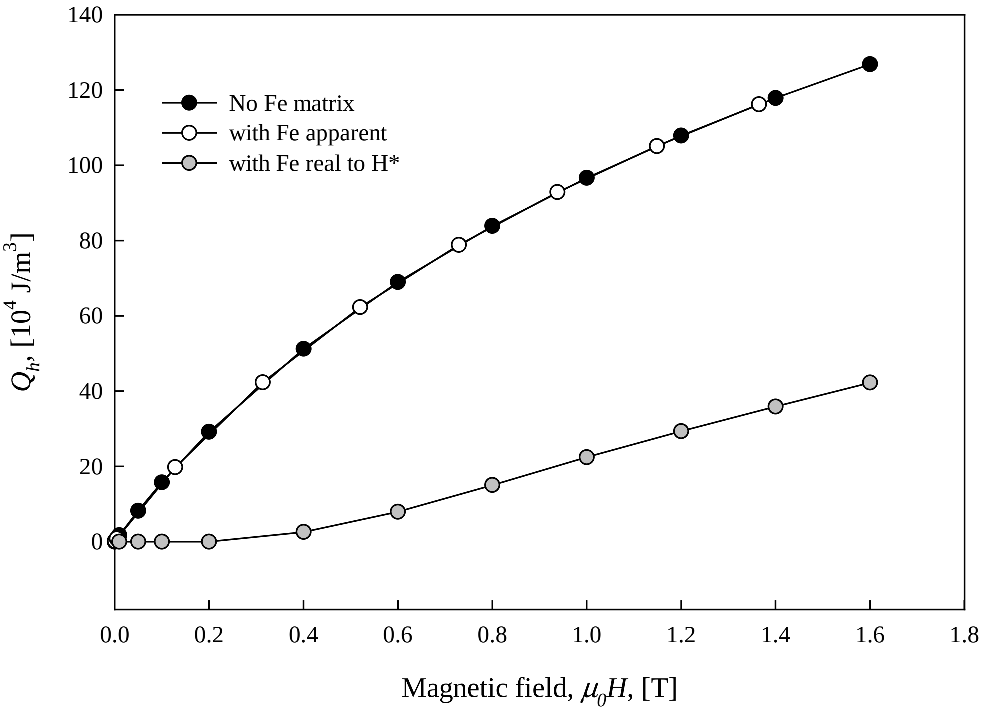

Fig. 4.26. AC loss (hysteresis loss) derived from *M-H* loops. The graph below shows the Real loss with respect *H**. *H** is the field the superconducting filaments experience inside the Fe matrix.

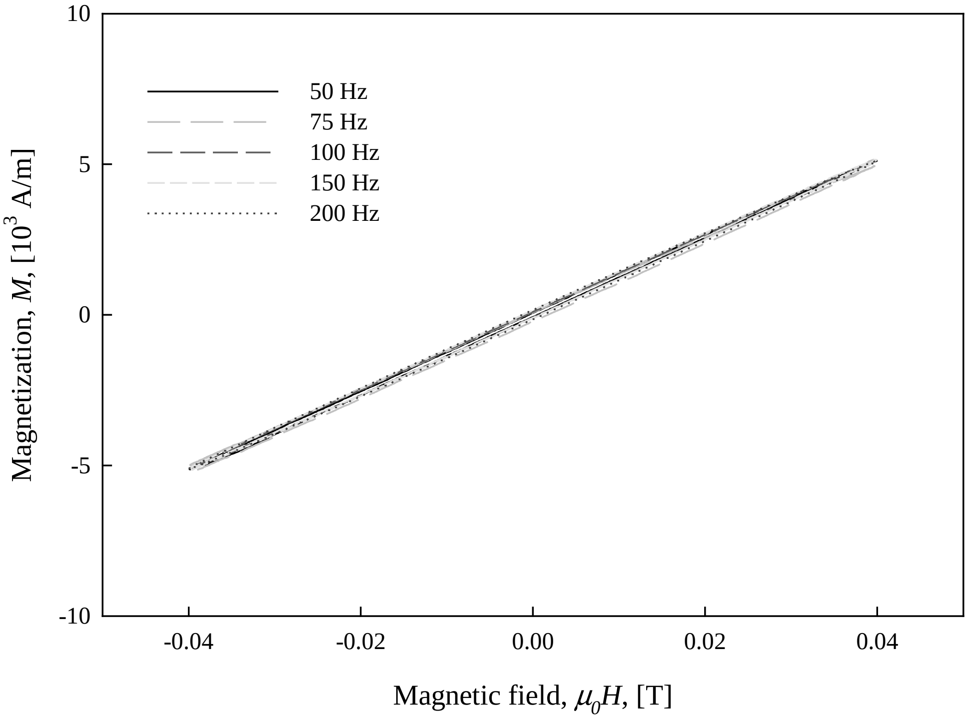

Fig. 4.27. *M-H* loops of SAE30 oil coated sample at 4.2 K by the pick-up coil method.

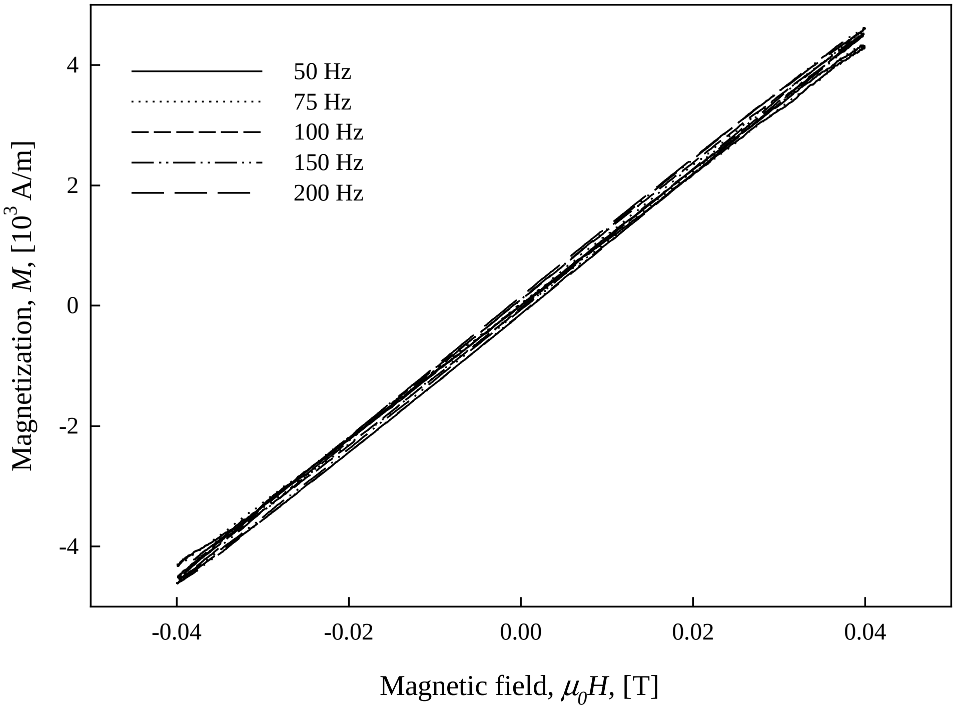

Fig. 4.28. *M-H* loops of paint coated sample at 4.2 K by pick-up the coil method.

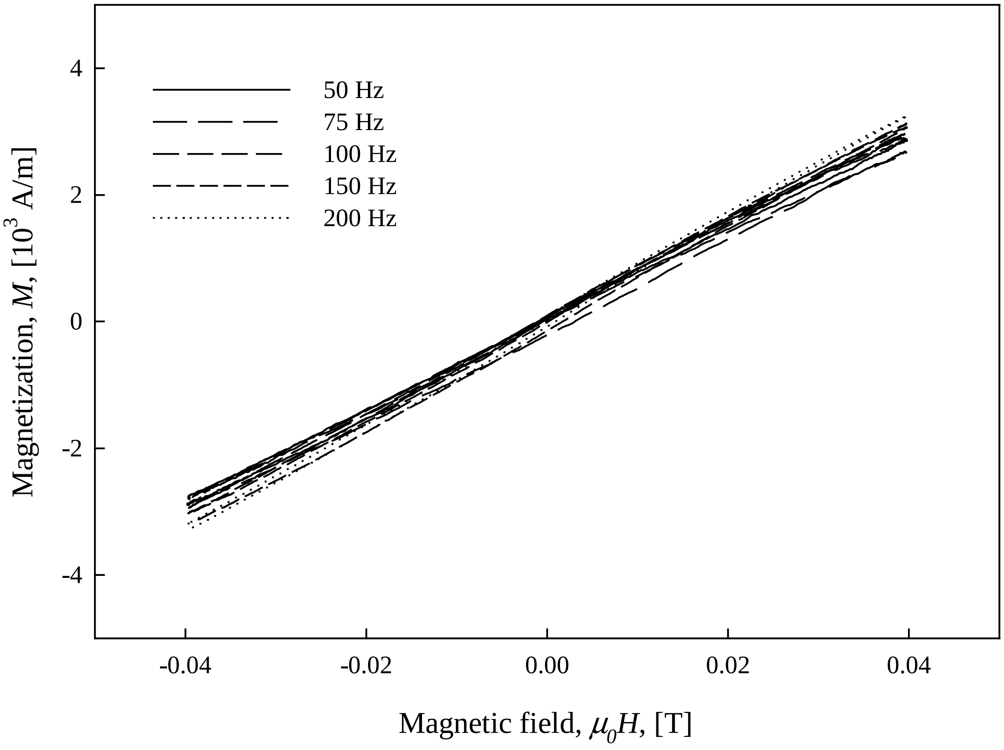

Fig. 4.29. *M*-*H* loops of uncoated sample with no Fe layer at 4.2 K by the pick-up coil method.

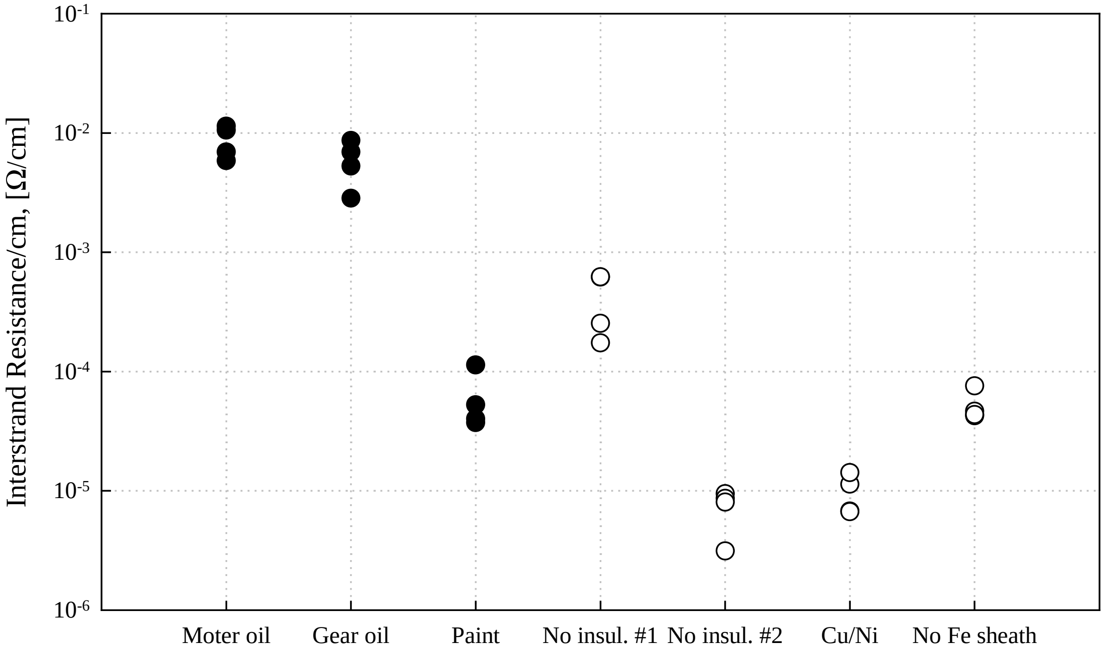

Fig. 4.30. Contact resistance in MgB$_2$ cables at 4.2 K with various insulating layers.

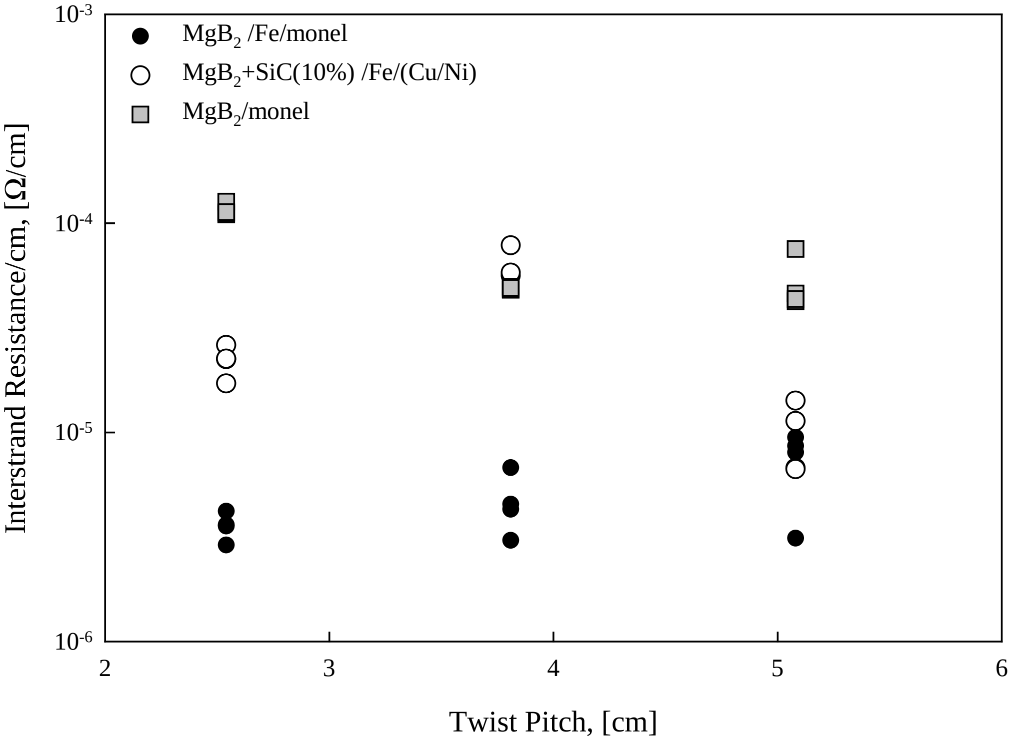

Fig. 4.31. Effect of twist pitch on the contact resistance of MgB$_2$ cables at 4.2 K .

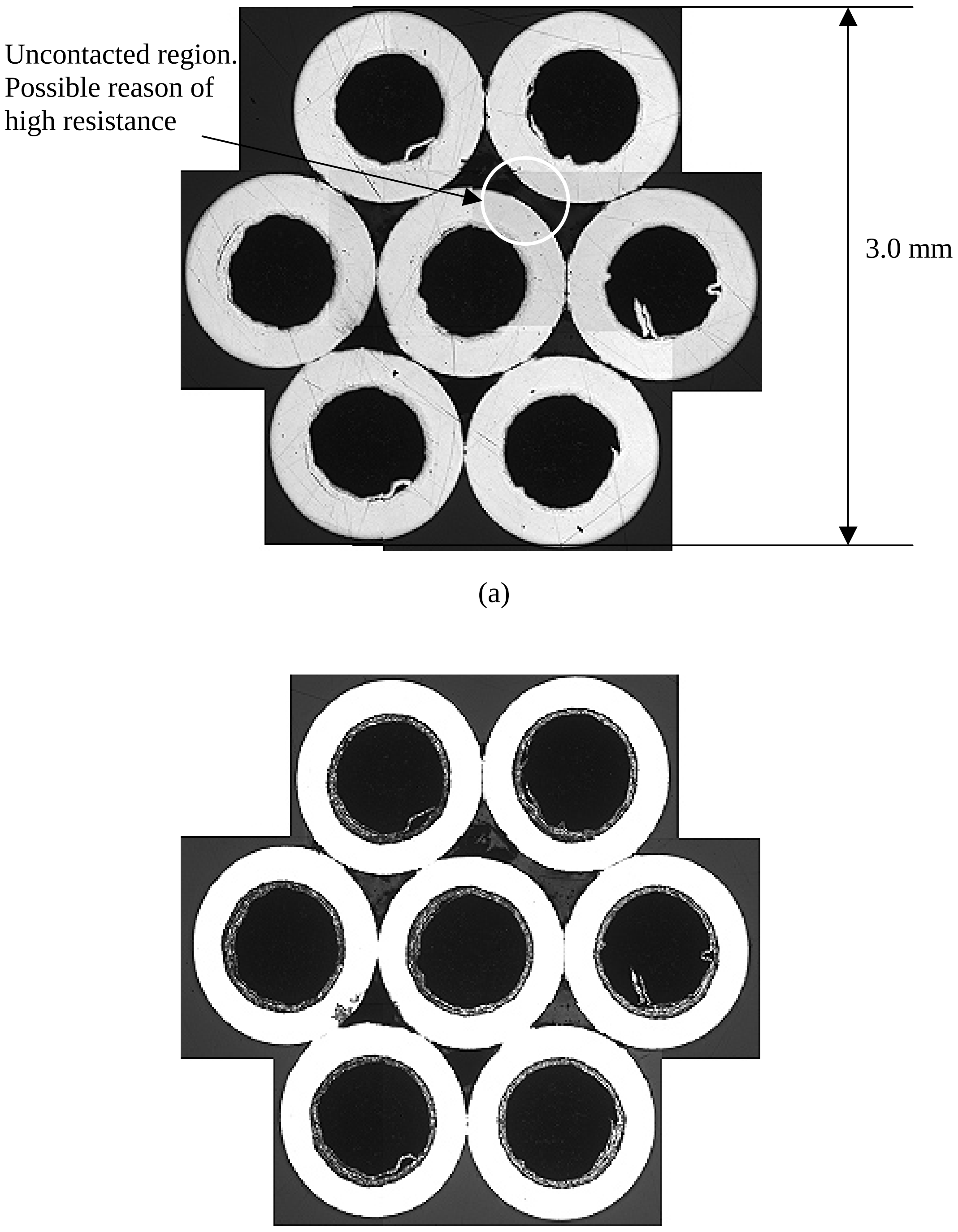

(a)

(b)

Fig. 4.32. Optical microscopy of MgB_2 cable insulated using SAE30 oil. (a) before etching Fe layer surrounding MgB_2 superconducting filaments. (b) after etching Fe layer surrounding MgB_2 superconducting filaments.

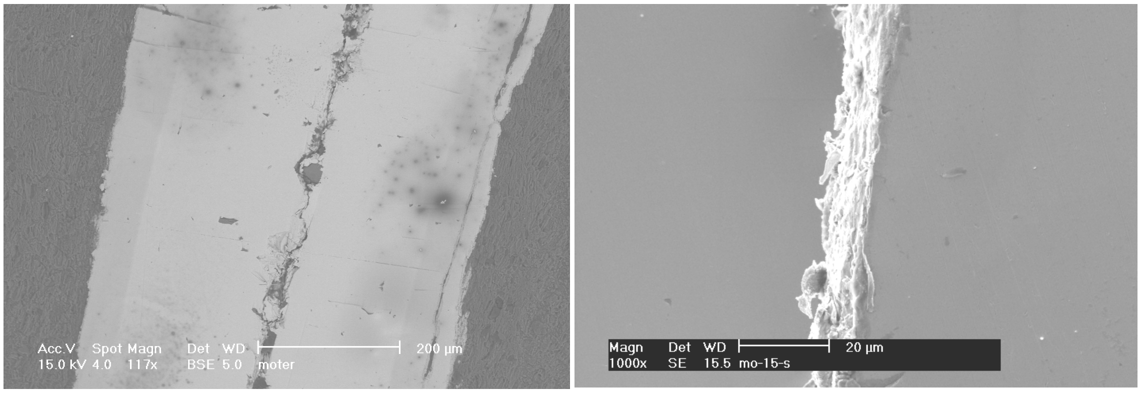

Surface coated sample (MOT01) with motor oil

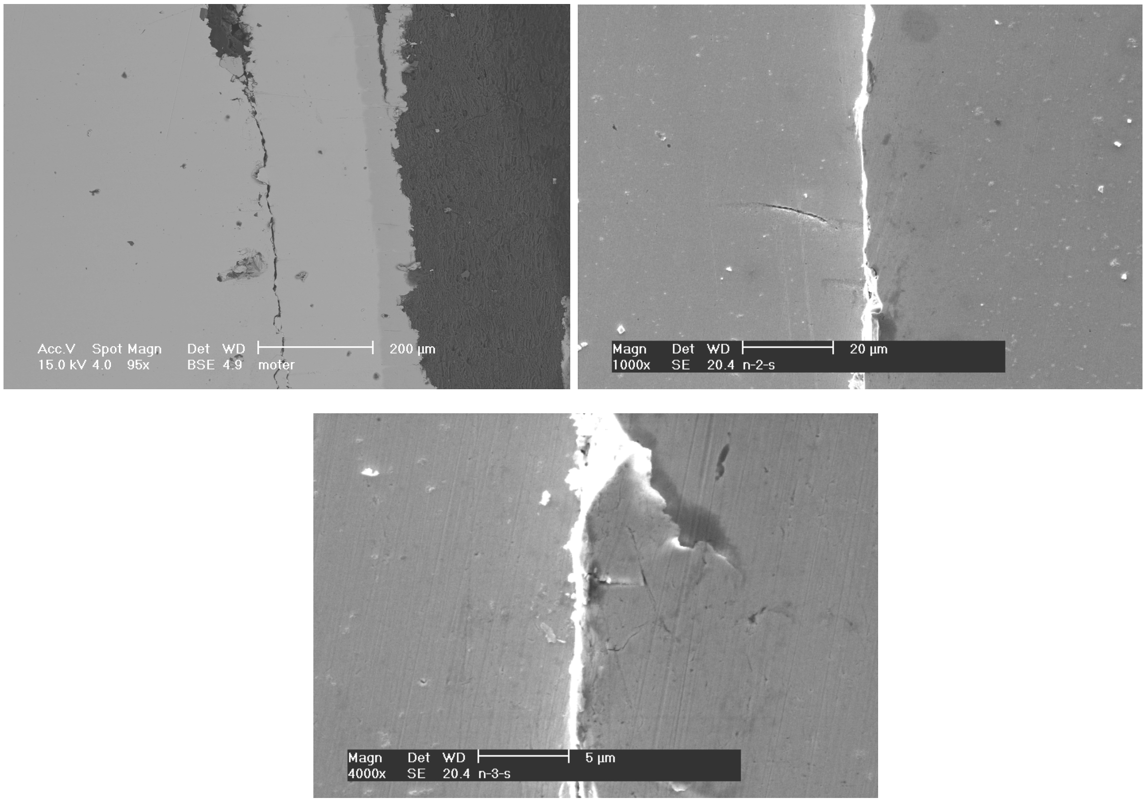

Sample (NOS03) without surface

Fig. 4.33. SEM images of the interface between stands of an MgB_2 cable.

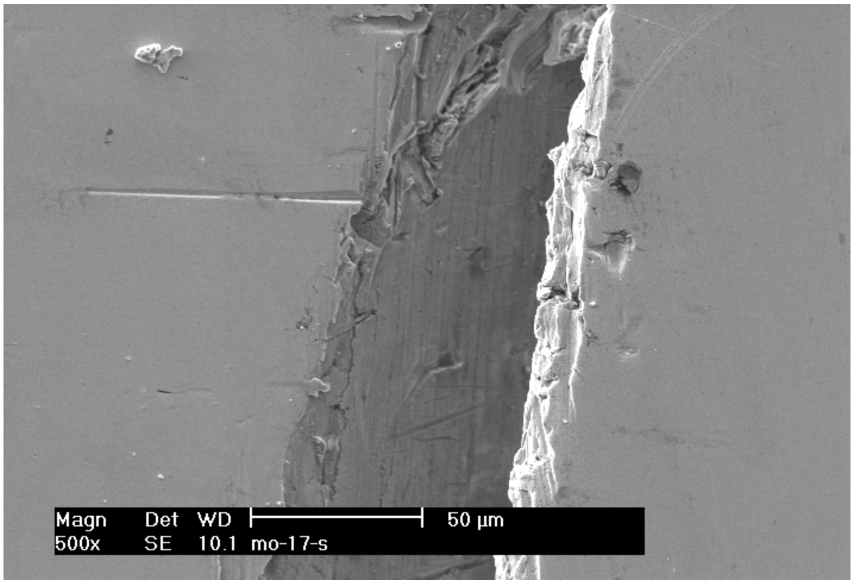

Surface coated sample (MOT01) with motor oil.
Oxygen content at surface: 5.10 At. %
Oxygen content inside matrix: 1.23 At. %

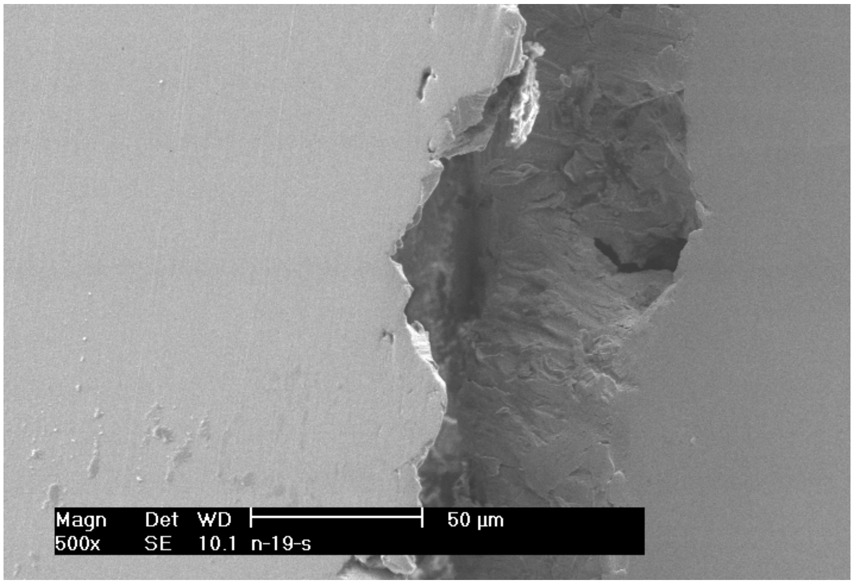

Sample (NOS03) without insulation coating.
Oxygen content at surface: 3.60 At. %
Oxygen content inside matrix: 1.87 At. %

Fig. 4.34. EDS analysis of oxygen of an MgB_2 cable.

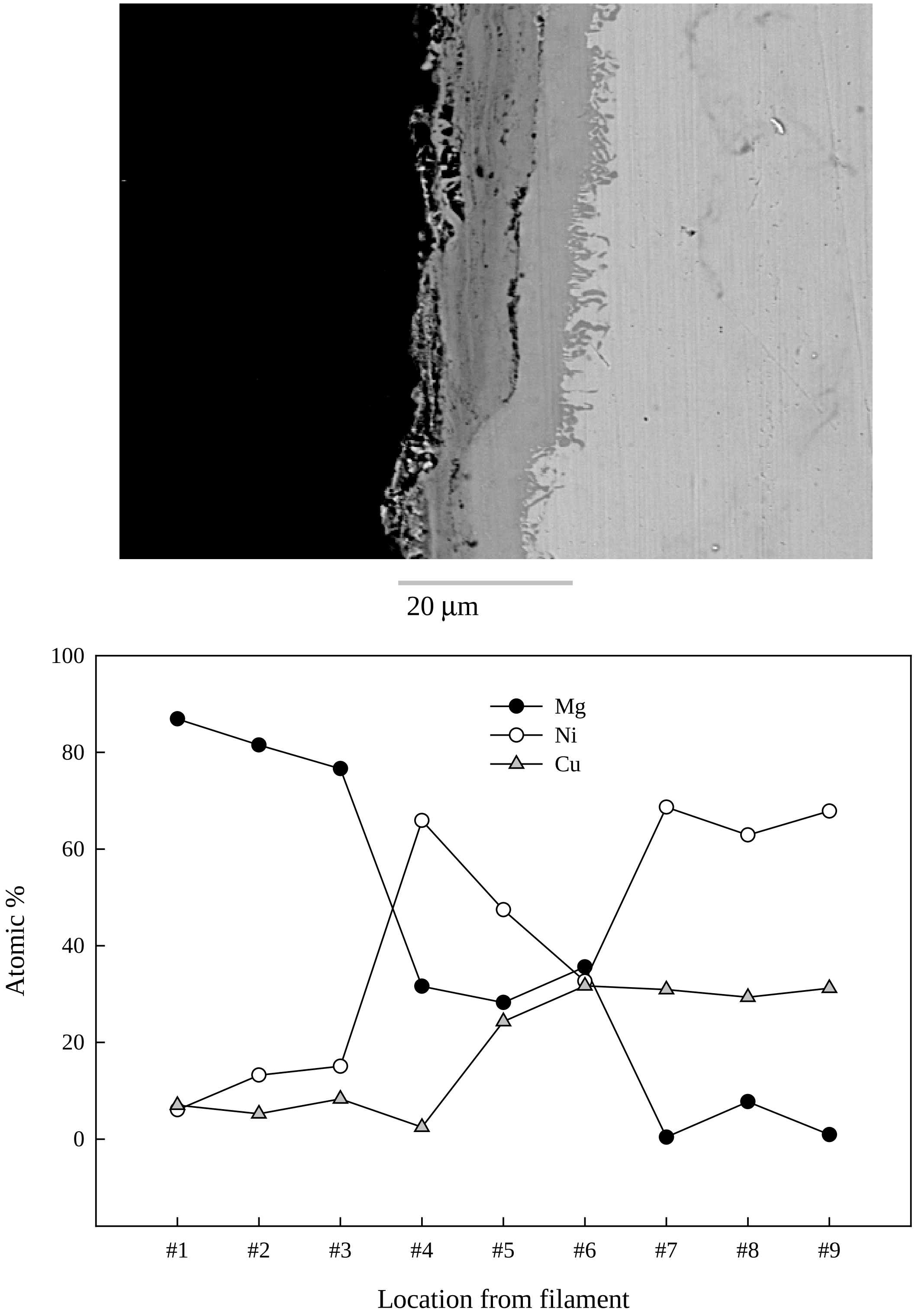

Fig. 4.35. BSE image and EDS analysis of sample without Fe layer.

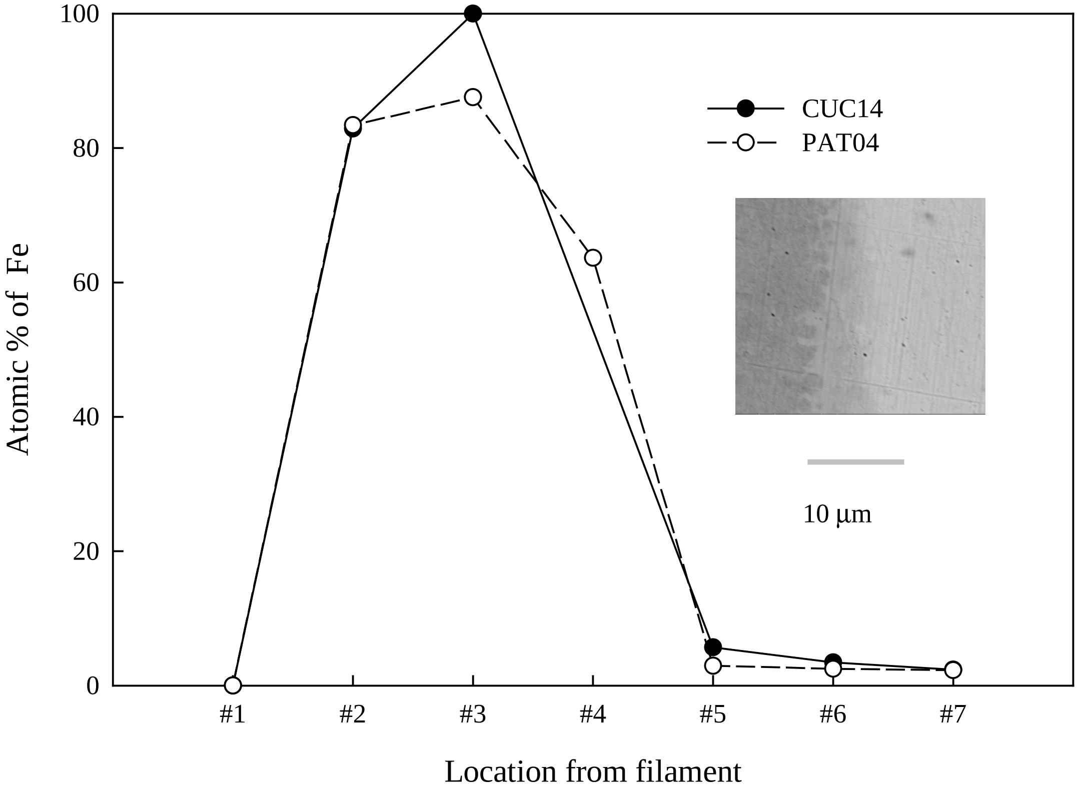

Fig. 4.36. EDS analysis of Fe in an MgB_2 cable. PAT04 shows some reaction between Fe and monel. However, no reaction can be found in CUC14 that has higher Cu composition. #4 location is the interface indicated in BSE picture.

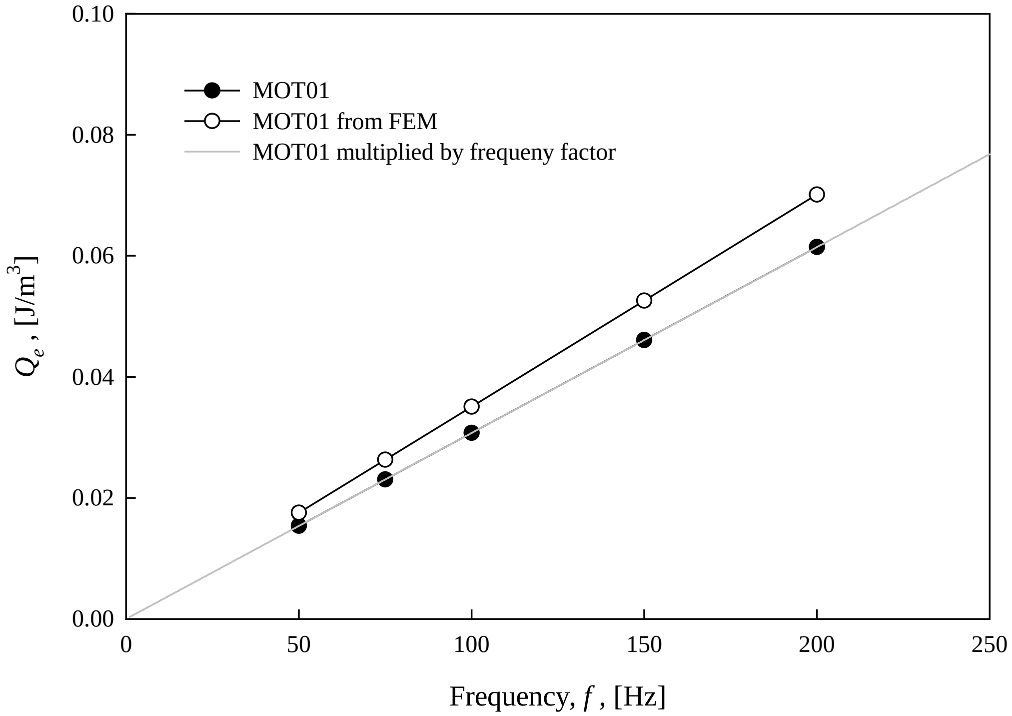

Fig. 4.37. Eddy current coupling loss of MOT01 at 4.2 K.

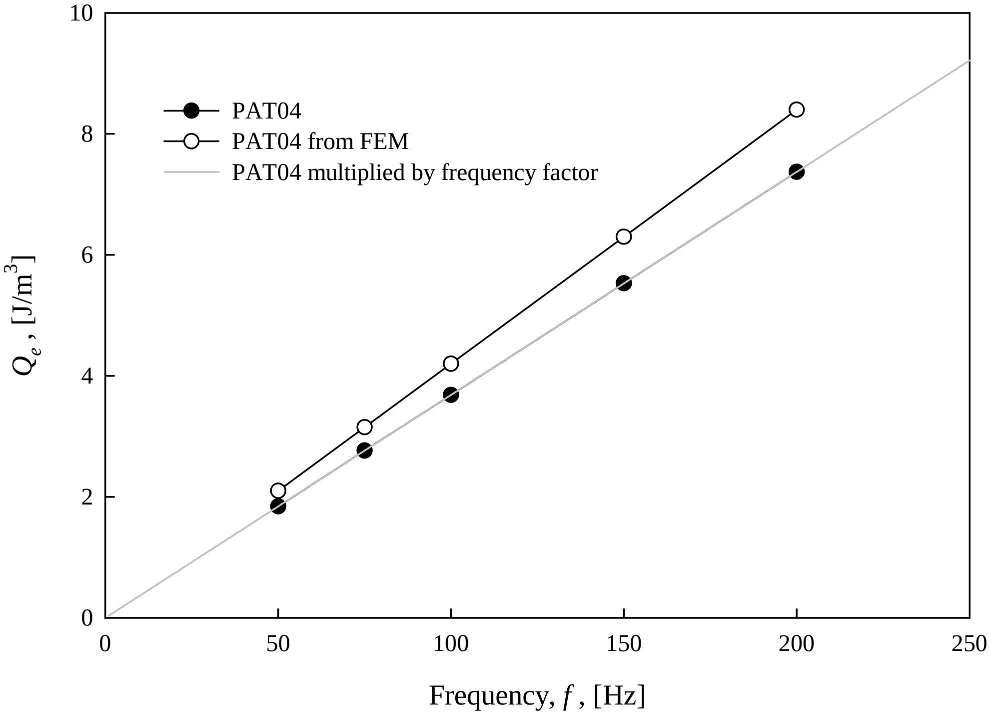

Fig. 4.38. Eddy current coupling loss of PAT04 at 4.2 K.

REFERENCES FOR CHAPTER 4

[1] W. J. Carr, *AC loss and macroscopic theory of superconductors*, 2 ed. New York: Tayor and Francis, 2001.

[2] M. N. Wilson, *Superconducting magnets*, 1 ed. New york: Oxford University Press, 1983.

[3] V. E. Sytnikov, G. G. Svalov, S. G. Akopov, and I. B. Peshkov, "Coupling losses in superconducting transposed conductors located in changing magnetic fields," *Cryogenics*, vol. 29, pp. 926-930, 1989.

[4] V. E. Sytnikov and I. B. Peshkov, "Coupling losses for superconducting cables in pulsed fields," *Advances in cryogenic engineering*, vol. 40, pp. 537-542, 1994.

[5] G. H. Morgan, "Eddy currents in flat metal-filled superconducting braids," *Journal of Applied Physics*, vol. 44, pp. 3319-3322, 1973.

[6] N. Banno, "Theoretical model of twisted high T_c superconducting tapes for numerical alternating-current loss claculations," *Journal of Applied Physics*, vol. 85, pp. 4243-4249, 1999.

[7] W. J. Carr and V. Kovachev, "Interstrand eddy current losses in rutherford cable," *Cryogenics*, vol. 35, pp. 529-534, 1995.

[8] M. D. Sumption, E. Lee, and E. W. Collings, "Influence of filamentary and strand aspect ratios on AC loss in short, untwisted samples of HTSC and LTSC superconducting multifilamentary composites," *Physica C*, vol. 337, pp. 187-194, 2000.

[9] M. D. Sumption, E. Lee, S. X. Dou, and E. W. Collings, "Extraction of matrix resistivity from short samples of superconducting multifilamentary composite tapes: Influence of strand twist and internal structure," *Physica C*, vol. 335, pp. 164-169, 2000.

[10] A. M. Campbell, "A general treatment of AC losses in multifilamentary superconductors," *Cryogenics*, pp. 3-16, 1982.

[11] A. C. Rose-innes, *Introduction to superconductivity*, 2nd ed. Oxford, New York: Pergamon Press, 1978.

[12] E. Lee, M. D. Sumption, and E. W. Collings, "FEM modeling of AC loss in rutherford cables with and without resistive cores," presented at CEC/ICMC, Anchorage, Alaska, 2003.

[13] M. D. Sumption, E. W. Collings, R. M. Scanlan, A. Nijhuis, and H. H. J. ten Kate, "Core-suppressed AC loss and strand-moderated contact resistance in a Nb_3Sn Rutherford cable," *Cryogenics*, vol. 39, pp. 1-12, 1999.

[14] M. D. Sumption, E. W. Collings, A. Nijhuis, and R. M. Scanlan, "Coupling current control in stabrite-coated NbTi Rutherford cables by varying the width of

a stainless steel core," *Advances in cryogenic engineering*, vol. 46B, pp. 1043-1049, 2000.

[15] M. Dhalle, A. Polcari, F. Marti, G. Witz, Y. B. Huang, R. Flukiger, S. Clerc, and K. Kwasnitza, "Reduced filament coupling in Bi(2223)/$BaZrO_3$/Ag composite tapes," *Physica C*, vol. 310, pp. 127-131, 1998.

[16] H. Eckelmann, "AC losses in multifilamentary Bi(2223) tapes with an interfilamentary resistive carbonate barrier," *Physica C*, vol. 310, pp. 122-126, 1998.

[17] W. Goldacker, M. Quilitz, B. Obst, and H. Eckelmann, "Novel resistive interfilamentary carbonate barriers in multifilamentary low AC loss tapes," presented at Applied superconductivity Conference, Palm Desert, CA, 1998.

[18] K. Kwasnitza, S. Clerc, R. Flukiger, and Y. B. Huang, "Reduction of alternating magnetic field losses in high T_c multifilament Bi(2223)/Ag tapes by high resistive barriers," *Cryogenics*, vol. 39, pp. 829-841, 1999.

[19] R. P. Reed and A. F. Clark, *Materials at low temperature*: American Society for Metals, 1983.

[20] M. D. Sumption, E. W. Collings, R. M. Scanlan, S. W. Kim, M. Wake, T. Shintomi, A. Nijhuis, and H. H. J. ten Kate, "AC loss and interstrand contact resistance in bare and coated NbTi/Cu Rutherford cables with cores," *Supercond. Sci. Technol.*, vol. 14, pp. 888-897, 2001.

[21] M. D. Sumption, H. H. J. ten Kate, R. M. Scanlan, and E. W. Collings, "Contact resistance and cable loss measurements of coated strands and cable wound from them," *IEEE transactions on applied superconductivity*, vol. 5, pp. 692-696, 1995.

[22] M. D. Sumption, E. W. Collings, R. M. Scanlan, A. Nijhuis, H. H. J. ten Kate, S. W. Kim, M. Wake, and T. Shintomi, "Influence of strand surface condition on interstrand contact resistance and coupling loss in Nb-Ti wound Rutherford cables," *Cryogenics*, vol. 39, pp. 197-208, 1999.

[23] S. Soltanian, X. L. Wang, I. Kusevic, E. Babic, A. H. Li, M. J. Qin, J. Horvat, H. K. Liu, E. W. Collings, E. Lee, M. D. Sumption, and S. X. Dou, "High transport critical current density above 30 K in pure Fe-clad MgB_2 tape," *Physica C*, vol. 361, pp. 84-90, 2001.

[24] M. D. Sumption, E. Lee, E. W. Collings, X. L. Wang, and S. X. Dou, "Suppression of AC(hysteretic) loss by magnetic shielding of MgB_2/Fe superconductors: The Pseudo-Meissner effect," *Advances in cryogenic engineering*, vol. 48, pp. 824, 2001.

[25] S. Soltanian, J. Horvat, X. L. Wang, P. Munroe, and S. X. Dou, "Effect of nano-carbon particle doping on the flux pinning properties of MgB_2 superconductor," *Physica C*, vol. 390, pp. 185-190, 2003.

[26] S. Soltanian, M. J. Qin, S. Keshavarzi, X. L. Wang, and S. X. Dou, "Effect of sample size on the magnetic critical current density in nano-SiC doped MgB_2 superconductors," *Physical Review B*, vol. 68, pp. 134509, 2003.

[27] X. L. Wang, S. H. Zhou, M. J. Qin, P. Munroe, S. Soltanian, H. K. Liu, and S. X. Dou, "Significant enhancement of flux pinning in MgB_2 superconductor through nano-Si addition," *Physica C*, vol. 385, pp. 461-465, 2003.

[28] M. D. Sumption, E. W. Collings, E. Lee, X. L. Wang, S. Soltanian, and S. X. Dou, "Reduction and elimination of external-field AC loss in MgB_2/Fe wire by in situ magnetic shielding," *Physica C*, vol. 378-381, pp. 894-898, 2002.
[29] M. D. Sumption, E. W. Collings, E. Lee, X. L. Wang, S. Soltanian, S. X. Dou, and M. Tomsic, "Real and apparent loss suppression in MgB_2 superconducting composites," *Physica C*, vol. 382, pp. 98-103, 2002.
[30] A. Nijhuis, H. H. J. ten Kate, J. L. Duchateau, and P. Decool, "Control of contact resistance by strand surface coating in 36-strand NbTi CICCs," *Cryogenics*, vol. 41, pp. 1-7, 2001.
[31] K. Kwasnitza and S. Clerc, "Coupling current loss reduction in cable-in-conduit superconductors by thick chromium oxide coating," *Cryogenics*, vol. 38, pp. 305--308, 1998.
[32] P. I. Dolgosheev, G. G. Svalov, V. E. Sytnikov, I. V. Podyablonskaya, and G. K. Matshueva, "Transversal conductivity in conductors of "Cable in conduit" type," *IEEE transactions on applied superconductivity*, vol. 5, pp. 749-752, 1995.
[33] K. Seo, K. Fukuhara, and M. Hasegawa, "Analysis for inter-strand coupling loss in multi-strand superconducting cable with distributed contact resistance between strands," *Cryogenics*, vol. 41, pp. 131-137, 2001.
[34] H. Okamoto, *Phase diagrams of dilute binary alloys*: ASM international, 2002.
[35] H. Okamoto, *Desk handbook: Phase diagrams for binary alloys*: ASM international, 2000.

CHAPTER 5

SUMMARY AND CONCLUSIONS

The AC loss of superconducting composites with rectangular and round cross sections, especially the eddy current coupling loss component are has been calculated by discrete and continuous models. The eddy current loss of a rectangular cross section composite was successfully calculated by a simple four or five-block model based on an anisotropic continuum approach rather than a discrete approach (network model, lumped model) that has been used for the Rutherford cables (a type of rectangular cross section composite) so far. Block models with a different anisotropic effective resistivity in each block were used to describe the dependence of eddy current coupling loss of rectangular cross section composites on twist pitch, aspect ratio, core resistivity, core thickness, core width, and outer sheath. The eddy current coupling loss increases with the square of the twist pitch and the aspect ratio of the composite as predicted by both the anisotropic continuum model and the discrete model. Moreover, this block model successfully calculates the dependences of core thickness, width, and outer sheath, which have not been described by these existing two models. As the core thickness, width, and the core resistivity increases, the eddy current loss linearly decreases. There is little effect of the outer sheath on the eddy current coupling loss although a normal eddy current loss exists within outer sheath.

In the case of twisted round composites, the eddy current loss is also calculated using a block model and then compared with the existing analytical expression from the anisotropic continuum model. We can verify that the current distribution in both models as well as the calculated eddy current coupling loss are very similar. A block model for a particular discrete system (seven-strand MgB_2 cable) is also developed by modeling it as consisting of several layers, each with different resistivity tensors. Transverse current in the seven-strand model is restricted to the centeral part of the sample and is greatly reduced, compared to that of cylindrical conductor, leading to very low eddy current coupling loss.

Magnetic shielding caused by the Fe layer reduces the hysteresis loss of MgB_2 strands, an effect which almost totally suppresses the hysteresis loss below 0.2 T. The reduction of hysteresis loss is calculated using a two-dimensional numerical method. The real loss reduction is calculated assuming full magnetic field penetration and a field dependence of critical current as in Kim's model. The apparent loss reduction as shown from the *M-H* loops measured with VSM is always greater than the real loss reduction, since the signal from the superconducting filaments are also shielded by Fe layer, before it reaches the pick-up coil of VSM.

An alternative method for measuring the eddy current coupling loss of MgB_2 seven strand cables was developed using the measured contact resistance between the strands. From the contact resistance averaged over the sample length measured by a four-point method, the eddy current coupling loss of MgB_2 seven strand cable is easily calculated. Since there are seven strands in a cable, the contact resistance between the strands is extracted using

$$R_c = \frac{273R_1}{60} = \frac{283R_2}{60} = \frac{258R_3}{60} = \frac{234R_4}{60}$$

This contact resistance is further normalized by multiplying the number of eddy current paths by $L_s / 2r$. Then, using this R_c, the eddy current loss is given by

$$\frac{P_e}{V_s} = \frac{9\pi r^3 \dot{B}^2 L_p{}^2}{48\rho_\perp} \times \frac{(L_p / 2r)}{\pi(3r)^2 L_p} = \frac{\dot{B}^2 L_p{}^2}{96\rho_\perp} = \frac{\dot{B}^2 L_p{}^2}{32\pi r R_c} = \frac{\dot{B}^2 L_p}{16\pi R_c} \cdot N_e$$

Without direct measurements of AC loss by either VSM or pick-up coil method, the eddy current coupling loss can be predicted with this simple analytic method. If we consider primarily the current component causing the eddy current loss in the cables, the results of the eddy current loss calculated from the numerical seven-strand model and the analytical method using contact resistance are very close (12.5– 27 % difference). The experimental verification of these models for eddy current coupling loss still needs to be performed in future work

AC loss of superconducting composites can be calculated either by a continuum model or a discrete model. A comparison was made between these models by relating the contact resistance R_c and the effective resistivity of the composite and it is given by

$$\frac{N_s{}^2}{R_\perp} = \frac{8w^2}{\rho_\perp d}\frac{L_p}{4w} = \frac{2wL_p}{\rho_\perp d} = \frac{4wL_p}{\rho_\perp t}.$$

Then, then from the expression of a discrete model, the eddy current loss is given by

$$\frac{Q_e}{V_s} = \frac{2}{3}\frac{w}{t} L_p B_m \left(\frac{dB}{dt}\right)\left(\frac{N_s{}^2}{20R_\perp}\right) = \frac{2}{15}\left(\frac{w}{t}\right)^2 \frac{L_p{}^2}{\rho_\perp} B_m \left(\frac{dB}{dt}\right).$$

It is very close the loss expression from a continuum model (6.67 % difference).

The insulating layer at the interface of strands is shown to control the contact resistance between the strands in the cables. This contact resistance eventually controls the eddy current coupling loss of MgB_2 cables. The contact resistance of a sample with surface treatment is about two orders higher than that of a sample without any surface treatment. The differences at the interface of these samples are analyzed using SEM and EDS. Considering the equilibrium carbon composition in Cu and Ni from phase diagrams, carbon contamination is too high to compare the MgB_2 cables with and without surface treatment. However, the interface between strands of MgB_2 cable without surface treatment is clearer than that of MgB_2 cable with surface treatment. It is thought to be residue from SAE30 oil after doing 750 °C heat treatment. Oxygen composition at the interface of the MgB_2 cable is slightly higher in case of the cable with surface treatment.

Intermetallic compounds can be made from reactions between Mg with Cu or Ni. Fe layer between filaments and matrix can prevent these reactions, but Fe itself can diffuse to matrix materials. These intermetallic compounds and the diffusion of Fe can increase the transverse effective resistivity of the cable, leading to low eddy current coupling loss, but these reaction can harm the superconducting properties of filaments and should be prevented. More extensive study should be done to reduce the eddy current loss in the cables without harming the superconducting properties of the filaments and the stability of the cables.

To directly measure the eddy current loss of the samples at high frequencies, a pick up coil system was built. The loss of the MgB_2 cables was measured at 4.2 K with 50 Hz – 200 Hz under an applied magnetic field of 0.04 T. The AC loss of these MgB_2 cables was very low in these conditions, due to magnetic shielding and the high contact resistance between the strands. Such low AC losses make these cables potentially useful applications such as power transfer lines where the magnetic field is low but the frequencies are high.

APPENDIX A

COMPARISONS OF DISCRETE AND CONTINUOUS ANALYTIC MODELS FOR RECTANGULAR GEOMETRY COMPOSITES

The eddy current loss in rectangular superconducting composite in the network model, especially for the Rutherford cables, is expressed as below[1, 2]

$$\frac{Q_e}{V_s} = \frac{2}{3}\frac{w}{t} L_p B_m \left(\frac{dB}{dt}\right)\left(\frac{{N_s}^2}{20R_c}\right) \qquad (\mathrm{J/m^3}) \qquad (1)$$

Here, the eddy current loss from the side-by-side interstrand resistance is ignored. w is cable width, t is cable thickness, L_p is twist pitch, B_m is magnetic field amplitude, N_s is the number of strand in cable, and $R_\perp$ is the interstrand resistance.

On the other hand, the eddy current loss for such a superconducting composite described in terms of an anisotropic continuum model, typically used for HTSC, is expressed as

$$\frac{Q_e}{V_s} = \left(\frac{w}{t}\right)^2 f \frac{{B_m}^2}{2\rho_\perp} {L_p}^2 = \left(\frac{w}{t}\right)^2 \frac{B_m}{8\rho_\perp}\left(\frac{dB}{dt}\right){L_p}^2 \qquad (\mathrm{J/m^3}) \qquad (2)$$

Here, $\rho_\perp$ is effective resistivity. The shape factor, $(w/t)^2$ is added to the equation kernel following Carr[3]. We have to convert the interstrand resistance, R_c, to an effective resistivity, $\rho_\perp$ in order to compare (1) and (2).

$$\frac{R_c}{2n} = \frac{\rho_\perp 2d}{2wl} = \frac{\rho_\perp d}{wl}$$

Here, $2n = 2\frac{w}{h}$ is the number of contacts in Rutherford cable. *d* is a strand diameter.

Then, $$R_c = \frac{2d\rho_\perp}{lh}$$

Also, from figure, $\frac{N_s}{2} h = w$, and $\tan\theta = \frac{(h/2)}{l}$

therefore, $$\frac{N_s^{\ 2}}{R_c} = \frac{8w^2 l}{h\rho_\perp d}, \text{ since } \frac{l}{h} = \frac{1}{2\tan\theta} = \frac{L_p}{4w},$$

Then, $$\frac{N_s^{\ 2}}{R_c} = \frac{8w^2}{\rho_\perp d}\frac{L_p}{4w} = \frac{2wL_p}{\rho_\perp d} = \frac{4wL_p}{\rho_\perp t}$$

Finally, if we input this to (1), we get

$$\frac{Q_e}{V_s} = \frac{2}{3}\frac{w}{t}L_p B_m \left(\frac{dB}{dt}\right)\left(\frac{N_s^{\ 2}}{20 R_c}\right) = \frac{2}{15}\left(\frac{w}{t}\right)^2 \frac{L_p^{\ 2}}{\rho_\perp} B_m \left(\frac{dB}{dt}\right),$$

which is 6.67% different from (2).

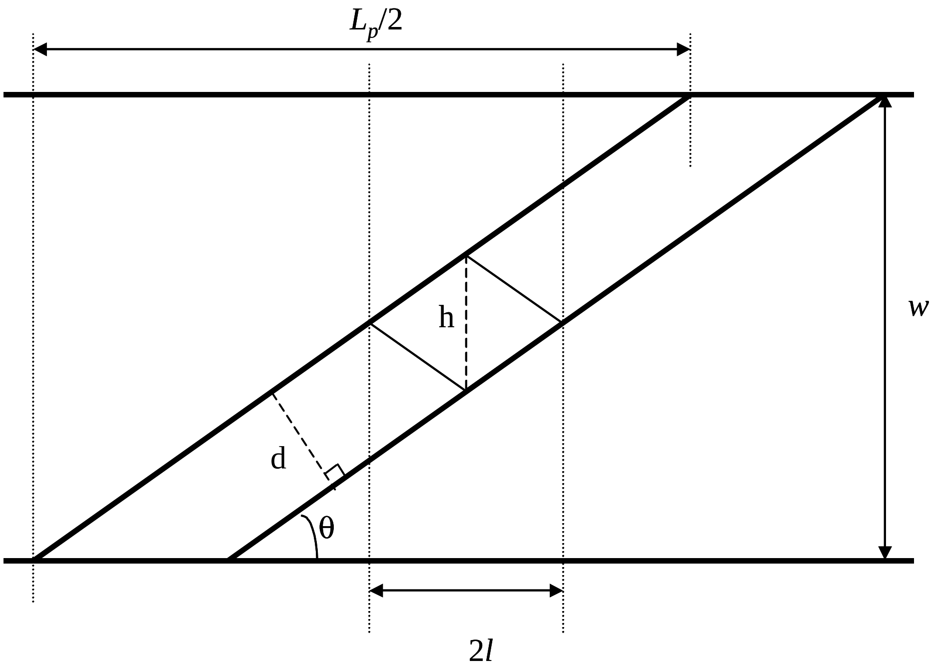

Fig. A.1. Crossover area in a Rutherford cable.

APPENDIX B

EDDY CURRENT COUPLING LOSS IN SEVEN-STRAND CABLES

The eddy current path of a seven strand cable is shown in Fig. B.1. Consider the contact resistance of this postulated eddy current path with cross section A_e and the path length t_{com}. The measured contact resistance by four-point probe method should be normalized by the number of current path as follows.

R_c: contact resistance at eddy current path = (measured R_c) $\times$ $(L_s/2r)$

The relationship between (measured R_n) (n = 1,2,3,4) and (measured R_c) is in Appendix D.

L_s: sample length $\approx L_{st}$ (strand length of the sample)

$(L_s/2r)$: Number of current path in the sample

A_e: cross section of eddy current path, πr^2

$t_{com} = 6r$ (from top filament to bottom filament, or vice versa)

r : radius of one strand

When magnetic field changes with certain frequency, the electromotive force is,

$V = \dot{\Phi} = \dot{B}A_D$. The diamond area in Fig. B.1. is $A_D = (3/2)L_p r$.

$I_e = \frac{V}{R_t} = \frac{\dot{B}A_D}{R_t} = \frac{\dot{B}A_D}{R_t}$, It is assumed no resistance along the superconducting filaments.

There are two contact resistances, R_c for effective transverse resistance, $R_\perp$, and two transverse resistance for total resistance along the eddy current path.

R_t: total resistance along the eddy current path is given by $R_t = 2R_\perp = 4R_c$

$$2R_c = R_\perp = \frac{\rho_{oxide} t_{oxide}}{A} = \frac{\frac{t_{com}}{t_{oxide}} \rho_\perp t_{oxide}}{A} = \frac{t_{com}\rho_\perp}{A} = \frac{6\rho_\perp}{\pi r}$$

Loss from one diamond loop $= I_e{}^2 R_t = \frac{\dot{B}^2 A_D{}^2}{4R_c} = \frac{9r^2\dot{B}^2 L_p{}^2}{16R_c} = \frac{9\pi r^3 \dot{B}^2 L_p{}^2}{48\rho_\perp}$

Loss per volume = $\frac{9\pi r^3 \dot{B}^2 L_p{}^2}{48\rho_\perp} \times \frac{(L_p/2r)}{\pi(3r)^2 L_p} = \frac{\dot{B}^2 L_p{}^2}{96\rho_\perp} = \frac{\dot{B}^2 L_p{}^2}{32\pi r R_c} = \frac{\dot{B}^2 L_p}{16\pi R_c} \cdot N_e$

$N_e = L_p/2r$, Number of *eddy current paths* in the volume, not the number of strands.

The loss from this derivation $\left(\frac{\dot{B}^2 L_p{}^2}{96\rho_\perp}\right)$ is less than the loss for twisted round stand by Carr[3] , which is $\frac{P_e}{V_s} = (\mu_0 \dot{H}_0)^2 \sigma_\perp \left(\frac{L_p}{2\pi}\right)^2 = \frac{\dot{B}^2 L_p{}^2}{4\pi^2 \rho_\perp}$. But, considering the current path in seven strand cables is greatly reduced comparing to that of the multifilamentary LTSC, the smaller loss is reasonable.

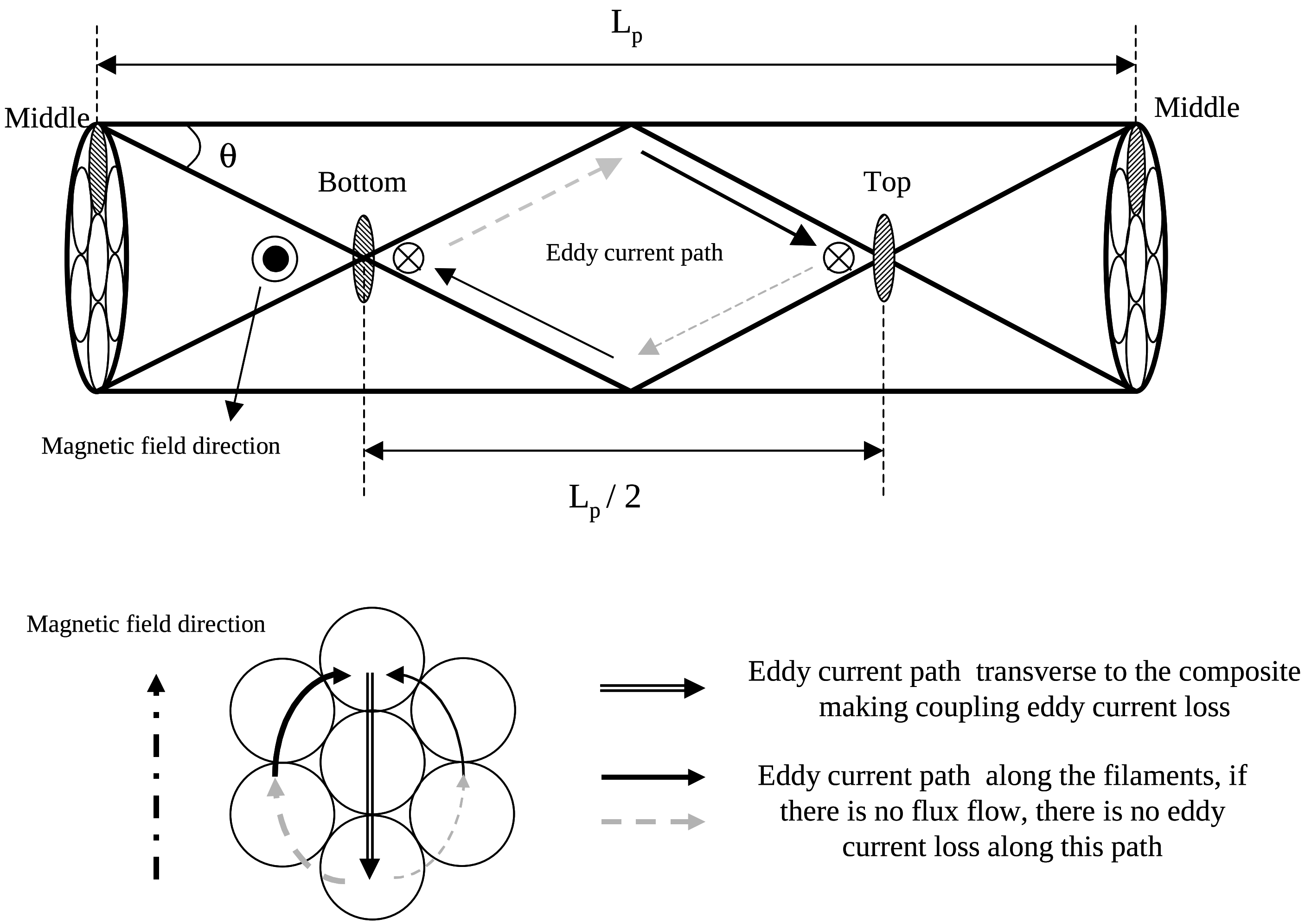

Fig. B.1. Eddy current path in a seven strand MgB_2 cable.

APPENDIX C

EFFECTIVE RESISTIVITY OF A SUPERCONDUCTING COMPOSITE

By using effective medium theory, we can derive (1-9-a) and (1-9-b). We assume filaments are cylindrical shape and do not consider potential variation according to composite axis. Then, we can make ‘unit cell’ which is composed of superconducting filament and matrix around it as Fig. C. 1

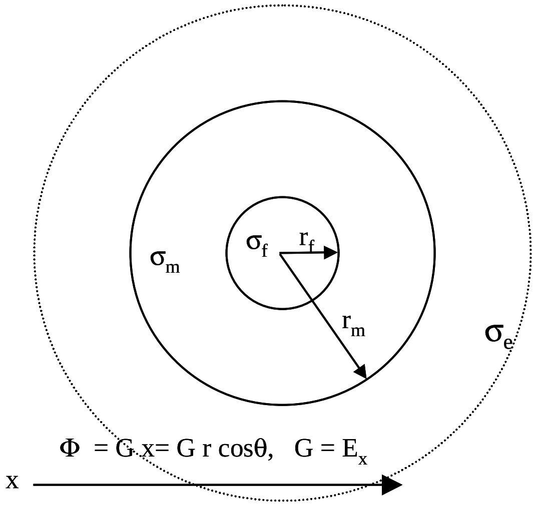

Fig. C.1. Unit cell of the filament with radius r_f, conductivity σ_f, and matrix with radius r_m, and conductivity σ_m. We want to know the effective conductivity of the composite, σ_e.

The volume fraction of the superconducting filament within the unit cell shown above is $\lambda = (r_f / r_m)^2$, The potential is given by $\Phi = Gx = Gr\cos\theta$ where G is gradient of Φ, i.e., the electric field E_x. If we assume there is no source of charge inside filaments, then we can use the Laplace equation, $\nabla^2 \Phi = 0$. The general solution of this differential equation in a cylindrical geometry is

$$\Phi(r,\theta) = (Ar + \frac{B}{r})\cos\theta$$

inside of the filament, $$\Phi_f = (A_f r + \frac{B_f}{r})\cos\theta, \tag{1}$$

within the matrix, $$\Phi_m = (A_m r + \frac{B_m}{r})\cos\theta, \tag{2}$$

and for an effective medium averaged in a length scale much larger than the filamentary scale, $$\Phi_e = (A_e r + \frac{B_e}{r})\cos\theta. \tag{3}$$

We now apply a boundary condition. We know that at $r_f = 0$, Φ must have finite value, therefore from (1) $B_f = 0$.

Then, $$\Phi_f = A_f r\cos\theta \tag{1-1}$$

$$\Phi_e = G\, r\cos\theta, \tag{3-1}$$

therefore from (3), $B_e = 0$ and $A_e = G$.

Also, at r_f $$\Phi_f(r_f, \theta) = \Phi_m(r_f, \theta), \tag{4}$$

And, at r_m $$\Phi_m(r_m, \theta) = \Phi_e(r_m, \theta), \tag{5}$$

at r_f $$-\sigma_f \frac{\partial \Phi_f}{\partial r} = -\sigma_m \frac{\partial \Phi_m}{\partial r} \ , \tag{6}$$

at r_m $$-\sigma_m \frac{\partial \Phi_m}{\partial r} = -\sigma_e \frac{\partial \Phi_e}{\partial r} \ . \tag{7}$$

We have 4 unknowns, A_f, A_m, B_m and σ_e and 4 equations (4),(5),(6),(7). After solving simultaneously using λ, we can get σ_e.

$$\sigma_e = \sigma_m \frac{\sigma_f + \sigma_m - \lambda(\sigma_m - \sigma_f)}{\sigma_f + \sigma_m + \lambda(\sigma_m - \sigma_f)}$$

if interface resistivity is low $\sigma_f \to \infty$, then $\sigma_e = \sigma_m \frac{1+\lambda}{1-\lambda}$ and

if interface resistivity is high $\sigma_f \to 0$, then $\sigma_e = \sigma_m \frac{1-\lambda}{1+\lambda}$.

APPENDIX D

CONTACT RESISTANCE OF A SEVEN-STRAND CABLE

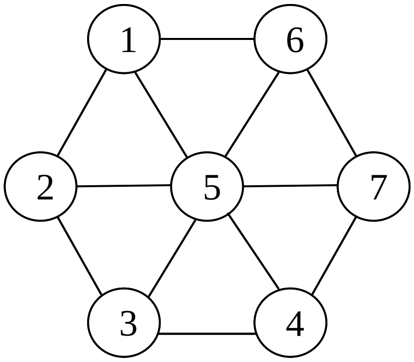

Fig. D.1. Contacts between individual strands in an MgB_2

Considering the symmetry of seven strand MgB_2 cable, there are four kinds of contact resistances R_1(1 and 2), R_2 (1 and 3), R_3 (1 and 4) and R_4(1 and 5). There are many possible connections, but the maximum connection between two strands is assumed 6, considering the number of strands. Also, the contact resistance is assumed same as R_c.

For contact resistance R_1, R_2, R_3 and R_4 the possible current paths are in Table D.1

Then, for R_1,

$$\frac{1}{R_1}=\frac{1}{R_c}+\frac{1}{2R_c}+\frac{2}{3R_c}+\frac{3}{4R_c}+\frac{4}{5R_c}+\frac{5}{6R_c}+.....=\frac{273}{60R_c} \text{ Therefore, } R_1=\frac{60}{273}R_c$$

For R_2,

$$\frac{1}{R_2}=\frac{2}{2R_c}+\frac{4}{3R_c}+\frac{5}{4R_c}+\frac{4}{5R_c}+\frac{2}{6R_c}+.....=\frac{283}{60R_c}\text{ Therefore, }R_2=\frac{60}{283}R_c$$

For R_3,

$$\frac{1}{R_3}=\frac{1}{2R_c}+\frac{4}{3R_c}+\frac{6}{4R_c}+\frac{4}{5R_c}+\frac{2}{6R_c}+.....=\frac{258}{60R_c}\text{ Therefore, }R_3=\frac{60}{258}R_c$$

For R_4,

$$\frac{1}{R_4}=\frac{1}{R_c}+\frac{2}{2R_c}+\frac{2}{3R_c}+\frac{2}{4R_c}+\frac{2}{5R_c}+\frac{2}{6R_c}+.....=\frac{234}{60R_c}\text{ Therefore, }R_4=\frac{60}{234}R_c$$

Possible paths for R_1	Resistance	Possible paths for R_2	Resistance	Possible paths for R_3	Resistance	Possible paths for R_4	Resistance
1 2	R_c	1 2 3	$2R_c$	1 5 4	$2R_c$	1 5	R_c
1 5 2	$2R_c$	1 5 3	$2R_c$	1 2 3 4	$3R_c$	1 2 5	$2R_c$
1 5 3 2	$3R_c$	1 6 5 3	$3R_c$	1 6 7 4	$3R_c$	1 6 5	$2R_c$
1 6 5 2	$3R_c$	1 2 5 3	$3R_c$	1 2 5 4	$3R_c$	1 6 7 5	$3R_c$
1 5 4 3 2	$4R_c$	1 5 2 3	$3R_c$	1 6 5 4	$3R_c$	1 2 3 5	$3R_c$
1 6 5 3 2	$4R_c$	1 5 4 3	$3R_c$	1 2 5 3 4	$4R_c$	1 6 7 4 5	$4R_c$
1 6 7 5 2	$4R_c$	1 6 7 5 3	$4R_c$	1 2 3 5 4	$4R_c$	1 2 3 4 5	$4R_c$
1 6 5 4 3 2	$5R_c$	1 5 7 4 3	$4R_c$	1 2 5 7 4	$4R_c$	1 6 7 4 3 5	$5R_c$
1 6 7 4 3 2	$5R_c$	1 6 5 4 3	$4R_c$	1 6 7 5 4	$4R_c$	1 2 3 4 7 5	$5R_c$
1 6 7 5 3 2	$5R_c$	1 6 5 2 3	$4R_c$	1 6 5 7 4	$4R_c$	1 6 7 4 3 2 5	$6R_c$
1 5 7 4 3 2	$5R_c$	1 6 7 4 3	$4R_c$	1 6 5 3 4	$4R_c$	1 2 3 4 7 6 5	$6R_c$
1 6 7 4 3 5 2	$6R_c$	1 5 6 7 4 3	$5R_c$	1 6 5 2 3 4	$5R_c$		
1 6 7 4 5 3 2	$6R_c$	1 6 5 7 4 3	$5R_c$	1 2 5 6 7 4	$5R_c$		
1 6 5 7 4 3 2	$6R_c$	1 2 5 7 4 3	$5R_c$	1 6 7 5 3 4	$5R_c$		
1 6 7 5 4 3 2	$6R_c$	1 6 7 5 2 3	$5R_c$	1 2 3 5 7 4	$5R_c$		
1 5 6 7 4 3 2	$6R_c$	1 6 7 4 5 2 3	$6R_c$	1 2 3 5 6 7 4	$6R_c$		
		1 2 5 6 7 4 3	$6R_c$	1 6 7 5 2 3 4	$6R_c$		

Table D.1. Possible current paths for R_1, R_2, R_3 and R_4.

REFERENCE FOR APPENDIX

[1] V. E. Sytnikov and I. B. Peshkov, "Coupling losses for superconducting cables in pulsed fields," *Advances in cryogenic engineering*, vol. 40, pp. 537-542, 1994.

[2] V. E. Sytnikov, G. G. Svalov, S. G. Akopov, and I. B. Peshkov, "Coupling losses in superconducting transposed conductors located in changing magnetic fields," *Cryogenics*, vol. 29, pp. 926-930, 1989.

[3] W. J. Carr, *AC Loss and Macroscopic Theory of Superconductors*, 2 ed. New york: Tayor and Francis, 2001.

BIBLIOGRAPHY

Akhmetov, A. A. (2000). "Compatibility of two basic models describing the AC loss and eddy currents in flat superconducting cables." Cryogenics **40**: 445-457.

Amemiya, N., K. Miyamoto, et al. (1997). "Numerical analysis of AC losses in high T_c superconductors based on *E-J* characteristics represented with *n*-value.".

Amemiya, N., K. Miyamoto, et al. (1998). "Finite element analysis of AC loss in non-twisted Bi2223 tape carrying AC transport current and /or exposed to DC or AC external magentic field." Physica C **310**: 30-35.

Amemiya, N., S. Murasawa, et al. (1998). "Numerical modelings of superconducting wires for AC loss calculations." Physica C **310**: 16-29.

Banno, N. (1999). "Theoretical model of twisted high T_c superconducting tapes for numerical alternating-current loss claculations." Journal of Applied Physics **85**: 4243-4249.

Banno, N. and N. Amemiya (1998). Numerical analysis of AC loss in high T_c twisted tape carrying AC transport current in external AC magnetic field - effect of twisting on loss reduction. Applied superconductivity Conference, Palm Desert, CA.

Boggs, S. A., E. W. Collings, et al. "AC losses in HTSC conductor elements." IEEE transactions on applied superconductivity.

Campbell, A. M. (1982). "A general treatment of AC losses in multifilamentary superconductors." Cryogenics: 3-16.

Carr, W. J. (1983). AC loss and macroscopic theory of superconductor. New York, Gordon and Breach.

Carr, W. J. (2001). AC loss and macroscopic theory of superconductors. New York, Tayor and Francis.

Carr, W. J. and V. Kovachev (1995). "Interstrand eddy current losses in rutherford cable." Cryogenics **35**: 529-534.

Cheng, C. H., Y. Zhao, et al. (2000). "Thermal diffusion and AC loss in high T_c superconductors." Physica C **337**: 239-244.

Ciszek, M., S. P. Ashworth, et al. (1996). "Transport AC losses in multifilamentary Ag/Bi-2223 tapes in low external DC magnetic fields." Physica C **272**: 319-325.

Ciszek, M., A. M. Campbell, et al. (1995). “Energy dissipation in high temperature ceramic superconductors.” Applied Superconductivity **3**: 509-520.

Collings, E. W. (1986). Applied superconductivity, metallurgy, and physics of titanium alloys. New York, Plenum Press.

Collings, E. W. (1988). “Stabilizer design considerations in fine-filament Cu/Nbti composites.” Advances in Cryogenic Engineering Materials **34**: 867-878.

Collings, E. W., K. R. Marken, et al. (1991). AC loss and dynamic resistance of a high T_c strand carrying a direct current in a tranverse AC magnetic field. CEC/ICMC, Huntsville, AL.

COMSOL (2002). FEMLAB 2.3 Eletromagnetic module manual, COMSOL AB.

Darmann, F., R. Zhao, et al. (1998). “AC losses of filamentary HTS twisted filaments round wires and flat tapes.”.

Dhalle, M., A. Polcari, et al. (1998). “Reduced filament coupling in Bi(2223)/$BaZrO_3$/Ag composite tapes.” Physica C **310**: 127-131.

Dolgosheev, P. I., G. G. Svalov, et al. (1995). “Transversal conductivity in conductors of "Cable in conduit" type.” IEEE transactions on applied superconductivity **5**: 749-752.

Eckelmann, H. (1998). “AC losses in multifilamentary Bi(2223) tapes with an interfilamentary resistive carbonate barrier.” Physica C **310**: 122-126.

Eckelmann, H., J. Krelaus, et al. (1999). AC losses of multifilamentary Bi(2223) tapes in external perpendicular magnetic fields with different internal resistive barrier structure betwwen the filaments. EUCAS'99, Sitges, Spain.

Eckelmann, H., M. Quilitz, et al. (1998). AC losses in multifilamentary low AC loss Bi(2223) tapes with novel interfilamentary resistive carbonate barriers. Applied Superconductivity Conference, Palm Springs, CA.

Farinon, S., P. Fabbricatore, et al. (2000). Shieding and Losses in Multifilamentary Tapes Exposed to Perpendicular AC Magnetic Fields. ASC 2000, Virginia Beach, VA.

Fukui, S., O. Tsukamoto, et al. (1998). “AC loss of low temperature superconducting AC wire caused by longitudinal and azimuthal AC magnetic field components.” Physica C **310**: 142-146.

Fukunaga, T. and A. Oota (1995). “Hysteresis and eddy-current losses of Ag sheathed $(Bi, Pb)_2\ Sr_2Ca_2Cu_3O_x$ rod-form wires under AC transport currents.” Physica C **251**: 325-329.

Funaki, K. (1990). Superconductivity, Part 8 AC loss measurements, International Electrotechnical Commission.

Funaki, K. (2000). “Basic approach to AC losses in HTS wires exposed to various types of eletromagnetic configuration.” Physica C **335**: 124-128.

Funaki, K., K. Kajikawa, et al. (1998). “A simple electromagnetic method of cyclic loss measurement for superconducting wires in a combined alternating transverse magnetic field and transport current.” Physica C **310**: 132-136.

Goldacker, W., M. Quilitz, et al. (1998). Novel resistive interfilamentary carbonate barriers in multifilamentary low AC loss tapes. Applied superconductivity Conference, Palm Desert, CA.

Hughes, T., F. Darmann, et al. (1999). “Reduction of the AC losses in Ag sheathed PbBi2223 tapes with twisted filaments.” Physica C **325**: 77-82.

Iwakuma, M., Y. Tajika, et al. (1998). “Twist effect on hysteresis loss in Bi2223 multifialmentary wires exposed to an AC magnetic field.” Physica C **310**: 154-158.

Jin, J. (1993). The finite element method in electromagnetics, John wiley & Sons.

Kajikawa, K. (1998). A new multi-purpose method for AC Loss measurements of superconducting wires. Electrical Engineering. Fukuoka, Kyushu University.

Kanbara, K. (1987). “Hysteresis loss of a round superconductor carrying a d.c transport current in an alternating transverse field.” Cryogenics **27**: 621-630.

Kovachev, V. (1991). Energy Dissipation in Superconducting Materials. New York, Oxford University Press.

Krelaus, J., R. Nast, et al. (1999). Novel, internally stranded "Ring Bundled Barrier" Bi-2223 tapes for low AC loss applications. EUCAS'99, Sitges, Spain.

Kwasnitza, K. and S. Clerc (1994). “AC Losses of Superconducting High-T_c Multifilament Bi-2223/Ag Sheated Tapes in Perpendicular Magnetic Fields.” Physica C **233**: 423-435.

Kwasnitza, K. and S. Clerc (1998). “Coupling current loss reduction in cable-in-conduit superconductors by thick chromium oxide coating.” Cryogenics **38**: 305--308.

Kwasnitza, K., S. Clerc, et al. (1999). “Reduction of alternating magnetic field losses in high T_c multifilament Bi(2223)/Ag tapes by high resistive barriers.” Cryogenics **39**: 829-841.

Lee, E., M. D. Sumption, et al. (2003). FEM modeling of AC loss in rutherford cables with and without resistive cores. CEC/ICMC, Anchorage, Alaska.

Lee, E., M. D. Sumption, et al. (2003). “Temperature and field dependence of the effective matrix resistivity of Bi:2223/Ag composites.” IEEE transactions on applied superconductivity **13**: 3614.

Lennikov, V., H. Caudevilla, et al. (1998). “Development of Ag sheathed Bi-2223 Multifilamentary tapes with MgO Coated Filaments.”.

Martinez, E., Y. Yang, et al. (2000). “Experimetal study of loss mechanisms of AgAu/PbBi-2223 tapes with twisted filaments under perpendicular AC magnetic fields at power frequencies.” Physica C **331**: 216-226.

Morgan, G. H. (1973). "Eddy currents in flat metal-filled superconducting braids." Journal of Applied Physics **44**: 3319-3322.

Mulder, G. B. J. and E. M. J. Niessen (1992). Coupling losses of multifilamentary superconductors having several concentric regions and mixed matrix, Chicago, IL.

Muller, K. H. (1997). AC loss in Y-123/hastelloy superconducting tapes. EUCAS'97.

Nijhuis, A., H. H. J. ten Kate, et al. (2001). "Control of contact resistance by strand surface coating in 36-strand NbTi CICCs." Cryogenics **41**: 1-7.

Okamoto, H. (2000). Desk handbook: Phase diagrams for binary alloys, ASM international.

Okamoto, H. (2002). Phase diagrams of dilute binary alloys, ASM international

Oomen, M., J. Rieger, et al. (1998). "Decease of magnetic AC loss in twisted-filament Bi-2223 tapes." Physica C **310**: 137-141.

Oomen, M., J. Rieger, et al. (1999). "Dynamic resistance in a slab-like superconductor with $J_c(B)$ dependence." Supercond. Sci. Technol. **12**: 382-387.

Reed, R. P. and A. F. Clark (1983). Materials at low temperature, American Society for Metals.

Rose-innes, A. C. (1978). Introduction to superconductivity. Oxford, New York, Pergamon Press.

Seeber, B. (1998). Handbook of applied superconductivity, IOP Publishing.

Seo, K., K. Fukuhara, et al. (2001). "Analysis for inter-strand coupling loss in multi-strand superconducting cable with distributed contact resistance between strands." Cryogenics **41**: 131-137.

Sheahen, T. P. (1994). Introduction to high temperature superconductivity. New York, Plenum Press.

Silvester, P. P. and R. L. Ferrari (1996). Finite elements for electrical engineers, Cambridge university press.

Sokolovsky, V., V. Meerovich, et al. (1998). "Analytical approach to AC loss calculation in high T_c superconductors." Physica C **306**.

Soltanian, S., J. Horvat, et al. (2003). "Effect of nano-carbon particle doping on the flux pinning properties of MgB_2 superconductor." Physica C **390**: 185-190.

Soltanian, S., M. J. Qin, et al. (2003). "Effect of sample size on the magnetic critical current density in nano-SiC doped MgB_2 superconductors." Physical Review B **68**: 134509.

Soltanian, S., X. L. Wang, et al. (2001). "High transport critical current density above 30 K in pure Fe-clad MgB_2 tape." Physica C **361**: 84-90.

Sumption, M. D. and E. W. Collings (1993). Transverse resistivities of Cu-matrix and Cu-Mn matrix multifilamentary strands as fuctions of magnetic field and temperature. CEC-ICMC93, Albuquerque, NM.

Sumption, M. D., E. W. Collings, et al. (2002). “Reduction and elimination of external-field AC loss in MgB_2/Fe wire by in situ magnetic shielding.” Physica C **378-381**: 894-898.

Sumption, M. D., E. W. Collings, et al. (2002). “Real and apparent loss suppression in MgB_2 superconducting composites.” Physica C **382**: 98-103.

Sumption, M. D., E. W. Collings, et al. (2000). “Coupling current control in stabrite-coated NbTi Rutherford cables by varying the width of a stainless steel core.” Advances in cryogenic engineering **46B**: 1043-1049.

Sumption, M. D., E. W. Collings, et al. (2001). “AC loss and interstrand contact resistance in bare and coated NbTi/Cu Rutherford cables with cores.” Supercond. Sci. Technol. **14**: 888-897.

Sumption, M. D., E. W. Collings, et al. (1999). “Core-suppressed AC loss and strand-moderated contact resistance in a Nb_3Sn Rutherford cable.” Cryogenics **39**: 1-12.

Sumption, M. D., E. W. Collings, et al. (1999). “Influence of strand surface condition on interstrand contact resistance and coupling loss in Nb-Ti wound Rutherford cables.” Cryogenics **39**: 197-208.

Sumption, M. D., E. Lee, et al. (2000). “Influence of filamentary and strand aspect ratios on AC loss in short, untwisted samples of HTSC and LTSC superconducting multifilamentary composites.” Physica C **337**: 187-194.

Sumption, M. D., E. Lee, et al. (2001). “Suppression of AC(hysteretic) loss by magnetic shielding of MgB_2/Fe superconductors: The Pseudo-Meissner effect.” Advances in cryogenic engineering **48**: 824.

Sumption, M. D., E. Lee, et al. (2000). “Extraction of matrix resistivity from short samples of superconducting multifilamentary composite tapes: Influence of strand twist and internal structure.” Physica C **335**: 164-169.

Sumption, M. D., H. H. J. ten Kate, et al. (1995). “Contact resistance and cable loss measurements of coated strands and cable wound from them.” IEEE transactions on applied superconductivity **5**: 692-696.

Sytnikov, V. E. and I. B. Peshkov (1994). “Coupling losses for superconducting cables in pulsed fields.” Advances in cryogenic engineering **40**: 537-542.

Sytnikov, V. E., G. G. Svalov, et al. (1989). “Coupling losses in superconducting transposed conductors located in changing magnetic fields.” Cryogenics **29**: 926-930.

Verweij, A. P. (1995). Electrodynamics of superconducting cables in accelerator magnets. Enschede, Twente University.

Wakuda, T., T. Nakano, et al. (1997). "*E-J* chracteristics and AC losses in a superconducting Bi(2223) hollow cylinder." Cryogenics **37**: 381-388.

Wang, X. L., S. H. Zhou, et al. (2003). "Significant enhancement of flux pinning in MgB_2 superconductor through nano-Si addition." Physica C **385**: 461-465.

Wilson, M. N. (1983). Superconducting magnets. New york, Oxford University Press.

Yamafuji, K., T. Wakuda, et al. (1997). "Generalized critical state model in high-T_c superconductors." Cryogenics **37**: 421-430.

Yang, Y., T. Hughes, et al. (1998). "Experimental study on AC losses in Ag sheathed PbBi2223 tapes with twist filaments." Physica C **310**: 147-153.

Zhang, P. X., R. Inada, et al. (2000). Fabrication and transport AC losses of (Bi,Pb) 2223 multifilamentary tapes with resistive barriers. Applied Superconductivity Conference, Virginia Beach, VA.